Induced superconductivity in HgTe based topological insulator nanowires

DISSERTATION ZUR ERLANGUNG DES DOKTORGRADES DER NATURWISSENSCHAFTEN (DR. RER. NAT.)
DER FAKULTÄT PHYSIK

DER UNIVERSITÄT REGENSBURG

vorgelegt von

Ralf Fischer

aus Kösching

im Jahr 2022

Promotionsgesuch eingereicht am: 20.07.2022
Die Arbeit wurde angeleitet von: Prof. Dr. Dieter Weiss

Prüfungsausschuss:

Vorsitzender:	Prof. Dr. Klaus Richter
1. Gutachter:	Prof. Dr. Dieter Weiss
2. Gutachter:	Prof. Dr. Milena Grifoni
weiterer Prüfer:	Prof. Dr. Sergey Ganichev

Termin des Promotionskolloquiums: 16.11.2022

Table of Contents

1 Introduction

The discipline of quantum computing emerged in the 1980s with the vision that a quantum computer has the ability of solving certain problems far faster than any conceivable classical computer [1, 2]. Algorithms have been proposed that allow searching in huge databases [3] or factorizing large numbers as used in encryption techniques [4].

In 2019, Google set a milestone by proving 'quantum supremacy'. They performed a calculation that is practically impossible for a classical computer with a quantum computer based on a processor with programmable superconducting qubits [5]. Despite this great efforts, there is a problem with the use of qubits: The quantum states are extremely fragile. Thus, any slight influence from the environment can cause a qubit to change its state. This requires complex procedures for error correction [6–8].
However, Alexei Kitaev provided a different approach [9]. He proposed to make qubits out of anyons which possess non-Abelian exchange statistics and have a topological protection against errors. These so-called 'topological qubits' are the most promising platform for fault-tolerant quantum computing [10].

In 1937, Ettore Majorana proposed the Majorana fermion, which is a particle and its own antiparticle at the same time [11]. This particle obeys these non-Abelian exchange statistics. In condensed matter physics, Majorana Fermions do not exist as free particles, but as quasiparticle excitations, so-called Majorana bound states. To be more precise, they occur as zero-energy excitations in spinless p-wave superconductors [12]. Since p-wave superconductors are practically unusable until now [13], a different approach was proposed by Fu and Kane [14]. They suggest to engineer a spinless p-wave superconductor, which is also called a topological superconductor, by inducing s-wave superconductivity to the surface states of a three-dimensional (3D) topological insulator. Since then, various concepts to search for Majorana bound states have been suggested [15].

The prevailing platform are semiconductor nanowires with strong spin-orbit interaction in which s-wave superconductors induce topological superconductivity [16–20]. The experiments have already provided good signatures for the existence of Majorana bound states at the proximitized region of a semiconductor wire, but it could not be proven beyond doubt [21, 22].

In this work, we explore a yet untried concept to realize topological superconductivity by combining s-wave superconductors and topological insulator nanowires [23, 24]. Without a magnetic field, the subband structure of the nanowire is topologically trivial. This changes by applying a magnetic flux of one-half flux quantum $\Phi_0/2 = h/2e$ through the cross-sectional area of the wire. Now, the system becomes topologically nontrivial [25, 26], and Majorana bound states are expected to emerge when superconductivity is induced into the wire. In contrast to trivial Andreev bound states whose energy-phase relation is 2π-periodic, the Majorana bound state has 4π-periodicity [27, 28]. Thus, the related Josephson supercurrent is also 4π-periodic.

We fabricate nanowires based on the 3D topological insulator Mercury Telluride (HgTe). The topological nature of the surface states emerging were revealed in various experiments dealing with Hallbar devices [29–31] as well as nanowires [32]. Superconducting contacts made of Niobium (Nb) are placed on top of the nanowires to induce superconductivity.

We analyze the behavior of fabricated Josephson junctions in an applied magnetic field where various directions of the field with respect to the wire are investigated. The main part of this work deals with the search for a 4π-periodic supercurrent in our devices. To probe this signature of the Majorana bound state, we examine the fractional Josephson effect by measuring the I-V characteristic of the devices under microwave irradiation [17, 33–37]. With a microwave field, quantized voltage (Shapiro) steps appear at voltages $V_n = nhf/2e$ with f the microwave frequency and n an integer [38]. In the case of 4π-periodic Josephson currents, the odd steps $n = 1, 3, ...$ are partially missing [39]. The appearance of a 4π-periodic supercurrent is a strong signature of topological superconductivity, but not proof beyond doubt as missing Shapiro steps have also been found in topologically trivial devices [40]. A special focus is on the transition from the trivial to the topological state when an axial magnetic field is applied along the wire. This is achieved by tracing the 4π-periodic fraction of the supercurrent as a function of the magnetic flux penetrating the cross-sectional area of the nanowire and by disentangling trivial and topological 4π-periodic currents with the aid of a perpendicular magnetic field.

The outline of this thesis is as follows:

- Chapter 2 reviews the theoretical concepts. An introduction of topology in condensed matter physics is given leading to the concept of 3D topological insulators. The material HgTe is presented, and the theory of nanowires made from a 3D topological insulator is shown.

  The second part of this chapter introduces the microscopic theory of conventional superconductivity and gives an overview of the physics in normal conductor/superconductor hybrid structures. Here, the concept of Josephson junctions and Andreev bound states is explained. Additionally, the behavior of

Josephson junctions under microwave radiation using a resistivity and capacitively shunted junction (RCSJ) model and in the presence of an out-of-plane magnetic field is studied.

The chapter ends with an introduction of unconventional superconductivity and Majorana fermions. The emergence of Majorana fermions at the ends of an one-dimensional (1D) p-wave superconductor is highlighted. Furthermore, the current-phase relations of an 1D superconductor is derived focusing on the differences between s- and p-wave pairing. Finally, the realization of an 1D p-wave superconductor by the combination of a topological insulator nanowire and an s-wave superconductor is illustrated.

- Chapter 3 describes the experimental methods. The wafer material and the fabrication processes are illustrated, followed by a presentation of the cryogenic and electronic setup with a focus on the sample holder and filtering stages.
- Chapter 4 summarizes the basic properties of the materials and devices used. Here, the transport properties of HgTe are determined, and the critical parameters of the Nb films are extracted. Additionally, different parameters of the fabricated junctions are estimated. Particularly noteworthy in this context is the determination of the transmission at the superconductor/nanowire interfaces.
- Chapter 5 describes the study of HgTe wire based Josephson junction in a magnetic field. In the first part, the evolution of the critical current is investigated as a function of an out-of-plane magnetic field where the oscillations of the critical current resemble the Fraunhofer diffraction pattern. Additionally, special scenarios are described where no pattern can be observed in an out-of-plane magnetic field. For a magnetic field aligned parallel to the HgTe wire based Josephson junction, a Fraunhofer pattern would never be expected. Surprisingly, we find oscillations of the critical current which are $h/4e$- and even $h/8e$-periodic. These findings are discussed both experimentally and theoretically in the second part of the chapter. Lastly, we report on resistance oscillations as a function of the axial magnetic field that occur in the transition from the superconducting to the normal state.
- In chapter 6, we explore the expected topological transition in topological insulator nanowire based Josephson junctions as a function of magnetic flux by probing the 4π-periodic fraction of the supercurrent. We estimate the amplitude of the 4π-periodic current using a heuristic approach based on the resistively shunted junction (RSJ) model. Since this model neglects several effects, we show numerical simulations based on an extended RCSJ model aiming to reproduce the experimental results as accurately as possible. Furthermore, a method to distinguish between a trivial and a topological origin of the 4π-periodic supercurrent is presented.

Finally, a summary of the results obtained is given. The thesis ends with a short outlook on possible future experiments that will bring the system one step closer to a potential application in the field of fault-tolerant quantum computing.

2 Theoretical background

This chapter contains the basic theoretical background which is important to understand the experimental results. At first, the concept of topological insulators is introduced. A basic description of conventional superconductivity follows. The focus here is on Josephson junctions and their behavior under microwave radiation and in a magnetic field. The chapter ends with the introduction of topological superconductivity. We show the emergence of Majorana fermions at the boundaries of an 1D p-wave superconductor and explain how this is achieved with the aid of topological insulator nanowires.

2.1 Topological insulators

Topological insulators are materials where an energy gap separates the valence band from the conduction band like in an ordinary insulator, but surface or edge states exist which are protected by time-reversal symmetry [41]. In this section, we review the concept of topology in condensed matter physics with a special treatment of the 3D topological insulator HgTe. Additionally, the special properties of nanowires made from 3D topological insulators are highlighted.

2.1.1 Topology in condensed matter physics

In the mathematical field of topology, objects are described by their genus g which counts the number of holes. Exemplary objects are sketched in figure 2.1(a-c). For instance, a doughnut can be transformed into a coffee mug under continuous deformations without closing the hole. Thus, they topologically belong to the same class ($g = 1$). However, a sphere has a different genus $g = 0$ since it cannot be deformed into a doughnut without closing the hole [41].

The same concept can be applied to classify Hamiltonians in condensed matter physics. The Hamiltonians of two systems are topologically equivalent if they can be continuously deformed into one another without closing the energy gap. The different classes can be distinguished by the so-called Chern number $n \in \mathbb{Z}$ where $\mathbb{Z}$ denotes integers [42]. Accordingly, the energy gap has to close at an interface where the

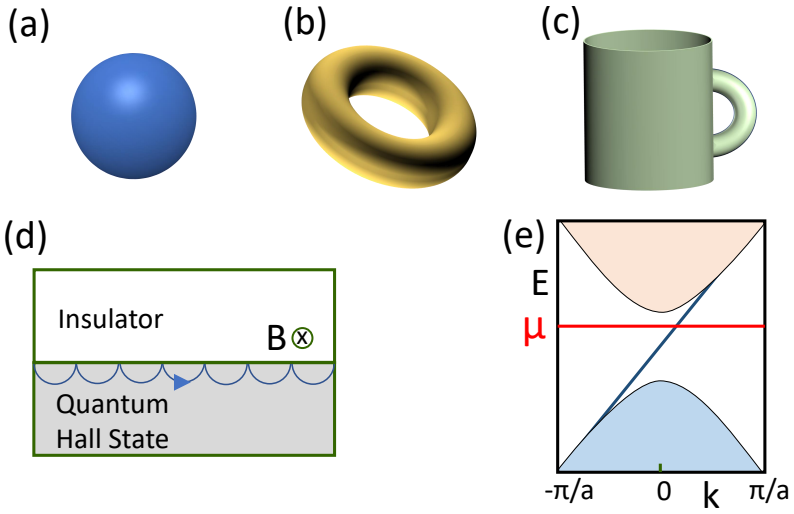

FIG. 2.1: (a-c) Different geometric objects as an illustration of topology. A doughnut (b) can be transformed into a coffe mug (c) without closing the hole. They are topologically equivalent. However, both objects cannot be transformed into a sphere (a) without closing the hole. (d) The interface between an insulator and the quantum Hall state. Since the Chern invariant changes, a conducting edge state emerges at the interface. (e) Electronic dispersion in the quantum Hall state. Here, an edge state connects the valence band and the conduction band. Adapted from [41].

Chern number changes. Therefore, the existence of conducting edge or surface states at such interfaces is a fundamental consequence of the topological classification [41]. Historically, the quantum Hall state was first of all discovered as a topological state [43]. Here, electrons in a two-dimensional electron gas (2DEG) are forced on circular orbits when a strong magnetic field is applied perpendicular to the plane of the 2DEG. These circular orbits are quantized with the cyclotron frequency ω_C and lead to the formation of Landau levels with energies $E_N = \hbar\omega_C\,(N + 1/2)$ where $\hbar$ is the reduced Planck constant. If N Landau levels are occupied, an energy gap separates the filled and the empty states similar to an ordinary insulator. However, the application of an electric field leads to the formation of conducting edge channels at the interface of a quantum Hall insulator and an ordinary insulator. These edge channels cause a quantized Hall conductance $\sigma_{xy} = Ne^2/h$ [44] where e is the elementary charge and h is the Planck constant. In a topological description, N is equal to the Chern invariant n [42]. At the interface between a quantum Hall insulator and an ordinary insulator, which is described by $n = 0$, the Chern invariant has to change from $n \neq 0$ to $n = 0$ leading to the formation of edge channels. Exemplarily, the situation is depicted in figure 2.1(d) for $n = 1$. A single edge channel is formed at the interface between the quantum Hall state and the insulating state. The corresponding electronic dispersion is shown in figure 2.1(e) where the band gap is closed by a conducting edge state.

As an applied magnetic field breaks time-reversal symmetry $\mathcal{T}$, the quantum Hall

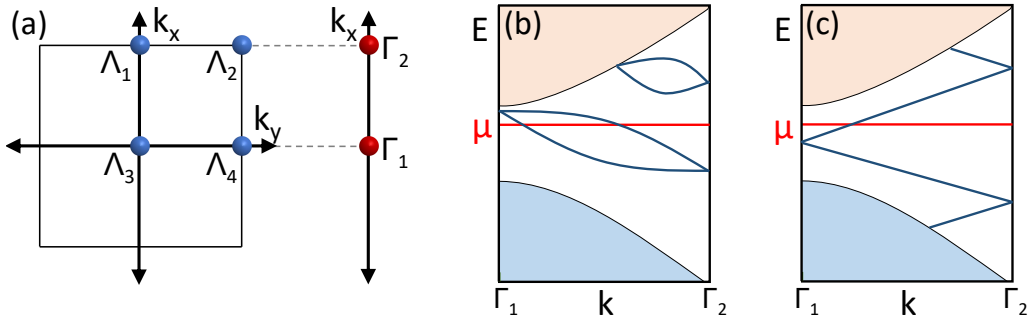

FIG. 2.2: (a) The Brillouin zone of a 2D system with four $\mathcal{T}$ invariant momenta Λ_i (blue dots). The $\mathcal{T}$ invariant momenta Γ_1 and Γ_2 of an edge are projections of pairs Λ_i. Adapted from [46, 47]. (b-c) Electronic dispersion of a $\mathcal{T}$ invariant 2D insulator. In (a), the number of edge states crossing the Fermi level μ is even. In (b), the number is odd. An odd number leads to topologically protected edge states. Adapted from [41].

state only occurs in systems where $\mathcal{T}$ is broken. $\mathcal{T}$ is given by an antiunitary operator $\Theta = i\sigma_y\mathcal{K}$ where σ_y is a Pauli spin matrix[1], and $\mathcal{K}$ is the complex conjugation operator [14]. For spin 1/2 particles, it yields $\Theta^2 = -1$, and a $\mathcal{T}$ invariant Hamiltonian has to fulfill

$$\Theta H\left(\vec{k}\right)\Theta^{-1} = H\left(-\vec{k}\right). \tag{2.1.1}$$

However, edge states can also appear in a system without the application of an external magnetic field due to strong spin-orbit interaction. Here, $\mathcal{T}$ is preserved, and the edge states can even be protected by $\mathcal{T}$ [45]. Because the Chern invariant is $n = 0$ in $\mathcal{T}$ invariant systems, a new $\mathbb{Z}_2$ topological number ν is introduced to characterize $\mathcal{T}$ invariant systems. The $\mathbb{Z}_2$ index can take two possible values $\nu = 0, 1$ which are explained in figure 2.2. The Brillouin zone of a two-dimensional (2D) system has four $\mathcal{T}$ invariant momenta Λ_i which are shown by the blue dots in figure 2.2(a). For an edge perpendicular to a vector $\vec{G}$, the $\mathcal{T}$ invariant momenta Γ_1 and Γ_2 are projections of pairs Λ_i onto the line perpendicular to $\vec{G}$. The electronic dispersion of a $\mathcal{T}$ invariant 2D insulator is plotted as a function of the crystal momentum k on a path connecting Γ_1 and Γ_2 in figure 2.2(b-c). Only half of the Brillouin zone $0 < k < \pi/a$, where a is the lattice constant, is shown since the other half is just a mirror image due to $\mathcal{T}$. The Kramers' theorem constrains that all eigenstates of a $\mathcal{T}$ invariant Hamiltonian are at least twofold degenerate [41]. Therefore, if edge states exist inside the band gap, they must at least be twofold degenerate at the $\mathcal{T}$ invariant momenta $k = \Gamma_1 = 0$ and $k = \Gamma_2 = \pi/a$. Between these points, the degeneracy is lifted due to spin-orbit interaction. There are two possibilities how the states at $k = \Gamma_1$ and $k = \Gamma_2$ can connect. In figure 2.2(b), they connect pairwise, i.e. the Fermi energy μ intersects the bands an even number of times. In this case, the edge states can be pushed away, e.g. by strong disorder, and we obtain an

[1]Let us recall the Pauli matrices: $\sigma_0 = \begin{pmatrix} 1 & 0 \\ 0 & 1 \end{pmatrix}$, $\sigma_x = \begin{pmatrix} 0 & 1 \\ 1 & 0 \end{pmatrix}$, $\sigma_y = \begin{pmatrix} 0 & -i \\ i & 0 \end{pmatrix}$, $\sigma_z = \begin{pmatrix} 1 & 0 \\ 0 & -1 \end{pmatrix}$.

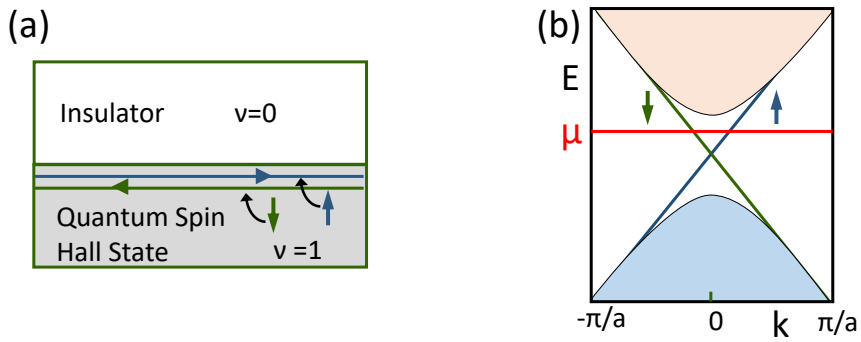

FIG. 2.3: (a) Interface between a trivial insulator and a QSHI. Since the $\mathbb{Z}_2$ invariant changes at the interface, helical edge states emerge. (b) Electronic dispersion of a QSHI. Helical edge states exist in the band gap connecting the valence band and the conduction band. Adapted from [41].

ordinary insulator with the $\mathbb{Z}_2$ invariant $\nu = 0$. In contrast, the edge states cannot be eliminated when μ intersects the bands an odd number of times as it is sketched in figure 2.2(c). The $\mathbb{Z}_2$ invariant is $\nu = 1$, and the edge states are topologically protected [41, 46, 47].

Such 1D topological edge states exist in a quantum spin Hall insulator (QSHI) which is also known as a 2D topological insulator. This state was firstly proposed in graphene [45]. Later, the existence was also theoretically predicted in HgTe/CdTe quantum wells [48] and experimentally verified by König et al. [49]. Since $\mathcal{T}$ is still preserved, the edge states form Kramers pairs and are helical, i.e. the direction of movement is coupled to the orientation of the spin. The situation is illustrated in figure 2.3(a). At the interface of a QSHI and an ordinary insulator, two edge channels exist. The spin-up electrons move to the left, while the spin-down electrons move to the right. The directions are vice versa on the opposite interface. The channels are forbidden to scatter into each other as long as $\mathcal{T}$ is present [41]. The band structure of a QSHI is shown in figure 2.3(b). Here, two helical edge states connect the conduction band and the valence band.

2.1.2 3D topological insulators

The principle of the QSHI can be extended to three dimensions [47]. Instead of edge channels at the boundaries of a 2D topological insulator, 2D surface states emerge for 3D topological insulators. Here, four $\mathbb{Z}_2$ invariants (ν_0; $\nu_1\nu_2\nu_3$) are needed to characterize a 3D topological insulator. Their meaning can be explained in a similar way as for the QSHI. In figure 2.4(a), the Brillouin zone of a 3D insulator is shown. Now, there are eight $\mathcal{T}$ invariant points Λ_i in the Brillouin zone of a 3D crystal. The surface Brillouin zone for a surface perpendicular to $\vec{G}$ has four $\mathcal{T}$ invariant momenta

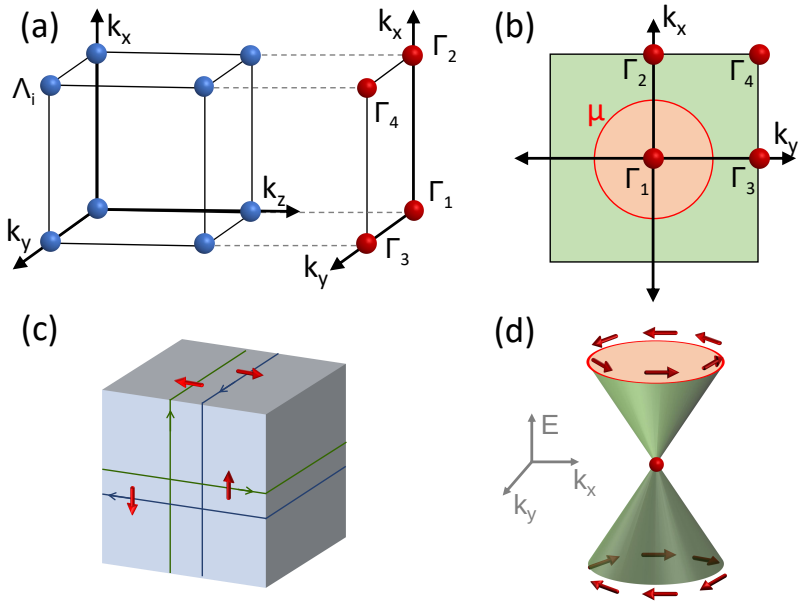

FIG. 2.4: (a) The Brillouin zone of a 3D insulator with eight $\mathcal{T}$ invariant points Λ_i (blue dots) in the Brillouin zone. A surface Brillouin zone has four $\mathcal{T}$ invariant momenta Γ_i (red dots) which are projections of pairs Λ_i. Adapted from [46, 47]. (b) Surface Brillouin zone of a 3D topological insulator. The Fermi circle encloses a single $\mathcal{T}$ invariant point. This describes a strong topological insulator. Adapted from [41]. (c) The surface states of a 3D topological insulator in real space. The spin of the electrons is always orientated perpendicular to the direction of motion. (d) A Dirac cone describes the dispersion of a single surface. Adapted from [50].

$\Gamma_1, \Gamma_2, \Gamma_3$ and Γ_4. These are projections of pairs Λ_i into the plane perpendicular to $\vec{G}$. Due to Kramers' degeneracy, the $\mathcal{T}$ invariant points at Γ_i, which are also called Dirac points, are twofold degenerate, while the degeneracy is lifted between them due to spin-orbit interaction. Again, the surface band structure resembles either figure 2.2(b) or 2.2(c) for a path connecting any pair Γ_i and Γ_j. The total number of intersections between the Fermi circle and the surface states determines the topological properties of the system. If the number of intersections is even, the system is called a weak topological insulator, and the first $\mathbb{Z}_2$ invariant is $\nu_0 = 0$. The surface states are not protected by $\mathcal{T}$ and can be localized in the presence of disorder. On the other hand, when the Fermi surface intersects the paths connecting any pair Γ_i and Γ_j an odd number of times, ν_0 is 1, and we call it a strong topological insulator. In this case, the surface states are topologically protected and cannot be localized. The other invariants $(\nu_1\nu_2\nu_3)$ can be interpreted as Miller indices which describe the orientation of the layer. The simplest case of a strong topological insulator is achieved when only a single Dirac point, e.g. Γ_1, is enclosed by the Fermi circle while this point is connected to every other $\mathcal{T}$ invariant point as in figure 2.2(c), i.e. μ crosses the

bands an odd number of times. The Brillouin zone, where a single Dirac point is enclosed by the Fermi circle, is visualized in figure 2.4(b). Here, a single surface of a 3D topological insulator is described by the Hamiltonian

$$H_{Surf} = \hbar v_F \left(\hat{k}_x \sigma_x + \hat{k}_y \sigma_y \right) \tag{2.1.2}$$

with the Pauli matrices σ_x, σ_y, the wave number operators $\hat{k}_x = -i\partial_x$, $\hat{k}_y = -i\partial_y$, and the Fermi velocity v_F. By inserting a plane wave ansatz $\Psi = \mathrm{e}^{-ik_x x}\mathrm{e}^{-ik_y y}\chi$, where χ is a two-component spinor, into the Dirac equation $H_{Surf}\Psi = E\Psi$, we obtain a Dirac-like dispersion

$$E = \pm\hbar v_F \sqrt{k_x^2 + k_y^2}. \tag{2.1.3}$$

The resulting 2D Dirac cone describing a single surface of a 3D topological insulator is plotted in figure 2.4(d). The special property of these surface states is that they are not spin degenerate. This results from the fact that states at momenta $\vec{k}$ and $-\vec{k}$ must have an opposite spin due to $\mathcal{T}$. Thus, the spin rotates with $\vec{k}$ around the Fermi circle as shown in figure 2.4(d). Each state has only one spin orientation and the spin is always orientated perpendicular to the direction of motion. This phenomenon is known as spin-momentum locking [41, 46, 47]. A corresponding real-space picture is shown in figure 2.4(c).

The spin-momentum locking has nontrivial consequences for the Berry phase γ_n^B acquired by an electron moving around the Fermi circle. In general, the Berry phase γ_n^B is the accumulated phase factor of a quantum mechanical system after it completes a closed path C in the parameter space, i.e. the position $\vec{R}\,(t = T)$ is equal to $\vec{R}\,(t = 0)$. The Berry phase is defined as

$$\gamma_n^B = \oint_C d\vec{R} \cdot \vec{\mathcal{A}}_n \left(\vec{R} \right) \tag{2.1.4}$$

with the Berry connection $\vec{\mathcal{A}} = i\langle n, \vec{R}|\nabla_R|n, \vec{R}\rangle$ where n is the n-th eigenstate of the system [50, 51]. In our case, an electron circles a single Dirac point where its spin rotates by 2π. This results in a Berry phase of π [52]. As we will show in section 2.1.4, the π Berry phase plays an important role dealing with topological insulator nanowires.

2.1.3 Strained HgTe as a 3D topological insulator

So far, we only discussed if surface states are topologically protected or not. To understand how such states actually arise in HgTe, we take a closer look at the band structure of the system. HgTe has a zincblende lattice and forms the bonds between the 6s electrons of the Hg atoms and the 5p electrons of the Te atoms. To demonstrate the special properties of the HgTe bandstructure, we additionally

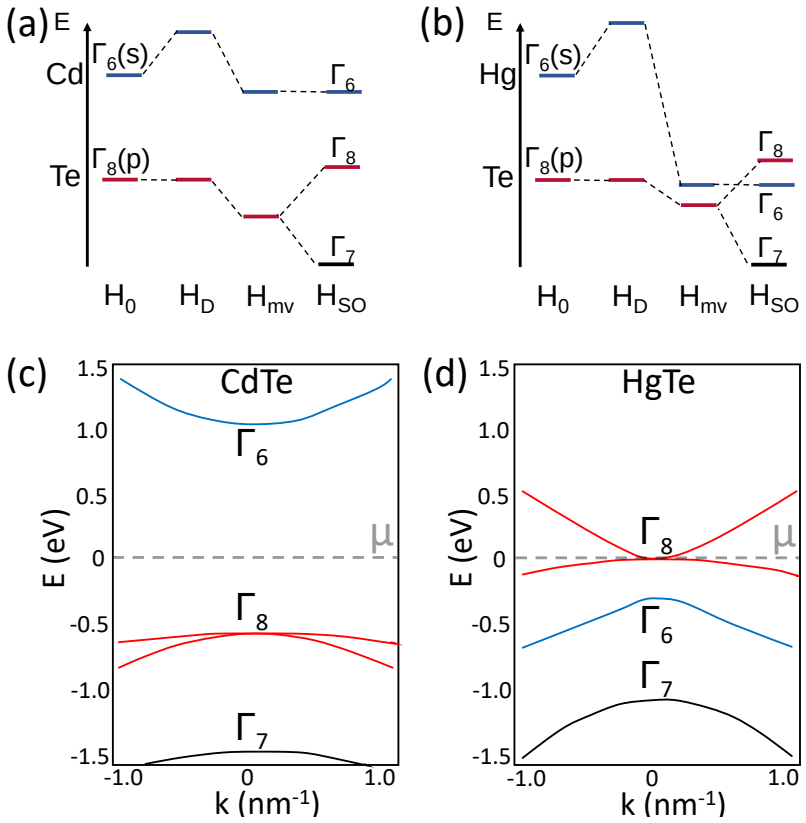

FIG. 2.5: (a-b) Illustration of energy corrections from the Darwin term (H_D), mass-velocity term (H_{mv}) and spin-orbit term (H_{SO}) to the Γ_6 band and the Γ_8 band of CdTe (a) and HgTe (b). Adapted from [53]. (c) Band structure of CdTe. CdTe has a conventional band structure where the Γ_6 band lies above the Γ_8 band. (d) Band structure of HgTe. HgTe has an inverted band structure since the Γ_8 band lies above the Γ_6 band. Adapted from [48].

take a look at the bandstructure of cadmium telluride (CdTe) for comparison. In figure 2.5(a), the energy levels at the Γ-point are shown for CdTe, while they are sketched for HgTe in figure 2.5(b). In the initial system (H_0), the energy levels look quite similar. The s-type Γ_6 band lies energetically above the p-type Γ_8 band. However, relativistic corrections to the energy levels have to be taken into account. While the Darwin term (H_D) and the mass velocity term (H_{mv}) result in a small correction of the energy levels in CdTe, the effect is much stronger in HgTe. Here, the Γ_6 band is almost reduced to the same level as the Γ_8 band. The spin-orbit interaction (H_{SO}) splits the Γ_8 band in a degenerate Γ_8 band and a Γ_7 band. In HgTe only, the p-type Γ_8 band is energetically shifted above the s-type Γ_6 band. Therefore, HgTe has an inverted band structure, while the trivial band ordering is still preserved in CdTe [53]. Approaching an interface between HgTe and CdTe (or any trivial insulator), the bands need to reverse their order because it is not

possible to continuously transform an s-type band into a p-type band. Therefore, the bands have to cross at the interface, and the band gap vanishes. These states are the topological surface states which connect the Γ_6 bands and the Γ_8 bands of HgTe and CdTe, respectively. The described mechanism corresponds to a topological phase transition at the interface where the topological invariant changes from $\nu_0 = 1$ (HgTe) to $\nu_0 = 0$ (CdTe).

A more detailed sketch of the energy dispersion of bulk HgTe and bulk CdTe near the Γ-point is shown in figure 2.5(c-d). HgTe has no band gap and is a semimetal. However, a gap is favored as otherwise the bulk dominates the transport properties, and it is difficult to exclusively probe the surface states. Indeed, there is a way to open a gap between the Γ_8 bands: By growing HgTe on a CdTe substrate, the HgTe gets strained due to a small lattice mismatch of 0.3 % between these materials. This strain opens a small gap in the order of $15 - 20$meV [30, 54] in the bulk band structure of HgTe which is illustrated in figure 2.6(a). Here, the surface states are indicated as dashed purple lines. A simplified drawing of the bands near the band gap is shown in figure 2.6(b). From now on, the energetically highest Γ_8 band is labeled as the conduction band (CB) and the twofold degenerate Γ_8 band, which lies energetically lower, as the valence band (VB). The surface states (SS) are described by a Dirac-like dispersion where the Dirac point (DP) typically lies in the valence band.

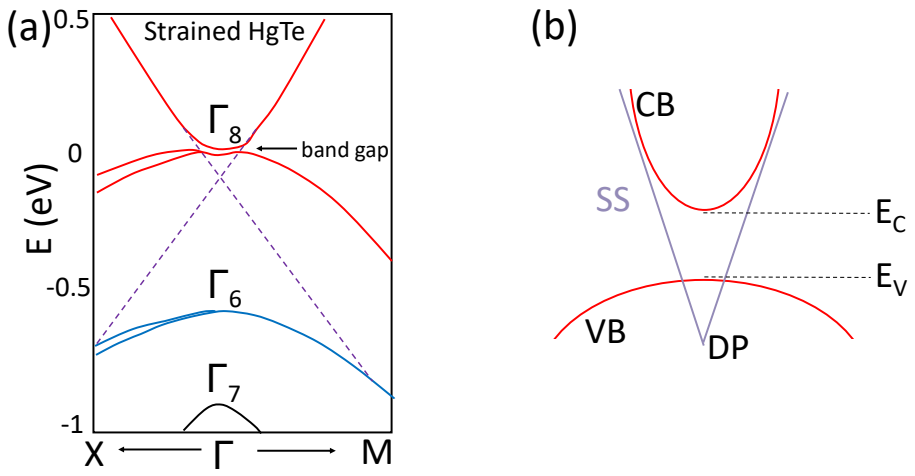

FIG. 2.6: (a) Band structure of strained HgTe. By growing HgTe on CdTe, a band gap opens in the band structure. Adapted from [55]. (b) The surface states (SS) also exist in the band gap and connect the valence band (VB) and the conduction band (CB). The Dirac point (DP) lies in the valence band. Adapted from [31].

2.1.4 Topological insulator nanowires

Let us now consider a cylindrical nanowire made from a 3D topological insulator. Since we neglect any contribution of the bulk, it can be viewed as a Dirac-like surface state wrapped around a hollow cylinder. The nanowire is assumed to be orientated along the x-axis and has the radius R as it is sketched in figure 2.7(a). The Hamiltonian of the Dirac-like surface is given by $H_{Surf} = \hbar v_F \left(\hat{k}_x \sigma_x + \hat{k}_y \sigma_y\right)$.

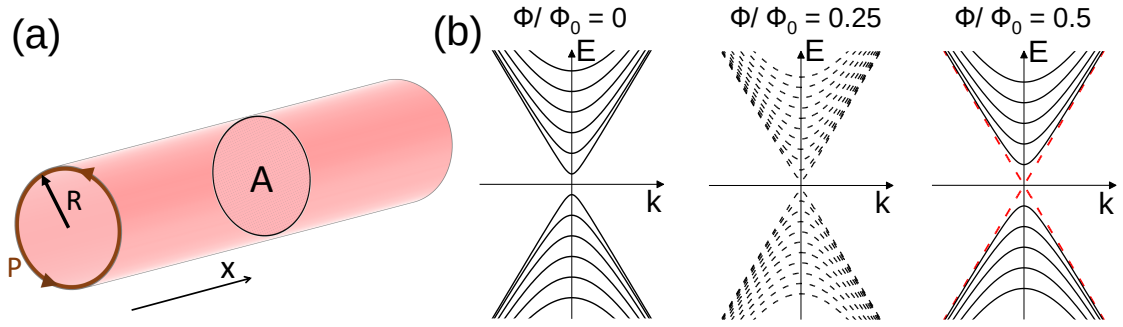

FIG. 2.7: (a) Cartoon of a nanowire with radius R and perimeter P which is orientated along the x-direction. The cross-sectional area of the wire is labeled by A. (b) Energy spectrum of a topological insulator nanowire for three characteristic values of the magnetic flux. Nondegenerate bands are visualized as dashed lines, while degenerate bands are indicated as solid lines. For $\Phi/\Phi_0 = 0$, the spectrum is gapped and the bands are degenerate. The degeneracies are lifted for $\Phi/\Phi_0 = 0.25$, but the spectrum is still gapped. For $\Phi/\Phi_0 = 0.5$, the band structure becomes gapless and linear, non-degenerate bands emerge. The other bands are twofold degenerate. Adapted from [25].

Introducing cylindrical coordinates and using a local unitary transformation[2], the Hamiltonian of the nanowire yields [56]

$$H_{Wire} = \hbar v_F \left(\hat{k}_x \sigma_x + \frac{1}{R} \hat{k}_\varphi \sigma_y\right) \tag{2.1.5}$$

with the angular coordinate φ, $\hat{k}_x = -i\partial_x$, and $\hat{k}_\varphi = -i\partial_\varphi$. When a Dirac fermion encircles the circumference of the nanowire, its spin rotates since the momentum goes in a loop. As discussed in section 2.4, this spin rotation results in a Berry phase of π. As a result, the 2π rotation of a spin gives a minus sign, and the wave function Ψ is antiperiodic:

$$\Psi(x, \varphi + 2\pi) = -\Psi(x, \varphi). \tag{2.1.6}$$

Substituting the ansatz

$$\Psi = \mathrm{e}^{-ik_x x} \mathrm{e}^{-ik_\varphi \varphi} \chi, \tag{2.1.7}$$

[2]See [56] for details of the transformation.

where χ is a two-component spinor, in equation (2.1.6) and using $-1 = \mathrm{e}^{2i\pi\ell}$ with $\ell = \pm\frac{1}{2}, \pm\frac{3}{2}, \pm\frac{5}{2}, ...$, we derive

$$k_\varphi = \ell \text{ with } \ell = \pm\frac{1}{2}, \pm\frac{3}{2}, \pm\frac{5}{2}, ... \tag{2.1.8}$$

We now add a magnetic field $\vec{B} = B\vec{e_x}$ in x-direction. This field is described by the vector potential $\vec{A} = \frac{B}{2}(-y, x, 0)$, which gives $\vec{A} = \frac{BR}{2} \cdot \vec{e_\varphi} \coloneqq A_\varphi \cdot \vec{e_\varphi}$ after a transformation in cylindrical coordinates[3]. After extending Hamiltonian (2.1.5) by the vector potential, it holds

$$H_{Wire} = \hbar v_F \left(\hat{k}_x \sigma_x + \left(\frac{1}{R}\hat{k}_\varphi + \frac{e}{\hbar} A_\varphi \right) \sigma_y \right) = \hbar v_F \left(\hat{k}_x \sigma_x + \left(\frac{1}{R}\hat{k}_\varphi + \frac{1}{R} \cdot \frac{\Phi}{\Phi_0} \right) \sigma_y \right)$$

where we used $\frac{e}{\hbar}A_\varphi = \frac{2\pi e}{h}\frac{BR^2}{2R} = \frac{\Phi}{R\Phi_0}$ with the magnetic flux threading the wires' cross-sectional area $\Phi = BR^2\pi$ and the magnetic flux quantum $\Phi_0 = h/e$. The energy spectrum is calculated by the Dirac equation $H_{Wire}\Psi = E\Psi$ which yields

$$\hbar v_F \begin{pmatrix} 0 & -i\partial_x - \frac{i}{R}\left(-i\partial_\varphi + \frac{\Phi}{\Phi_0}\right) \\ -i\partial_x + \frac{i}{R}\left(-i\partial_\varphi + \frac{\Phi}{\Phi_0}\right) & 0 \end{pmatrix} \Psi = E\Psi. \tag{2.1.9}$$

By inserting the ansatz (2.1.7) and solving the set of equations for E, we obtain the energy spectrum of the nanowire

$$E = \pm\hbar v_F \sqrt{k_x^2 + \frac{1}{R^2}\left(\ell - \frac{\Phi}{\Phi_0}\right)^2} \coloneqq \pm\hbar v_F \sqrt{k_x^2 + k_l^2} \tag{2.1.10}$$

where we defined $k_l = \frac{1}{R}\left(\ell - \frac{\Phi}{\Phi_0}\right)$. The spectrum is plotted in figure 2.7(b) for three characteristic values of the magnetic flux $\Phi/\Phi_0 = 0, 1/4, 1/2$ and $\ell = \pm 1/2, \pm 3/2, ..., \pm 9/2$. Nondegenerate bands are visualized as dashed lines in figure 2.7(b), while degenerate bands are indicated as solid lines. For $\Phi/\Phi_0 = 0$, the spectrum is gapped while the subbands are twofold degenerate with respect to angular momentum $k_\varphi = \ell$. For a flux $0 < \Phi/\Phi_0 < 1/2$, the degeneracies are lifted, but the spectrum is still gapped. By applying $\Phi/\Phi_0 = 1/2$, the magnetic flux cancels out the effect of the Berry phase, and the $\ell = +1/2$ bands become gapless and are nondegenerate. The other bands are again twofold degenerate. Further increasing of the flux leads to analogous cycles [25, 26, 56, 57]. An experimental signature of the nanowires' subband structure are conductance oscillations as a function of the Fermi level μ, i.e. an applied gate voltage, or the magnetic flux Φ. Here, maxima occur each time when μ crosses an additional subband. Such experiments were already performed in various material systems [32, 58–63] and have confirmed the band structure of topological insulator nanowires.

[3] We use $(-y, x, 0) = R\,(-sin(\varphi), cos(\varphi), 0) = R\vec{e_\varphi}$.

2.2 Superconductivity

Superconductors are a class of materials which lose their electrical resistance below a certain critical temperature T_c. A further property of superconductors is that they are perfect diamagnets and expell magnetic fields from the interior. This is called the Meissner effect. In this section, we review the microscopic theory of superconductivity by Bardeen, Cooper, and Schrieffer (BCS) [64] and extend it to the Bogoliubov-de Gennes theory which is a tool to describe unconventional and inhomogeneous superconductors. Additionally, we show that superconductivity can be induced to normal conductors by the proximity effect. An experimental setup to probe the induced superconductivity are Josephson junctions. We will introduce their basic properties and the behavior in the presence of a magnetic field and microwave radiation where so-called Shapiro steps can be observed in the I-V characteristics.

2.2.1 Microscopic theory of superconductivity

In 1957, Bardeen, Cooper, and Schrieffer [64] introduced a microscopic theory of superconductivity. The theory is based on an attractive interaction between the electrons. In the picture of only two particles, the physical idea is that an electron propagating through a crystal polarizes the medium by attracting the positive ions, i.e. the electron excites a lattice vibration and creates a phonon. Since this phonon can be absorbed by another electron, there is an effective attracting interaction between these electrons. This process is possible if the energy difference between the electrons is smaller than $\hbar\omega_D$ where ω_D is the Debye frequency. The coupling is energetically most favorable if two electrons with opposite momenta ($\pm k$) form a pair, a so-called Cooper pair. These Cooper pairs, which are bosons, condense to an energetically lower ground state while an energy gap Δ opens between the ground state of the Cooper pair condensate and the spectrum of excited single-particle states due to the pairing energy. As a consequence of this gap, scattering processes are suppressed and, therefore, the resistance of a superconductor vanishes [65–67]. The pairing mechanism described is most favorable when electrons with opposite spins are coupled. This is referred to as conventional or s-wave superconductivity. For the moment, we limit the discussion to this case. Later, we show that other pairing mechanisms are also possible.

The BCS-Hamiltonian in the second quantization formalism is given by

$$H_{BCS} = \sum_{k\sigma} \epsilon_k c^\dagger_{k\sigma} c_{k\sigma} + \sum_{kl} V_{kl} c^\dagger_{k\uparrow} c^\dagger_{-k\downarrow} c_{-l\downarrow} c_{l\uparrow}. \tag{2.2.1}$$

Here, $c_{k\sigma}$ is the annihilation operator and $c^\dagger_{k\sigma}$ is the creation operator of an electron with spin σ and momentum k. The kinetic energy ϵ_k is given relative to the

chemical potential, i.e. $\epsilon_k = \hbar^2/2m\left(\vec{k}^2 - \vec{k}_F^2\right)$ with the mass of the electron m and the Fermi wave vector $\vec{k_F}$. The scattering matrix element V_{kl} describes the interaction for a pair of electrons. The BCS-Hamiltonian is treated using a mean field approximation where two operators are expanded by their expectation value , e.g. $c^\dagger_{k\uparrow}c^\dagger_{-k\downarrow} = \langle c^\dagger_{k\uparrow}c^\dagger_{-k\downarrow}\rangle + \left(c^\dagger_{k\uparrow}c^\dagger_{-k\downarrow} - \langle c^\dagger_{k\uparrow}c^\dagger_{-k\downarrow}\rangle\right)$. Furthermore, we define

$$\Delta_k = -\sum_l V_{kl}\langle c_{-l\downarrow}c_{l\uparrow}\rangle. \tag{2.2.2}$$

The resulting mean-field Hamiltonian is given by

$$H_{MF} = \sum_{k\sigma}\epsilon_k c^\dagger_{k\sigma}c_{k\sigma} - \sum_k\left(\Delta_k c^\dagger_{k\uparrow}c^\dagger_{-k\downarrow} + \Delta^*_k c_{-k\downarrow}c_{k\uparrow} - \Delta_k\langle c^\dagger_{-k\downarrow}c^\dagger_{k\uparrow}\rangle\right). \tag{2.2.3}$$

The last term is often ignored since it only contributes a constant shift in energy. This Hamiltonian is diagonalized by using the Bogoliubov-Valatin transformation [68, 69]

$$\begin{aligned} c_{k\uparrow} &= u^*_k\gamma_{k\uparrow} + v_k\gamma^\dagger_{-k\downarrow}, \\ c^\dagger_{-k\downarrow} &= u_k\gamma^\dagger_{-k\downarrow} - v^*_k\gamma_{k\uparrow}. \end{aligned} \tag{2.2.4}$$

In particular, new fermionic operators $\gamma_{k\sigma}$ and coefficients u_k, v_k are defined. The new operators satisfy the fermionic anticommutation relations $\left\{\gamma_{k\sigma}, \gamma^\dagger_{k'\sigma'}\right\} = \delta_{kk'}\delta_{\sigma\sigma'}$ with the Kronecker delta $\delta_{kk'}$, $\{\gamma_{k\sigma}, \gamma_{k'\sigma'}\} = 0$, and the normalization condition $|u_k|^2 + |v_k|^2 = 1$. Substituting the new operators into the mean-field Hamiltonian gives

$$\begin{aligned} H_{MF} =& \sum_k\left[2\epsilon_k|v_k|^2 - \Delta_k u_k v^*_k - \Delta^*_k u^*_k v_k + \Delta_k\langle c^\dagger_{-k\downarrow}c^\dagger_{k\uparrow}\rangle\right] + \\ & \sum_k\left[\left[\epsilon_k\left(|u_k|^2 - |v_k|^2\right) + \Delta_k u_k v^*_k + \Delta^*_k u^*_k v_k\right]\left(\gamma^\dagger_{k\uparrow}\gamma_{k\uparrow} + \gamma^\dagger_{-k\downarrow}\gamma_{-k\downarrow}\right)\right] + \\ & \sum_k\left[\left(2\epsilon_k u_k v_k - \Delta_k u_k^2 + \Delta^*_k v_k^2\right)\left(\gamma^\dagger_{k\uparrow}\gamma^\dagger_{-k\downarrow}\right) + \text{h.c.}\right], \end{aligned} \tag{2.2.5}$$

where h.c. is the hermitian conjugate. The first row contains only constants, and the second row is already diagonal. Thus, the third row has to vanish in order to get a fully diagonalized Hamiltonian. Consequently, the condition is

$$2\epsilon_k u_k v_k - \Delta_k u_k^2 + \Delta^*_k v_k^2 = 0. \tag{2.2.6}$$

Solving for the ratio v_k/u_k and using $|u_k|^2 + |v_k|^2 = 1$, the result is

$$|v_k|^2 = 1 - |u_k|^2 = \frac{1}{2}\left(1 - \frac{\epsilon_k}{\sqrt{\epsilon_k^2 + |\Delta_k|^2}}\right). \tag{2.2.7}$$

With these relations, the Hamiltonian becomes

$$H_{MF} = \sum_{k\sigma} E_k \gamma^\dagger_{k\sigma} \gamma_{k\sigma} + E_0 \tag{2.2.8}$$

where we define the excitation energy

$$E_k = \pm\sqrt{\epsilon_k^2 + |\Delta_k|^2}, \tag{2.2.9}$$

and the ground-state energy E_0 which contains all constant terms [70]. The excitation spectrum E_k is plotted in figure 2.8(a) for the superconductor and the normal conductor ($\Delta_k = 0$). Note that the resulting energy spectrum is degenerate with respect to the spin. The energy spectrum of the superconductor has a gap of size $2|\Delta_k|$, while the normal-state spectrum is gapless. For the sake of simplicity, one can define V_{kl} as a constant $-V$ for energies around μ[4]. Then, Δ_k is independent of k, and we can cancel the k subscript.

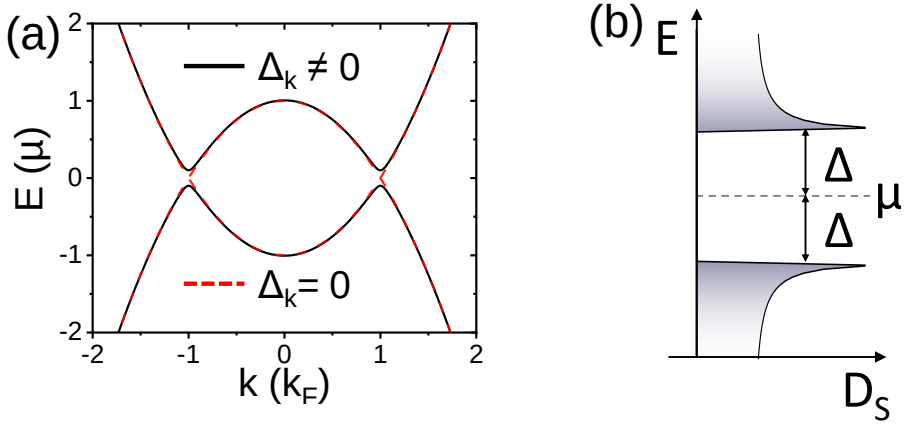

FIG. 2.8: (a) The excitation spectrum $E_k(k)$ for a superconductor ($\Delta_k \neq 0$) and a normal conductor ($\Delta_k = 0$). For the superconducting state, the spectrum has a gap of size $2|\Delta_k|$, while the normal-state spectrum is gapless. (b) Density of states D_S of a superconductor. No fermionic states are allowed inside the gap of size 2Δ around μ. Adapted from [65].

The excitations in the superconductor are described by quasiparticles, so-called Bogoliubons, which are given by the operators $\gamma^\dagger_{k\sigma}$. By inverting equation (2.2.4), we note that Bogoliubons are a mixture of electrons and holes:

$$\begin{aligned} \gamma_{k\uparrow} &= u_k^* c_{k\uparrow} - v_k c^\dagger_{-k\downarrow}, \\ \gamma^\dagger_{-k\downarrow} &= u_k^* c^\dagger_{-k\downarrow} + v_k^* c_{k\uparrow}. \end{aligned} \tag{2.2.10}$$

[4] $V_{kl} = \begin{cases} -V & \text{for } |\epsilon_k - \mu| \leq \hbar\omega_D,\ |\epsilon_l - \mu| \leq \hbar\omega_D \\ 0 & \text{otherwise} \end{cases}$ [67].

To understand the meaning of the coefficients u_k and v_k, we look at the case $\Delta_k = 0$. With equation (2.2.7), $|v_k|^2 = 1$ and $|u_k|^2 = 0$ holds for $\epsilon_k < 0$, while $|u_k|^2 = 1$ and $|v_k|^2 = 0$ for $\epsilon_k > 0$. Therefore, creating a Bogoliubon corresponds to creating an electron for $\epsilon_k > 0$ and creating a hole of opposite momentum and spin for $\epsilon_k < 0$. However, for a superconductor ($\Delta_k \neq 0$), a Bogoliubon is a superposition of an electron and a hole state.

Density of states

The density of states of a superconductor D_S is calculated by assuming the conservation of the total number of states $D_S(E)\partial E = D_N(\epsilon)\partial\epsilon$ where D_S is the density of states in the superconducting state and D_N is the density of states in the normal state. Since only energies ϵ a few millielectronvolts from the Fermi level μ are of interest, we take $D_N(\epsilon) = D_N(\mu = 0)$ as a constant. Therefore, the result is

$$D_S = D_N(0)\frac{\partial\epsilon}{\partial E} = D_N(0)\frac{\partial}{\partial E}\sqrt{E^2 - \Delta^2} = D_N(0)\begin{cases}\frac{E}{\sqrt{E^2-\Delta^2}} & \text{for } |E| > \Delta \\ 0 & \text{for } |E| < \Delta\end{cases}.$$

The spectrum of the density of states is shown in figure 2.8(b). No states are available below an energy $|E| < \Delta$. The divergent density of states at $|E| = \Delta$ are explained by the fact that all excitations $|E| < \Delta$ are raised above Δ [66].

Bogoliubov-de Gennes Hamiltonian

The previous presentation holds for homogeneous systems. If inhomogeneous systems or the combination of superconducting and normal conducting materials are investigated, we have to switch to real space. The operators in real space are achieved by Fourier transformations of the operators $c_{k\sigma}$:

$$\begin{aligned}\psi_\sigma(\vec{r}) &= \sum_k \mathrm{e}^{i\vec{k}\cdot\vec{r}} c_{k\sigma}, \\ \psi_\sigma^\dagger(\vec{r}) &= \sum_k \mathrm{e}^{-i\vec{k}\cdot\vec{r}} c_{k\sigma}^\dagger.\end{aligned} \tag{2.2.11}$$

Here, $\psi_\sigma^\dagger(\vec{r})$ creates and $\psi_\sigma(\vec{r})$ annihilates an electron at position $\vec{r}$ with spin $\sigma = \uparrow, \downarrow$. The Hamiltonian is derived analogous to the previous calculation using a mean-field approximation [71]. It yields

$$\begin{aligned}H = \int dr \Big\{ &\begin{pmatrix}\psi_\uparrow^\dagger(\vec{r}) & \psi_\downarrow^\dagger(\vec{r})\end{pmatrix} H_N(\vec{r}) \begin{pmatrix}\psi_\uparrow(\vec{r}) \\ \psi_\downarrow(\vec{r})\end{pmatrix} \\ &+ \Delta(\vec{r})\,\psi_\uparrow^\dagger(\vec{r})\,\psi_\downarrow^\dagger(\vec{r}) + \Delta^*(\vec{r})\,\psi_\downarrow(\vec{r})\,\psi_\uparrow(\vec{r})\Big\} + \text{const.}\end{aligned} \tag{2.2.12}$$

In general, the normal-state Hamiltonian H_N is a 2×2-matrix in spin space. Since excitations in a superconductor are superpositions of electron and hole states, the usage of a Hamiltonian that incorporates both the spins and electron/hole components is desirable. This is achieved by doubling the degrees of freedom by adding the redundant hole spectrum [72] to the Hamiltonian (2.2.12): Formally, we can rewrite the normal-state Hamiltonian[5]

$$\begin{pmatrix}\psi_\uparrow^\dagger & \psi_\downarrow^\dagger\end{pmatrix} H_N \begin{pmatrix}\psi_\uparrow \\ \psi_\downarrow\end{pmatrix} = \frac{1}{2}\left(\begin{pmatrix}\psi_\uparrow^\dagger & \psi_\downarrow^\dagger\end{pmatrix} H_N \begin{pmatrix}\psi_\uparrow \\ \psi_\downarrow\end{pmatrix} - \begin{pmatrix}\psi_\uparrow & \psi_\downarrow\end{pmatrix} H_N^T \begin{pmatrix}\psi_\uparrow^\dagger \\ \psi_\downarrow^\dagger\end{pmatrix} + \mathrm{Tr}\left(H_N\right)\right)$$

where $\mathrm{Tr}(H_N)$ is the trace of the matrix, and H_N^T is the transpose of the matrix. Similarly, we rewrite the pairing terms

$$\Delta\psi_\uparrow^\dagger\psi_\downarrow^\dagger + \Delta^*\psi_\downarrow\psi_\uparrow = \frac{1}{2}\left(\Delta\psi_\uparrow^\dagger\psi_\downarrow^\dagger + \Delta^*\psi_\downarrow\psi_\uparrow - \Delta\psi_\downarrow^\dagger\psi_\uparrow^\dagger - \Delta^*\psi_\uparrow\psi_\downarrow\right).$$

By applying these notations and introducing the Nambu spinor $\tilde{\Psi} = \begin{pmatrix}\psi_\uparrow & \psi_\downarrow & \psi_\uparrow^\dagger & \psi_\downarrow^\dagger\end{pmatrix}^T$, the Hamiltonian (2.2.12) is extended to

$$H \sim \frac{1}{2}\tilde{\Psi}^\dagger \begin{pmatrix} H_N & i\sigma_y\Delta \\ -i\sigma_y\Delta^* & -H_N^T\end{pmatrix}\tilde{\Psi} \coloneqq \frac{1}{2}\tilde{\Psi}^\dagger\tilde{\mathcal{H}}\tilde{\Psi}. \tag{2.2.13}$$

Here, we omitted the integral and constant terms as it is commonly done in the literature [73]. Additionally, H_N^T can be replaced by H_N^* since H_N is hermitian. The 4×4-matrix $\tilde{\mathcal{H}}$ is the so-called Bogoliubov-de Gennes (BdG) Hamiltonian.

The same problem can also be described in a different basis. The new basis is achieved by the transformation $\mathcal{H} = U\tilde{\mathcal{H}}U^\dagger$ with $U = \begin{pmatrix}\sigma_0 & 0 \\ 0 & i\sigma_y\end{pmatrix}$. The Hamiltonian in the new basis reads

$$\mathcal{H} \sim \frac{1}{2}\Psi^\dagger \begin{pmatrix} H_N & \sigma_0\Delta \\ \sigma_0\Delta^* & -\sigma_y H_N^*\sigma_y\end{pmatrix}\Psi \tag{2.2.14}$$

with $\Psi = U\tilde{\Psi} = \begin{pmatrix}\psi_\uparrow & \psi_\downarrow & \psi_\downarrow^\dagger & -\psi_\uparrow^\dagger\end{pmatrix}^T = \left(\begin{pmatrix}\psi_\uparrow & \psi_\downarrow\end{pmatrix} \Theta \begin{pmatrix}\psi_\uparrow & \psi_\downarrow\end{pmatrix}\right)^T$ where Θ is the time-reversal operator. In addition to the fact that this basis describes a quasiparticle by the spin as well as the electron/hole components, the hole operators are equal to time-reversed electron operators. This will be useful for a later argumentation. The upper left 2×2-block of the Hamiltonian $\mathcal{H}_{1,1}$ describes the electrons, while the lower right block $\mathcal{H}_{2,2}$ describes the time-reversed electrons, i.e. holes. The other 2×2-blocks $\mathcal{H}_{2,1}$ and $\mathcal{H}_{1,2}$ couple the electron and the hole block. At this point, we also introduce the Pauli matrices in the particle-hole space τ_0, τ_x, τ_y, and τ_z. They have the same form as the Pauli spin matrices, but they act on the

[5] We use the commutation relation $\psi_\alpha^\dagger H_{ij}\psi_\beta = -H_{ij}\psi_\beta\psi_\alpha^\dagger + \delta_{\alpha\beta}E_{ij} = -\psi_\beta H_{ij}^T\psi_\alpha + \delta_{\alpha\beta}E_{ij}$ with the Kronecker delta $\delta_{\alpha\beta}$.

particle-hole basis, i.e. one element of the Pauli matrices in particle-hole space corresponds to one 2×2-block of the Hamiltonian $\mathcal{H}$. Hence, the notation of $\mathcal{H}$ can be simplified by tensor multiplication of Pauli matrices in spin space and Pauli matrices in particle-hole space, e.g. it holds $\sigma_0 \otimes \tau_0 = \mathbb{1}_4$.

Bogoliubov-de Gennes equations

Up to now, we were dealing with a general normal-state Hamiltonian. For sake of simplicity, we now assume a conventional electron gas in the absence of a vector potential where $H_N(\vec{r}) = H_e\sigma_0 = [(\hbar^2/2m^*)\nabla^2 + U(\vec{r}) - \mu]\,\sigma_0$. Here, $U(\vec{r})$ is some potential, e.g. describing a barrier at an interface, m^* is the effective mass, and σ_0 is the unit matrix in spin space. The Hamiltonian (2.2.12) simplifies to

$$H \sim \psi_\uparrow^\dagger H_e \psi_\uparrow + \psi_\downarrow^\dagger H_e \psi_\downarrow + \Delta\psi_\uparrow^\dagger \psi_\downarrow^\dagger + \Delta^* \psi_\downarrow \psi_\uparrow = \begin{pmatrix} \psi_\uparrow^\dagger & \psi_\downarrow \end{pmatrix} \begin{pmatrix} H_e & \Delta \\ \Delta^* & -H_e \end{pmatrix} \begin{pmatrix} \psi_\uparrow \\ \psi_\downarrow^\dagger \end{pmatrix}. \quad (2.2.15)$$

Here, the matrix notation is derived analogous to the BdG Hamiltonian while it can be simplified to a 2×2-matrix in particle-hole space since H_N is spin degenerate. The Hamiltonian is diagonalized following the calculations of de Gennes [71] using the Bogoliubov transformation

$$\begin{aligned} \psi_\uparrow(\vec{r}) &= \sum_n \left(\gamma_{n\uparrow} u_{n\uparrow}(\vec{r}) - \gamma_{n\downarrow}^\dagger v_{n\uparrow}^*(\vec{r}) \right), \\ \psi_\downarrow(\vec{r}) &= \sum_n \left(\gamma_{n\downarrow} u_{n\downarrow}(\vec{r}) + \gamma_{n\uparrow}^\dagger v_{n\downarrow}^*(\vec{r}) \right). \end{aligned} \quad (2.2.16)$$

This transformation is an analogous version of equation (2.2.4) and corresponds to the definition of new quasiparticle operators

$$\begin{aligned} \gamma_{n\uparrow} &= \int dr \left(u_n^* \psi_\uparrow + v_n^* \psi_\downarrow^\dagger \right), \\ \gamma_{n\downarrow} &= \int dr \left(u_n^* \psi_\downarrow + v_n^* \psi_\uparrow^\dagger \right). \end{aligned} \quad (2.2.17)$$

At this point, we do not perform the full calculation and only take a look at the condition for the diagonalization. It results that the quasiparticle operators $\gamma_{n\sigma}$ diagonalize the Hamiltonian when u_n and v_n satisfy

$$\begin{pmatrix} H_e & \Delta \\ \Delta^* & -H_e^* \end{pmatrix} \begin{pmatrix} u_n(\vec{r}) \\ v_n(\vec{r}) \end{pmatrix} = E_n \begin{pmatrix} u_n(\vec{r}) \\ v_n(\vec{r}) \end{pmatrix}. \quad (2.2.18)$$

This is the so-called Bogoliubov-de Gennes (BdG) equation. The solutions of the BdG equation represented by $u_n(\vec{r})$ and $v_n(\vec{r})$ are again electron-like or hole-like quasiparticles. Both are coupled by a finite pairing potential. If $\Delta = 0$, the two rows of the BdG equation are decoupled, and we obtain the single-particle Schrödinger equations for electrons and holes. Therefore, the BdG equation can describe superconducting, normal conducting as well as hybrid systems.

2.2.2 Andreev reflection

Let us now consider an interface between a normal conductor and a superconductor as it is sketched in figure 2.9. We set $\mu = 0$ to simplify the explanation. An electron

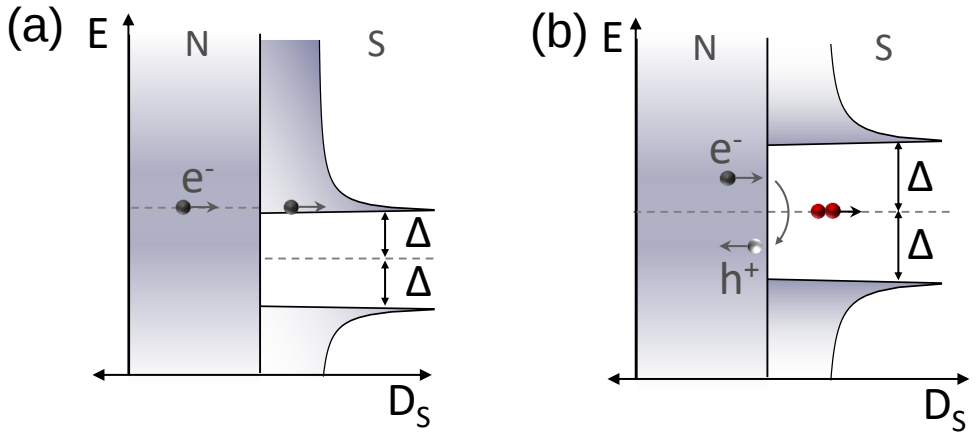

FIG. 2.9: Interface between a normal conductor (N) and a superconductor (S). (a) An electron in the normal conductor with energy $E > \Delta$ can be transmitted into the superconductor. (b) An electron with energy $E < \Delta$ cannot be transmitted into the superconductor since there are no states allowed. However, the electron can be Andreev-reflected. Here, a Cooper pair is created in the superconductor, while an additional hole emerges in the normal conductor moving in the opposite direction than the incoming electron.

with energy $E > \Delta$ (see figure 2.9(a)) in the normal conductor, which moves to the interface of the structure, can be transmitted into the superconductor. However, if an electron has an energy $E < \Delta$ (see figure 2.9(b)), it cannot be transmitted into the superconductor since there are no single-particle states allowed below $E < \Delta$. In this case, a different mechanism is possible, which is called Andreev reflection [74]. In this process, a Cooper pair is created while a second electron of the normal conductor is needed as a binding partner. Thus, a compatible electron is additionally transmitted to the superconductor. This is equivalently described by a hole with an energy $-E$ which moves in the opposite direction than the incoming electron. Therefore, two charges are transported during the process. It follows that the conductance is doubled compared to a single particle transmitted. The additional current, which is added by the enhanced conductance, is called excess current I_{exc}.

This description stands as we are dealing with perfect interfaces. In real systems, the transmissions of the interfaces are weaker, e.g. due to oxide layers or Schottky barriers. In this situation, there is only a finite probability for an incoming electron with $E < \Delta$ to be Andreev reflected. It also can be normal-reflected at the interface. The latter gives no contribution to the conductance.

A model describing these processes was introduced by Blonder, Tinkham and Klapwijk [75] and is known as BTK model. They describe the barrier at the interface as a δ-function with height h_B. Furthermore, the dimensionless parameter $Z = h_B m/\hbar^2 k_F$ is introduced which is commonly used to describe the transparency of a barrier in the literature. This parameter is related to the transmission probability D by $D = 1/(1+Z^2)$. The mechanism of Andreev reflection is important to understand the formation of a supercurrent in superconductor - normal conductor - superconductor (SNS) junctions. Such structures are also known as Josephson junctions.

2.2.3 Josephson junctions

In 1962, Brian Josephson proposed that a dissipationless current can flow through a weak link between two superconducting electrodes [76]. Assuming a thin tunnel barrier as the weak link, the problem can be addressed by a perturbative approach. In section 2.3.4, we also show a more general approach.

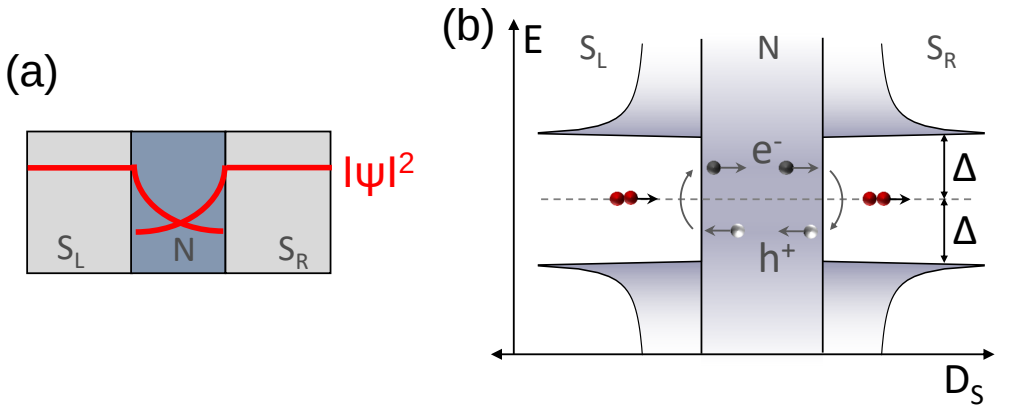

FIG. 2.10: (a) Sketch of a superconductor (S_L) - normal conductor (N) - superconductor (S_R) junction. The wave function is constant inside the superconductors, while it exponentially decays outside of the superconductor. It is possible that the wave functions overlap in the normal conductor. (b) Andreev bound state in a $S_L N S_R$ junction. An electron with energy $+E$ is Andreev-reflected at the NS_R interface. A Cooper pair is created in S_R. The reflected hole is Andreev reflected at the NS_L interface, and a hole Cooper pair is created in S_L. Here, another electron is reflected, and the process repeats.

Each superconducting electrode is described by the wave function Ψ_i where $i = L$ denotes the left and $i = R$ the right lead as it is sketched in figure 2.10(a). The wave function is constant inside a superconductor, while it decays over a finite length outside of the superconductor. If the two superconducting leads are close enough, their wave functions can overlap. Thus, we define a weak coupling constant K and

formulate the coupled Schrödinger equations

$$i\hbar\frac{\partial\Psi_{L,R}}{\partial t} = \mu_{L,R}\Psi_{L,R} + K\Psi_{R,L} \tag{2.2.19}$$

where $\mu_{L,R}$ is the chemical potential of the left (L) and the right (R) electrode. A solution of these equations is

$$\Psi_i = \sqrt{n_i}\mathrm{e}^{i\phi_i} \tag{2.2.20}$$

with the Cooper pair density n_i and the phase ϕ_i of the superconducting state. By substituting the solution into the Schrödinger equations, assuming $n = n_1 \approx n_2$, and separating real and imaginary parts, we obtain

$$\frac{\partial n}{\partial t} = \pm\frac{2Kn}{\hbar}\sin(\phi_R - \phi_L) \quad \text{and} \tag{2.2.21}$$

$$\frac{\partial\phi_{R,L}}{\partial t} = -\frac{K}{\hbar}\cos(\phi_R - \phi_L) \pm \frac{\mu_{R,L}}{\hbar}. \tag{2.2.22}$$

The resulting supercurrent I_S is defined as the number of Cooper pairs transferred from one side to the other by time:

$$I_S = -2e\frac{\partial n}{\partial t} = \frac{-4neK}{\hbar}\sin(\varphi) = I_C\sin(\varphi) \tag{2.2.23}$$

with $\varphi = \phi_2 - \phi_1$ and the critical current $I_C = |\max(I_S)|$ which is the maximum current flowing without dissipation. This relation is the first Josephson equation which connects the supercurrent with the phase difference of the superconductors' macroscopic wave functions. The second Josephson relation is derived by subtracting both versions of (2.2.22) from each other. It yields

$$\frac{\partial\varphi}{\partial t} = \frac{2eV}{\hbar} \tag{2.2.24}$$

with the voltage drop across the superconducting leads $V = (\mu_L - \mu_R)/2e$ [67]. By combining both Josephson equations, we notice that an alternating current $I_S = I_C\sin(2eVt/\hbar)$ is created for a finite voltage drop across the junction. The oscillation frequency of the supercurrent is the Josephson frequency $f_J = 2eV/h$.

Andreev bound states

In a microscopic picture, the formation of a supercurrent in an $\mathrm{S_LNS_R}$ junction can be understand by so-called Andreev bound states. Figure 2.10(b) illustrates the underlying process. We set again $\mu = 0$ to simplify the explanation. When there is no voltage drop across the junction, an electron with energy $+E$ in the normal conductor moving to the right $\mathrm{NS_R}$ interface is Andreev-reflected. Thus, a Cooper pair is created in the right electrode, and the reflected hole with energy $-E$ moves

in the opposite direction. This hole can now be Andreev-reflected at the left NS_L interface. A hole Cooper pair is created in the left electrode, which is equivalent to the annihilation of a Cooper pair. The thereby reflected electron has again the energy $+E$ and moves to the right. This is the initial condition. Therefore, this process is constantly repeated, and Cooper pairs are effectively transported from the left to the right superconducting electrode. From this description, it follows that a coherent state between the two superconductors exists.

Proximity-induced gap

The presence of the described pair correlations cause that the superconducting properties will be preserved up to a phase coherence length in the normal conductor. In particular, an induced superconducting gap Δ_i can arise in the density of states of the normal conductor [71, 77]. This is often referred to as the proximity effect. The induced gap Δ_i is typically smaller than the gap of the superconducting leads Δ. The Andreev bound states do not necessarily form inside the gap of the leads Δ, but inside the induced gap Δ_i. Hence, the induced gap is the limiting energy for the Andreev bound states. In the following theoretical description, we do not explicitly distinguish between Δ and Δ_i since we are mainly interested in the arising bound states.

Long junctions

The limiting energy changes when we deal with long junctions, i.e. a large distance between the superconducting electrodes since an electron has to travel from one lead to the other before loosing its phase coherence. The average time an electron needs in a clean junction, where the mean free path of the electrons is larger than the distance between the leads L, is $t = L/v_F$. The maximum energy where the electron keeps its phase coherence is given by the so-called Thouless energy $E_{th} = \hbar/t$ [78]. By comparing both equations, the Thouless energy is found to be $E_{th} = \hbar v_F/L$. Hence, short junctions are defined by $\Delta_i < E_{th}$, and the energy of the Andreev bound states is limited by the induced superconducting gap. In long junctions ($\Delta_i > E_{th}$), the maximum energy of the Andreev bound states is the Thouless energy E_{th}.

2.2.4 RCSJ model

The physics of Josephson junctions can be described within the resistively and capacitively shunted junction (RCSJ) model. A physical Josephson junction is modeled by an ideal one, as described by the first Josephson equation (2.2.23), shunted by a resistance and a capacitance. The circuit diagram is shown in figure

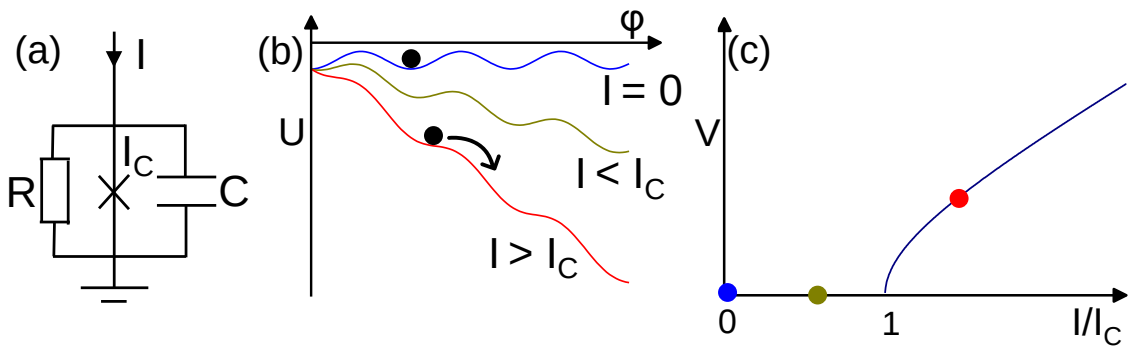

FIG. 2.11: (a) Circuit diagram of a physical Josephson junction. The ideal junction is shunted by a resistor and a capacitor. (b) Washboard potential for three different cases. If $I = 0$ or $I < I_C$, the phase particle is trapped in a minimum. When $I > I_C$, the phase particle slides down the potential. (c) I-V trace of a Josephson junction. The color of the dots corresponds to the lines in (b), respectively. As long as the particle is trapped, there is no voltage drop across the junction. A moving particle leads to a finite voltage. Adapted from [79].

2.11(a). The ideal Josephson junction models the dissipationless dc regime, the resistance the finite voltage regime, and the capacitor the geometric capacitance between the two electrodes. Within this model, the time dependence of the phase φ in the presence of an externally applied bias current I can be derived by using Kirchhoff's law:

$$I = I_S + I_{Res} + I_{Cap} = I_C \sin(\varphi) + \frac{V}{R} + C\frac{\partial V}{\partial t}. \tag{2.2.25}$$

Eliminating V by using the second Josephson equation (2.2.24) gives

$$I = I_S + I_{Res} + I_{Cap} = I_C \sin(\varphi) + \frac{\hbar}{2eR}\frac{\partial \varphi}{\partial t} + \frac{C\hbar}{2e}\frac{\partial^2 \varphi}{\partial t^2}. \tag{2.2.26}$$

We divide the equation by I_C and introduce a new time variable $\tau = \frac{2eI_C R}{\hbar}t$. This simplifies equation (2.2.26) to

$$\frac{I}{I_C} = \sin(\varphi) + \frac{\partial \varphi}{\partial \tau} + \beta_C \frac{\partial^2 \varphi}{\partial \tau^2} \tag{2.2.27}$$

where $\beta_C = \frac{2eI_C R^2 C}{\hbar}$ is the so-called Stewart-McCumber parameter [80, 81]. Despite this nonlinear differential equation is not analytically solvable, except in the limit $C = 0$, it turns out that there is a well-known analogous system, namely a particle of mass m moving along the x-axis in an effective potential U with damping η. The differential equation of such a system yields

$$m\frac{\partial^2 x}{\partial t^2} + \eta\frac{\partial x}{\partial t} + \nabla U = 0. \tag{2.2.28}$$

We can rewrite equation (2.2.27) in a similar form:

$$\left(\frac{\hbar}{2e}\right)^2 C\frac{\partial^2\varphi}{\partial t^2} + \left(\frac{\hbar}{2e}\right)^2 \frac{1}{R}\frac{\partial\varphi}{\partial t} + \frac{\partial}{\partial\varphi}\left[E_J\left(1-\cos(\varphi)-\frac{I}{I_C}\varphi\right)\right] = 0 \qquad (2.2.29)$$

with the Josephson coupling energy $E_J = \frac{\hbar I_C}{2e}$. Now, we notice the analogies: $x \Leftrightarrow \varphi$, $m \Leftrightarrow \left(\frac{\hbar}{2e}\right)^2 C$, $\eta \Leftrightarrow \left(\frac{\hbar}{2e}\right)^2 \frac{1}{R}$, and $U \Leftrightarrow E_J\left(1-\cos(\varphi)-\frac{I}{I_C}\varphi\right)$. Hence, we get a qualitative insight into the physics of Josephson junctions by considering a 'phase particle' in a so-called 'tilted washboard potential' $U = E_J\left(1-\cos(\varphi)-\frac{I}{I_C}\varphi\right)$. Figure 2.11(b) shows a plot of the potential U as a function of φ for three different externally applied currents I. The color of the lines corresponds to the dots in figure 2.11(c) where different situations are marked in the I-V trace. When no current is applied, the particle rests in a minimum, the phase φ is constant, and $\partial\varphi/\partial t = 0$. Due to the second Josephson equation (2.2.24), there is no voltage drop across the junction. By enhancing I, the slope of $U(\varphi)$ starts to tilt. However, there is still no voltage drop as long as $I < I_C$. If $I > I_C$, the particle leaves the minimum and begins to move down the potential. The phase $\varphi(t)$ changes, and there is a finite voltage drop across the junction according to the second Josephson equation (2.2.24).

In the following, we consider junctions with a negligibly small capacitance. This describes an overdamped junction with $\beta_C \ll 1$. In the picture of the washboard potential, this means that the mass of the particle is very small, and the damping term dominates. Here, the velocity of the particle is proportional to the local slope of the washboard potential due to the strong damping. Hence, the particle starts to move as soon as $dU/d\varphi < 0$ at the right side of a minimum, while the particle is trapped again when $dU/d\varphi > 0$. The resulting I-V trace is not hysteretic. Indeed, this problem ($C \to 0$) can be solved analytically. Equation (2.2.27) reduces to a first order differential, and the result is

$$V = R\sqrt{I^2 - I_C^2}. \qquad (2.2.30)$$

A possible I-V curve for an overdamped junction is shown in figure 2.12(a).

In the opposite case where C is very large and $\beta_C \gg 1$, the I-V traces become hysteretic as it is sketched in figure 2.12(b). By increasing I above I_C, V jumps to a finite voltage. This corresponds to the phase particle sliding down the potential. However, if I is decreased again, V does not drop back to zero until a retrapping current I_R is reached which is smaller than I_C[6]. In the washboard picture, this is explained by the inertia of the moving mass. When the damping is light, the moving particle can overcome a small barrier, i.e. a region with $dU/d\varphi > 0$, where it would have stopped if the damping was strong [66].

[6] $I_R \approx 4I_C/(\pi\sqrt{\beta_C})$

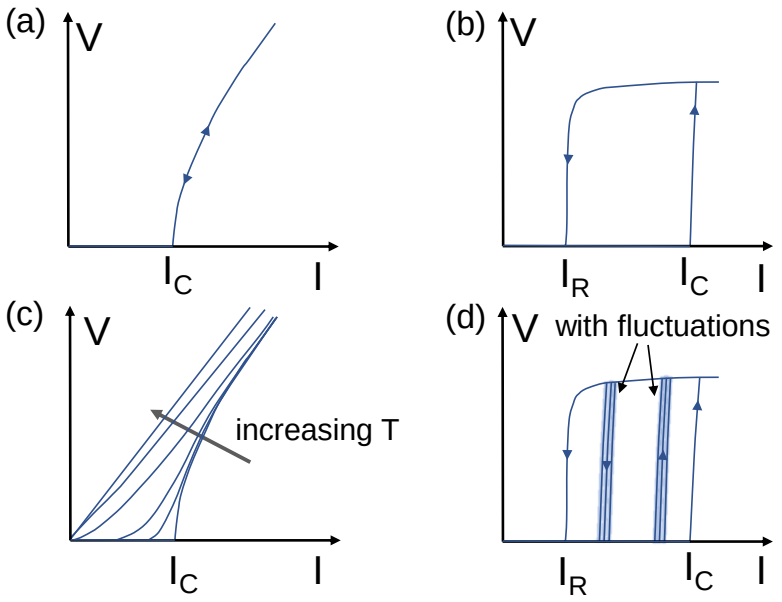

FIG. 2.12: (a) I-V trace of an overdamped junction. No hysteresis is observed. (b) I-V trace of an underdamped junction. The trace is hysteretic since the voltage V jumps to a finite value at I_C by increasing I, while it goes back to zero at $I_R < I_C$ for a decreasing I. (c) I-V trace of an overdamped junction including thermal noise. A finite resistance is always present, even for $I < I_C$. The resistance depends on the current as well as on temperature, i.e. noise strength. (d) I-V trace of an underdamped junction including noise. The switching from a finite voltage to $V = 0$ happens below I_C. Adapted from [66].

At last, thermally activated processes are taken into account. Mathematically, this is done by adding an additional fluctuation term in equation (2.2.27). Here, we limit it to a discussion within the tilted washboard model. The thermal activation can be imagined as the phase particle oscillates back and forth in the well. At each period, there is a probability that the particle escapes from the potential minimum over the barrier. Once the particle overcomes a barrier in an underdamped junction, it accelerates down the washboard potential as discussed above. Therefore, we expect a switching from a finite voltage to $V = 0$ well below I_C in the I-V characteristics. Figure 2.12(d) sketches possible traces [66].

In an overdamped junction, the situation is different. If the particle thermally escapes, it stays in the next minimum due to the strong damping until it escapes a second time. In this case, the implementation of a noise term in the model results in a finite nonlinear resistance which is always present and increases for $I \to I_C$ [82]. Corresponding I-V traces are shown in 2.12(c).

In general, the escape probability raises at higher temperature, while for $k_B T \ll E_J$ thermally activated escapes hardly play a role [66]. At this point, it is important to note that not only the temperature of the cryogenic bath defines the electron

temperature. Heating effects in the junction which depend on its resistance and the current flowing through the junction have also to be taken into account. Furthermore, electrical noise from the environment or the electric circuits can increase the electron temperature. Thus, filtering the electrical lines and shielding the sample from the environment are two important issues. These will be discussed in section 3.4.

2.2.5 Josephson junctions under microwave irradiation

If we irradiate a Josephson junction with microwaves of frequency f, steps form in the I-V traces at voltages $V_n = nhf/2e$ where n denotes integers. These steps are called Shapiro steps [38]. The microwave radiation can be taken into account by adding an additional alternating term

$$I = I_{dc} + I_{ac} \cos(\omega_{ac} t) \tag{2.2.31}$$

with $w_{ac} = 2\pi f$ in equation (2.2.26). In the picture of the washboard potential, this leads to an oscillation of the potential around a fixed position, for which $I = I_{dc}$ holds, with frequency f and amplitude I_{ac}. This scenario is sketched in figure 2.13(a) for the specific case $I_{dc} = I_C$. As long as $I_{dc} + I_{ac} > I_C$ and $I_{dc} - I_{ac} < I_C$, Shapiro steps

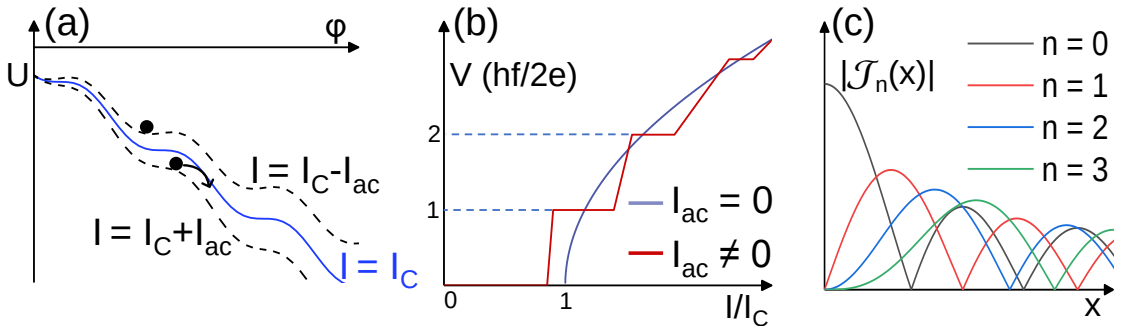

FIG. 2.13: (a) Washboard potential in the presence of microwave radiation. The slope of the potential oscillates around the position $I = I_{dc}$ with amplitude I_{ac} and frequency f. Here, the special case $I_{dc} = I_C$ is shown. (b) Comparison of the I-V traces with microwave radiation on (red) and off (blue). In the presence of microwave radiation, Shapiro steps appear at voltages $V_n = nhf/2e$ with $n = 0, 1, 2, ...$ (c) Plot of the n-th order Bessel function of the first kind. They describe the stepwidth of the n-th step, respectively. Adapted from [79].

arise. For $I_{dc} - I_{ac}$, the particle is trapped in a potential minimum, while for $I_{dc} + I_{ac}$ the particle moves down the potential. During one period of oscillation $\Delta t = 1/f$, the particle can go down n minima before it is trapped again. The resulting phase difference is $\Delta\varphi = 2\pi n$. Using the second Josephson equation (2.2.24), we obtain

$$\frac{\Delta\varphi}{\Delta t} = \frac{2eV}{\hbar} = \frac{2\pi n}{1/f}. \tag{2.2.32}$$

According to this, the constant Shapiro steps appear at voltages

$$V_n = n\frac{hf}{2e} \text{ for } n = 0, 1, 2, ... \tag{2.2.33}$$

An I-V trace of a Josephson junction in the presence of microwave radiation is shown in figure 2.13(b).

An analytic solution exists only for the ideal voltage-biased case. Here, the external voltage is written as

$$V = V_{dc} + V_{ac}\cos(\omega_{ac}t). \tag{2.2.34}$$

After replacing V by the second Josephson equation (2.2.24) and integrating the equation, we obtain

$$\varphi = \omega_0 + \frac{2eV_{ac}}{\hbar\omega_{ac}}\sin(\omega_{ac}t) + \varphi_0 \tag{2.2.35}$$

with $\omega_0 = 2eV_{dc}/\hbar$ and the constant of integration φ_0. We insert φ into the first Josephson equation (2.2.23) and use the expansion of the sine as a Bessel function where $\mathcal{J}_n$ is the n-th order Bessel function of the first kind[7]. The resulting supercurrent is

$$I_S = I_C \sum_{n=-\infty}^{\infty} (-1)^n \mathcal{J}_n\left(\frac{2eV_{ac}}{\hbar\omega_{ac}}\right)\sin((\omega_0 - n\omega_{ac})\,t + \varphi_0). \tag{2.2.36}$$

If $(\omega_0 - n\omega_{ac})\,t$ is time-dependent, there is a sum of sinusoidally varying terms which results in a time-averaged zero supercurrent. However, if $\omega_0 = n\omega_{ac}$, the expression is time-independent, and we get a dc supercurrent. This condition is equal to equation (2.2.33). The amplitude of the averaged dc current on the n-th Shapiro step is given by

$$|\langle I_S\rangle| = I_C|\mathcal{J}_n\left(\frac{2eV_{ac}}{\hbar\omega_{ac}}\right)| \tag{2.2.37}$$

which corresponds to half of the stepwidth of the n-th step. A plot of the Bessel function $|\mathcal{J}_n|$ for $n = 0$, 1, 2, 3 is shown in figure 2.13(c). By increasing the microwave amplitude V_{ac} for a fixed ω_{ac}, the width of the zero-voltage step decreases while the first step appears followed by the higher ones. For larger amplitudes, the step widths oscillate as a function of V_{ac}.

As already noted, this approach is only valid for the ideal voltage-biased case. However, an ideal voltage bias is difficult to achieve, and the junctions are mostly current-biased in the experiments. For this situation, no analytic solution exists, and numerical calculations are required to obtain the step widths. The results of Russer [83] for an ideal current-biased junction suggest that a time-averaged supercurrent is even present for $V \neq V_n$, and the oscillations of the step widths are similar to the voltage-biased case [66].

[7] $sin(a + bsin(x)) = \sum_{n=-\infty}^{\infty}(-1)^n \mathcal{J}_n(b)\,sin(a - nx)$.

2.2.6 Josephson junctions in a magnetic field

The presence of a magnetic field can have various effects on Josephson junctions. Typically, a magnetic field acts as a pair breaking mechanism for Cooper pairs [84–87]. Here, the superconducting gap Δ is monotonously reduced by a magnetic field. However, even magnetic fields which are too low to play a role for the pair breaking can cause a variation of the supercurrent. The most prominent example is the formation of a so-called Fraunhofer pattern which arises in the presence of an out-of-plane magnetic field. We derive its origin by considering a 2D Josephson junction in the xy-plane as it is shown in figure 2.14(a). The current flows along the

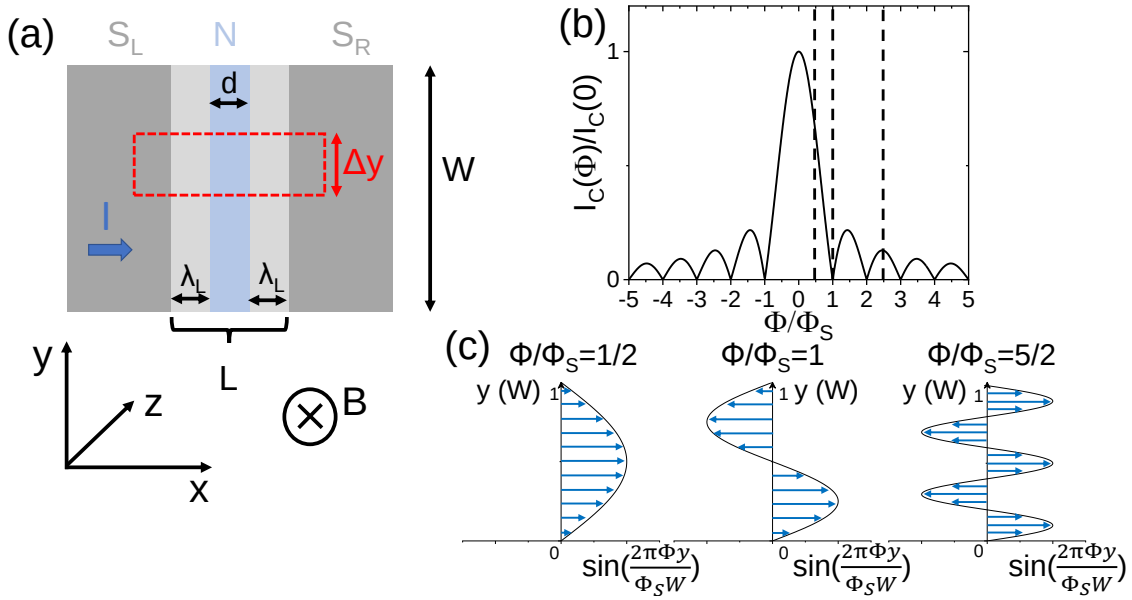

FIG. 2.14: (a) Sketch of a 2D Josephson junction in the xy-plane while the magnetic field B is orientated along the z-direction. The magnetic flux threading the area of the red rectangle is $\Delta\Phi = BL\Delta y$ while the flux penetrating the whole area of the junction is $\Phi = BWL$. (b) The normalized critical current $I_C(\Phi)/I_C(0)$ as a function of the magnetic flux. The trace resembles the Fraunhofer diffraction pattern. The dashed lines correspond to the situations described in (c). (c) Local distribution of the supercurrent along the y-axis for three different values of the magnetic flux Φ. For integer multiples of the superconducting flux quantum, the local supercurrent flowing in opposite directions cancel each other (middle panel). Thus, $I_C = 0$. Between these values a net positive current remains (left and right panel). Adapted from [88].

x-axis while d is the distance between the superconducting contacts, and W is the width of the junction. It is well known that an applied magnetic field B enters a superconductor up to the London penetration depth λ_L [89]. Thus, we define the effective length of the junction $L = d + 2\lambda_L$. We take a look at the magnetic flux $\Delta\Phi$ through a rectangular area A with an infinitesimally small width $\Delta y \to 0$. For the

sake of visualization, we sketch an area by red dashed lines in figure 2.14(a). The magnetic flux is given by $\Delta\Phi = BA = BL\Delta y$. In addition to the phase difference between the superconducting leads φ, there is now an additional phase difference caused by the magnetic flux $\Delta\varphi = 2\pi\Delta\Phi/\Phi_S = 2\pi BL\Delta y/\Phi_S$. Here, we explicitly use the superconducting flux quantum $\Phi_S = h/2e$. Thus, it holds

$$\frac{\Delta\varphi}{\Delta y} = \frac{2\pi BL}{\Phi_S}. \tag{2.2.38}$$

Introducing the magnetic flux through the whole area of the junction $\Phi = BLW$ and integrating equation (2.2.38), we obtain

$$\varphi(y) = \frac{2\pi\Phi}{W\Phi_s} y + \varphi_0 \tag{2.2.39}$$

where φ_0 is a constant of integration. The local Josephson current $j_S(y)$ is given by $j_S(y) = j_C(y)\sin[\varphi(y)]$ analogous to the first Josephson equation (2.2.23) where j_C is the critical current density. Assuming an uniform current distribution along the junction, $j(y) = I_C(B=0)/W$ holds. By integrating over the total width of the junction, we get the Josephson supercurrent

$$I_S(\Phi) = \int_{-W/2}^{W/2} \frac{I_C(0)}{W} \sin\left(\frac{2\pi\Phi}{W\Phi_S} y + \varphi_0\right) = I_C(0)\,\frac{\sin(\pi\Phi/\Phi_S)}{\pi\Phi/\Phi_S}\sin(\varphi_0). \tag{2.2.40}$$

We reach the maximum Josephson current $\max[I_S(\Phi)] = I_C(\Phi)$ by maximizing the equation with respect to φ_0:

$$I_C(\Phi) = I_C(0)\left|\frac{\sin(\pi\Phi/\Phi_S)}{\pi\Phi/\Phi_S}\right|. \tag{2.2.41}$$

The resulting critical current $I_C(\Phi)$ is visualized in figure 2.14(b). Due to the similarity to the optical phenomenon, this is referred to as the Fraunhofer diffraction pattern. For a deeper understanding of the current flow in the Josephson junction with an applied magnetic field, we look at the spatial distribution $j_S(y) \sim \sin[\varphi(y)]$. Figure 2.14(c) shows the distribution of $j_S(y)$ with $\varphi_0 = 0$ along y for three values of the magnetic flux. For $\Phi/\Phi_S = 1/2$, the phase shift due to the magnetic field $\varphi(y)$ lies between 0 and π in the range $y = 0 - W$ according to equation (2.2.39). This gives a positive net current which is already reduced compared to the situation of zero flux. When the flux is an integer multiple of the flux quantum $\Phi = n\Phi_S$, the total critical current is zero since the supercurrent has equal amounts flowing in both directions. Between these points, the net critical current is positive, as exemplarily shown for $\Phi/\Phi_S = 5/2$, since a part of the supercurrent is not compensated by a current running in the opposite direction.

As a regular Fraunhofer pattern only arises for a homogeneous current distribution, its appearance in the experiment indicates a high quality of the interface between the normal conductor and the superconducting contacts. An inhomogeneous distribution of the supercurrent leads to deviations from the ideal Fraunhofer pattern.

2.3 Topological superconductivity

The concept of topology can also be applied to superconductors. So-called topological superconductors are characterized by zero-energy states which are localized at their boundaries. These are known as Majorana bound states. In this section, we introduce the Majorana bound states and show how they emerge in 1D p-wave superconductors. An effective 1D p-wave superconductor is also realized by the combination of a topological insulator nanowire and an s-wave superconductor. Since our experiments are performed on such a system, we take a closer look at the theoretical proposal for the emergence of Majorana bound states in topological insulator nanowires.

2.3.1 Unconventional superconductivity

Until now, we have only dealt with s-wave superconductivity which is referred to as conventional superconductivity. Here, Cooper pairs are formed due to an attractive interaction among electrons with opposite spins s, s'. This is the most symmetric form of pairing where the relative orbital angular momentum vanishes, and the spin is in singlet configuration. The pair wavefunction of the Cooper pairs is given by

$$\Psi\left(\vec{r}, s; \vec{r}', s'\right) = f\left(|\vec{r} - \vec{r}'|\right) \chi\left(s, s'\right) \tag{2.3.1}$$

where $f\left(\vec{r}\right)$ describes the orbital part of the wavefunction and χ the spin part. In any case, the wave function has to be antisymmetric when inverting the two electrons of the Cooper pair. For a conventional superconductor, the spin part is antisymmetric: $\chi\left(s, s'\right) = -\chi\left(s', s\right)$. Thus, the orbital part is symmetric and fulfills $f\left(-\vec{r}\right) = f\left(\vec{r}\right)$.

All superconductors that deviate from this rule are called unconventional superconductors. Here, the spin part could be symmetric $\chi\left(s, s'\right) = \chi\left(s', s\right)$, while the orbital part is antisymmetric $f\left(-\vec{r}\right) = -f\left(\vec{r}\right)$ [90]. In the following, we take a look to one of the simplest form of unconventional pairing, namely p-wave pairing in one dimension. The asymmetry of the orbital part is achieved by a constant pairing potential, which changes its sign depending on the direction of the particles' propagation [27, 28]. Before explicitly calculating the energy spectrum of an 1D p-wave superconductor, we point out why p-wave superconductivity is an important building block for the occurrence of Majorana bound states.

2.3.2 Majorana fermions in condensed matter physics

The complex Dirac equation, which was established by Paul Dirac in 1930 [91], describes fermionic particles with spin 1/2. While the positive-energy solutions

describe electrons, the negative-energy solutions correspond to their antiparticles, the positrons, which have the same mass and spin but opposite charge. Both particles are related by the complex conjugate of its wave function, respectively. In 1937, Ettore Majorana proposed that the complex Dirac equation can be separated in a pair of real wave functions [11]. This solution describes a so-called Majorana fermion. It is a particle which is its own antiparticle. Thus, it holds

$$\gamma = \gamma^\dagger \tag{2.3.2}$$

for its annihilation and creation operator [92]. So far, it is still not clear if there are elementary particles which are Majorana fermions, e.g. neutrinos are potential candidates [93].

However, Majorana fermions are also proposed in condensed matter physics. Here, they are not free particles. They exist as quasiparticle excitations, so-called Majorana bound states. These states have attracted a lot of theoretical interest since they obey non-Abelian exchange statistics and, therefore, could serve as a platform for topological quantum computation [10].

In principle, any fermion can be separated into two Majorana fermions:

$$\begin{aligned} c &= \frac{1}{2}(\gamma_1 + i\gamma_2), \\ c^\dagger &= \frac{1}{2}(\gamma_1 - i\gamma_2) \end{aligned} \tag{2.3.3}$$

with the fermionic annihilation and creation operators c and $c^\dagger$. Normally, this has no physical consequences because the two Majorana fermions are localized close to each other and cannot be addressed individually. Therefore, Majorana fermions become only interesting when they are spatially separated and do not overlap [94]. Inverting equation (2.3.3) gives

$$\begin{aligned} \gamma_1 &= c^\dagger + c, \\ \gamma_2 &= i\left(c^\dagger - c\right). \end{aligned} \tag{2.3.4}$$

It follows that a Majorana fermion can be viewed as an equal superposition of an electron and a hole. Therefore, superconductors turn up as a potential platform since their quasiparticle excitations are also superpositions of electrons and holes. In the Bogoliubov-de Gennes formalism, which was introduced in section 2.2.1, the annihilation operator of a Majorana fermion, i.e. a quasiparticle with equal weight of an electron-like and a hole-like excitation, reads $\gamma = v_n c_\sigma^\dagger + u_n c_\sigma$ with $u_n = v_n$ and spin σ. This operator fulfills the condition $\gamma = \gamma^\dagger$. Since $u_n = v_n$, we expect an excitation exactly between electron-like and hole-like excitations, i.e. with excitation energy $E = 0$. In contrast to the s-wave annihilation operator of a Bogoliubon (see

equation (2.2.10)) where the fermion operators have opposite spin[8], the fermion operators creating a Majorana fermion have equal spin [94]. Thus, such quasiparticles do not exist in s-wave superconductors. However, if the pairing of spinless fermions is assumed, the annihilation operator of a Bogoliubon does not have spin indices, and it holds $\gamma = \gamma^\dagger$. The Cooper pair wavefunction of such spinless fermions has no spin part. Since the Cooper pair wavefunction must be antisymmetric due to the Pauli principle, the antisymmetry must be in the orbital part. Therefore, s-wave pairing, where the antisymmetry is in the spin part and the orbital part is symmetric, is not possible. Though, the antisymmetry in the orbital part could be achieved by p-wave pairing. Using this heuristic arguments, it follows that Majorana bound states emerge as zero-energy excitations in spinless p-wave superconductors [95]. In the next section, we explicitly show their emergence at the boundaries of an 1D p-wave superconductor.

2.3.3 Majorana fermions in an 1D p-wave superconductor

The Hamiltonian of an 1D spinless superconductor is given by

$$H = \sum_k c_k^\dagger \epsilon_k c_k + \frac{1}{2}\left[\Delta c_k^\dagger c_{-k}^\dagger + \Delta^* c_k c_{-k}\right]. \tag{2.3.5}$$

We focus on the situation where $\epsilon_k = \hat{p}^2/2m - \mu$ describes an 1D metal of spinless or spin-polarized fermions. Since a momentum-independent s-wave pairing is not possible, we introduce a momentum-dependent p-wave potential $\Delta = \Delta_0 \hat{p}$ where Δ_0 is a constant pairing potential and $\hat{p} = -i\hbar\partial_x$ is the momentum operator. The Hamiltonian can be diagonalized using the Bogoliubov-Valatin transformation (2.2.4) without spin indices $c_k = u_k^* \gamma_k + v_k \gamma_{-k}^\dagger$. Analogous to section 2.2.1, we derive

$$\begin{aligned} E &= \pm\sqrt{\left(p^2/2m - \mu\right)^2 + |\Delta_0|^2 p^2}, \\ v_k &= \sqrt{\frac{1}{2}\left(1 - \frac{\epsilon_k}{E}\right)}\frac{\Delta^*}{|\Delta|} \text{ and } u_k = \sqrt{\frac{1}{2}\left(1 + \frac{\epsilon_k}{E}\right)}. \end{aligned} \tag{2.3.6}$$

The functions u_k and v_k are determined only up to an overall phase. Thus, they can be multiplied by a phase $e^{i\varphi}$ without changing any physics [96]. The energy spectrum $E(k)$ for $\Delta_0 \neq 0$ is plotted as black lines in figure 2.15 for three different cases. The spectrum is gapped for $\mu > 0$ as well as for $\mu < 0$, while it becomes gapless for $\mu = 0$. This is the important difference to the s-wave pairing where the system is gapped even for $\mu = 0$. The cases $\mu > 0$ and $\mu < 0$ describe different topological phases. While the phase for $\mu > 0$ is called weak-pairing phase, $\mu < 0$ describes the strong-pairing phase. They cannot be adiabatically connected to each other without

[8] Here, $\gamma \neq \gamma^\dagger$.

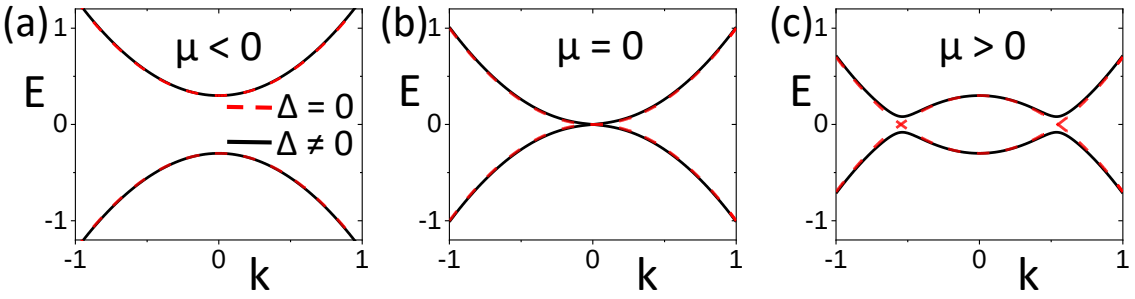

FIG. 2.15: Energy spectrum of a 1D p-wave superconductor (black lines). For comparison, the spectrum is also shown in the absence of pairing $\Delta = 0$ (red dashed lines). (a) For $\mu < 0$, the spectrum is gapped for $\Delta \neq 0$ and $\Delta = 0$. Both states are topologically equivalent to the trivial insulating state. (b) The spectra become gapless for $\mu = 0$. (c) For $\mu > 0$, the energy spectrum is gapless if $\Delta = 0$, while it is gapped for $\Delta \neq 0$. Since the latter case cannot be transformed to the trivial insulating state without closing the gap, it describes a nontrivial topological phase. Adapted from [97].

closing the band gap. Thus, one of them is expected to have a nontrivial topology. To derive the topological phase, we additionally show the spectra for $\Delta = 0$ as red dashed lines in figure 2.15. For $\mu < 0$, the system is a gapped trivial insulator. By turning on Δ, the system remains gapped. Hence, this phase can be adiabatically connected to the trivial insulating phase. When $\mu > 0$ and $\Delta = 0$, the system is metallic, i.e. gapless. It becomes only gapped for a finite Δ. By trying to connect the phase $\mu > 0$ and $\Delta \neq 0$ to the trivial insulating phase where $\mu < 0$ and $\Delta = 0$, we always have to pass a gapless point or region [97]. Thus, there is a topological phase transition, and the system is topologically nontrivial for $\mu > 0$ and $\Delta \neq 0$. Therefore, zero-energy bound states exist at the boundary between the topological system and any trivial system. We explicitly show that by considering a boundary at the position $x = 0$ between the weak-pairing ($x > 0$) and the strong-pairing ($x < 0$) phase, i.e. we define $\mu(x) = \mu_0$ for $x > 0$ and $\mu(x) = -\mu_0$ for $x < 0$. Furthermore, the BdG equations in real space have to be used which are analogously derived as in section 2.2.1. The BdG equations take the form

$$\begin{pmatrix} \frac{\hat{p}^2}{2m} - \mu(x) & \Delta_0 \hat{p} \\ \Delta_0^* \hat{p} & -\frac{\hat{p}^2}{2m} + \mu(x) \end{pmatrix} \begin{pmatrix} u_n(x) \\ v_n(x) \end{pmatrix} = E \begin{pmatrix} u_n(x) \\ v_n(x) \end{pmatrix}. \tag{2.3.7}$$

For the sake of simplicity, we set $\hbar = 1$. Thus, $\hat{p} = \hat{k} = -i\partial_x$. In the limit of small k, i.e. neglecting quadratic terms, and looking for zero-energy solutions, it holds

$$\begin{pmatrix} -\mu(x) & -\Delta_0 \partial_x \\ -\Delta_0^* \partial_x & \mu(x) \end{pmatrix} \begin{pmatrix} u_n(x) \\ v_n(x) \end{pmatrix} = 0. \tag{2.3.8}$$

We take the ansatz[9]

$$\begin{pmatrix} u_n(x) \\ v_n(x) \end{pmatrix} = \mathrm{e}^{-\frac{1}{\Delta_0}\int_0^x \mu(x')dx'} \begin{pmatrix} u_0 \\ v_0 \end{pmatrix} \tag{2.3.9}$$

and insert it into equation (2.3.8). This gives

$$\begin{pmatrix} -\mu(x) & i\mu(x) \\ i\mu(x) & \mu(x) \end{pmatrix} \begin{pmatrix} u_0 \\ v_0 \end{pmatrix} = 0. \tag{2.3.10}$$

A solution of this equation is given by

$$\begin{pmatrix} u_0 \\ v_0 \end{pmatrix} = \frac{1}{\sqrt{2}} \begin{pmatrix} 1 \\ -i \end{pmatrix}. \tag{2.3.11}$$

This solution inserted into the ansatz describes a zero-energy mode localized at the boundary. The annihilation operator of the corresponding Bogoliubon is given by the spinless version of equation (2.2.17):

$$\gamma = \int dx \left[u_n^*(x)\,\psi(x) + v_n^*(x)\,\psi^\dagger(x) \right] = \frac{1}{\sqrt{2}} \int dx\, \mathrm{e}^{-\frac{1}{\Delta_0}\int_0^x \mu(x')dx'} \left[\psi(x) + i\psi^\dagger(x) \right].$$

Using $i = \mathrm{e}^{-i\pi/2}$, we derive

$$\gamma = \frac{\mathrm{e}^{i\pi/4}}{\sqrt{2}} \int dx\, \mathrm{e}^{-\frac{1}{\Delta_0}\int_0^x \mu(x')dx'} \left[\mathrm{e}^{-i\pi/4}\psi(x) + \mathrm{e}^{i\pi/4}\psi^\dagger(x) \right]. \tag{2.3.12}$$

After removing the overall phase of $\pi/4$, we notice that $\gamma = \gamma^\dagger$ holds, and the operator describes a Majorana fermion [97].

There is also a topological invariant describing topological superconductivity in one dimension. This invariant is called Majorana number $\mathcal{M}$ and was firstly introduced by A. Kitaev [12]. This number can take the values $\mathcal{M} = \pm 1$, while the trivial phase is labeled with $\mathcal{M} = 1$. The nontrivial phase is described by $\mathcal{M} = -1$ and is expected to have zero-energy modes at the boundaries. Although the general determination is very complicated, the derivation of the Majorana number simplifies to

$$\mathcal{M} = (-1)^\nu \tag{2.3.13}$$

in the limit of a small pairing potential Δ. The exponent ν counts the number of points crossing the Fermi energy in the right half of the Brillouin zone of the normal spectrum, i.e. the energy spectrum of the underlying system including all degeneracies without introducing superconductivity. The second important criterion for the appearance of zero-energy modes at the boundaries is that a finite energy gap evolves when superconductivity is induced. In the original publication from 2001,

[9] The equations to solve take the same form as in the work of Jackiw and Rebbi [98]. It differs in the fact that they investigated a sign change of the mass at a boundary.

Kitaev stated that the gap has to be induced by proximity of a p-wave superconductor. Since p-wave superconductors are very rare in nature as well as they are not well understood [13], a possible realization was far away at that time. However, after the emergence of topological insulators, Fu and Kane [14] discovered that the induction of s-wave superconductivity to the surface states of a topological insulator leads to an effective p-wave superconductor. Therefore, we expect the emergence of Majorana fermions in topological insulators with $\mathcal{M} = -1$ where a superconducting gap Δ is induced by proximity to an s-wave superconductor.

2.3.4 4π-Josephson effect

In the previous section, we showed that Majorana fermions can emerge at boundaries of an 1D p-wave superconductor. However, an experimental signature is needed to distinguish effective s-wave and p-wave pairing. Hence, we will derive the Andreev bound state spectrum of a junction made of an 1D p-wave superconductor which is orientated along the x-axis following Kwon et. al. [27, 28]. A cartoon of the device is sketched in figure 2.16. Additionally, we simultaneously calculate the spectrum for s-wave pairing, point out the differences, and explain the different signatures in the experiments. The Hamiltonian of the 1D conductor in the normal state is given by $H_N = \hbar^2 \hat{k}_x^2/2m - \mu + U(x)$ where $\hat{k}_x = -i\partial_x$. The weak link is described by a potential barrier $U = U_0 \delta(x)$ at the position $x = 0$ between the left and right electrode. It is worth to mention that the following calculations are only valid for short junctions as we assume an infinitesimally small weak link. The calculations will be shown assuming an s-wave pairing potential as well as a p-wave pairing potential. They can be written as

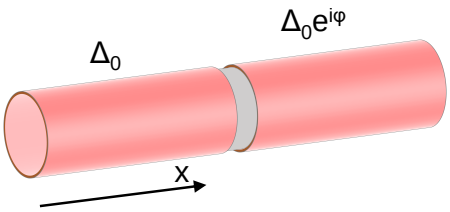

FIG. 2.16: Sketch of a 1D superconducting nanowire orientated along the x-axis. The weak link (gray) separates the left ($\Delta_L = \Delta_0$) and right electrode ($\Delta_R = \Delta_0 e^{i\varphi}$). Adapted from [27].

$$\Delta_\beta(x, \hat{k}_x) = \begin{cases} \Delta_\beta & \text{for s-wave pairing} \\ \Delta_\beta \frac{\hat{k}_x}{k_F} & \text{for p-wave pairing.} \end{cases} \tag{2.3.14}$$

Here, $\beta = R$ labels the right ($x > 0$) and $\beta = L$ the left ($x < 0$) side of the junction with $\Delta_L = \Delta_0$ and $\Delta_R = \Delta_0 e^{i\varphi}$ where φ is the superconducting phase difference across the junction. Thus, the s-wave pairing is described by a constant pairing potential Δ_0, while the p-wave pairing potential changes its sign depending on the direction of the particles' propagation. The BdG equation yields

$$\begin{pmatrix} H_N(x) & \Delta_\beta\left(x, \hat{k}_x\right) \\ \Delta_\beta^*\left(x, \hat{k}_x\right) & -H_N(x) \end{pmatrix} \Psi_n = E_n \Psi_n. \tag{2.3.15}$$

A general solution is a superposition of right and left moving particles with momenta close to αk_F where $\alpha = \pm$ labels the right- and left-moving electrons, and β is ± 1 for L and R when it is used as a factor. The ansatz takes the form

$$\Psi_\beta = \left[A_\beta \begin{pmatrix} u_{\beta+} \\ v_{\beta+} \end{pmatrix} \mathrm{e}^{ik_F x} + B_\beta \begin{pmatrix} u_{\beta-} \\ v_{\beta-} \end{pmatrix} \mathrm{e}^{-ik_F x} \right] \mathrm{e}^{\beta\kappa x}. \tag{2.3.16}$$

This wave function decays exponentially with increasing distance from the interface with the length $1/\kappa$. The coefficients $u_{\beta\alpha}$ and $v_{\beta\alpha}$ are determined by substituting the right- and left-moving terms separately into equation (2.3.15) at $x \neq 0$ where $U(x) = 0$. Assuming p-wave pairing, the equation for the coefficients in the limit $k_F \gg \kappa$[10] and with $\hbar^2 k_F^2/2m = \mu$ reads

$$\begin{pmatrix} \frac{\hbar^2}{2m}(-2i\alpha\beta\kappa k_F) - E & \tilde{\alpha}\Delta_\beta \\ \tilde{\alpha}\Delta_\beta^* & -\frac{\hbar^2}{2m}(-2i\alpha\beta\kappa k_F) - E \end{pmatrix} \begin{pmatrix} u_{\beta\alpha} \\ v_{\beta\alpha} \end{pmatrix} = \begin{pmatrix} 0 \\ 0 \end{pmatrix}. \tag{2.3.17}$$

At this point, we want to address how this equation changes if we assume s-wave pairing. To illustrate the difference, we introduced $\tilde{\alpha}$. In the case of p-wave pairing, the factor α equals $\tilde{\alpha}$, while the factor $\tilde{\alpha}$ vanishes ($\tilde{\alpha} = +1$) for s-wave pairing, and only α remains. The equations (2.3.17) are compatible if the determinant of the corresponding matrix is zero. Evaluating this determinant and solving for κ gives

$$\kappa = \frac{m\sqrt{\Delta_\beta^2 - E^2}}{\hbar^2 k_F}. \tag{2.3.18}$$

Furthermore, we solve one equation of (2.3.17) for $v_{\beta\alpha}/u_{\beta\alpha}$ and plug in κ. It yields

$$\eta_{\beta\alpha} \coloneqq \frac{v_{\beta\alpha}}{u_{\beta\alpha}} = \frac{E - i\alpha\beta\kappa\frac{\hbar^2 k_F}{m}}{\tilde{\alpha}\Delta_\beta} = \frac{E - i\alpha\beta\sqrt{\Delta_\beta^2 - E^2}}{\tilde{\alpha}\Delta_\beta}. \tag{2.3.19}$$

In the next step, we find the boundary conditions at $x = 0$. Due to the continuity of the wave functions, the first condition is

$$\Psi_R(x = 0) = \Psi_L(x = 0). \tag{2.3.20}$$

The derivatives are not continuous because of the δ-potential. However, the relation of the derivatives is found by integrating the BdG equation (2.3.15) around an infinitesimally small range[11]. Thus, the second boundary condition is

$$\partial_x \Psi_R(x = 0) - \partial_x \Psi_L(x = 0) = \frac{2mU_0}{\hbar^2} \Psi_{L=R}(x = 0). \tag{2.3.21}$$

[10] In the calculations, we assume $\kappa/ik_F \to 0$.

[11] For $\epsilon > 0$ and $\Psi_\beta = \begin{pmatrix} \Psi_{\beta 1} \\ \Psi_{\beta 2} \end{pmatrix}$, we exemplarily integrate the first equation for p-wave pairing:

$$0 = \lim_{\epsilon\to 0} \int_{-\epsilon}^{\epsilon} E\Psi_{\beta 1} dx = \lim_{\epsilon\to 0} \int_{-\epsilon}^{\epsilon} \left[\left(-\frac{\hbar^2 \partial_x^2}{2m} + U_0 \delta(x) \right) \Psi_{\beta 1} + \Delta_\beta \frac{-i\partial_x}{k_F} \Psi_{\beta 2} \right] dx =$$

By substituting equation (2.3.16) into the first boundary condition (2.3.20) as well as into the second boundary condition (2.3.21), we get the set of equations in the limit $k_F \gg \kappa$:

$$\begin{pmatrix} u_{L+} & -u_{R+} & u_{L-} & -u_{R-} \\ v_{L+} & -v_{R+} & v_{L-} & -v_{R-} \\ (2Z+i)u_{L+} & -iu_{R+} & (2Z-i)u_{L-} & iu_{R-} \\ (2Z+i)v_{L+} & -iv_{R+} & (2Z-i)v_{L-} & iv_{R-} \end{pmatrix} \begin{pmatrix} A_L \\ A_R \\ B_L \\ B_R \end{pmatrix} = \begin{pmatrix} 0 \\ 0 \\ 0 \\ 0 \end{pmatrix}. \tag{2.3.22}$$

Here, we defined $Z = mU_0/\hbar^2$ analogous to the BTK theory [75]. The determinant of this matrix has to be equal to zero to achieve compatible equations. By evaluating this determinant and introducing the transmission D, which is related to Z by $Z = \sqrt{(1-D)/D}$, we obtain

$$1 - D = \frac{(u_{R+}v_{L+} - u_{L+}v_{R+})\,(u_{L-}v_{R-} - u_{R-}v_{L-})}{(u_{L+}v_{R-} - u_{R-}v_{L+})\,(u_{R+}v_{L-} - u_{L-}v_{R+})}. \tag{2.3.23}$$

By using $\eta_{\beta\alpha} = v_{\beta\alpha}/u_{\beta\alpha}$, it simplifies to

$$1 - D = \frac{(\eta_{R-} - \eta_{L-})\,(\eta_{R+} - \eta_{L+})}{(\eta_{R+} - \eta_{L-})\,(\eta_{R-} - \eta_{L+})}. \tag{2.3.24}$$

We plug in $\eta_{\beta\alpha}$ for the s-wave case which is given by equation (2.3.19) ($\tilde{\alpha} = +1$) and use $\Delta_L = \Delta_0$, $\Delta_R = \Delta_0 e^{i\varphi}$. Solving this equation for E yields

$$E_{\pm}^{\text{s-wave}} = \pm\Delta_0\sqrt{1 - D\sin^2(\varphi/2)}. \tag{2.3.25}$$

This is the Andreev bound state spectrum for s-wave pairing. Analogously, we insert equation (2.3.19) in equation (2.3.24) to obtain the Andreev bound state spectrum for p-wave pairing:

$$E_{\pm}^{\text{p-wave}} = \pm\Delta_0\sqrt{D}\cos(\varphi/2). \tag{2.3.26}$$

The resulting Andreev bound state spectrum for s-wave and p-wave pairing is plotted in figure 2.17(a, d), respectively. In the s-wave case, the spectrum is 2π-periodic in φ for any value of D, except for perfect transmission $D = 1$. However, a perfect transmission is hardly reachable in realistic systems. Therefore, there always exists a gap at $\varphi = \pi$. For p-wave pairing, the spectrum is 4π-periodic in φ for any value of D while a value $D < 1$ opens a gap between the bound states and the continuum at $\varphi = n \cdot 2\pi$ with $n = 0, 1, 2, ...$ The periodicity and the crossing point at $E(\varphi = \pi) = 0$ remains unaffected by D.

$$\frac{-\hbar^2\partial_x}{2m}\Psi_{R1}(0) + \frac{\hbar^2\partial_x}{2m}\Psi_{L1}(0) + U_0\Psi_{R1}(0) + \frac{-i\Delta_\beta}{k_F}\left(\Psi_{R2}(0) - \Psi_{L2}(0)\right)$$

where the last term vanishes due to the first boundary conditions. The second equation gives the corresponding equation, where $\Psi_{\beta 2}$ and $\Psi_{\beta 1}$ are exchanged. For s-wave pairing, the calculation works analogous while the final boundary condition is the same.

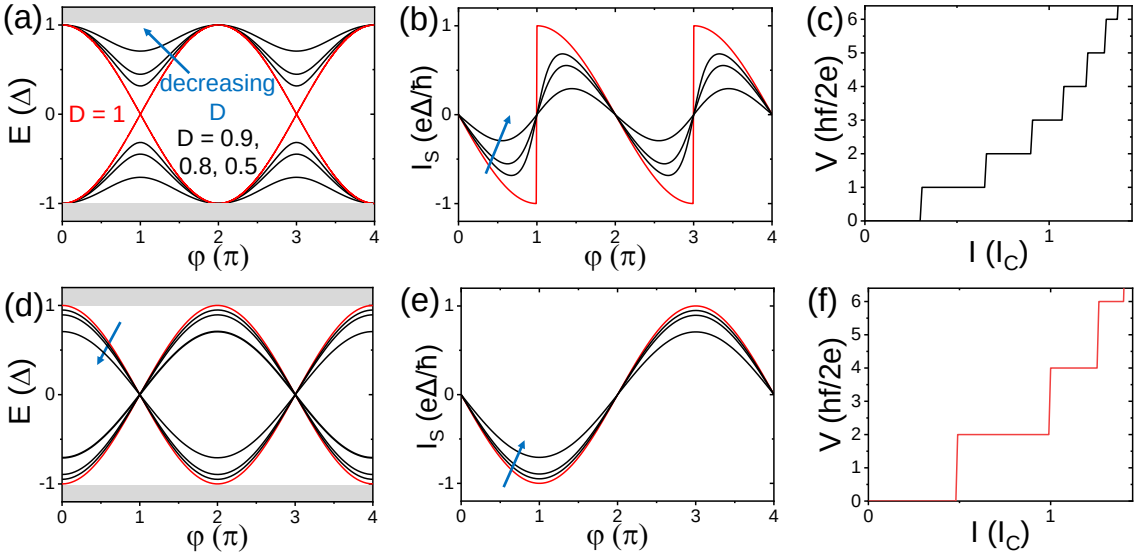

FIG. 2.17: (a) Andreev bound state spectrum assuming an s-wave pairing potential for different values of the transmission D. (b) The resulting current-phase relation for the same values of D. It is 2π-periodic with respect to the phase difference φ. (c) I-V trace in the presence of microwave radiation. All Shapiro steps at V_n are visible when the current-phase relation is 2π-periodic (see section 2.2.5). (d) Andreev bound state spectrum assuming a p-wave pairing potential for the same values of D as in (a). (e) The resulting current-phase relation is 4π-periodic. (f) I-V trace in the presence of microwave radiation. The even steps exclusively emerge for a 4π-periodic current-phase relation. Adapted from [27, 28, 34].

The current carried by a quasiparticle state can be calculated by

$$I_S = \frac{2e}{\hbar}\frac{\partial E(\varphi)}{\partial \varphi}. \tag{2.3.27}$$

Thus, the Josephson current of a single state assuming s-wave pairing is

$$I_S^{s-wave} = \pm\frac{2e\Delta_0 D}{4\hbar\sqrt{1 - D\sin^2(\varphi/2)}}\sin(\varphi). \tag{2.3.28}$$

in the limit of zero temperature. The resulting current-phase relation is plotted in figure 2.17(b). For clarity, only the result for one sign is plotted. In the limit $D \ll 1$, we recover the perfectly sinusoidal relation as it was derived in section 2.2.3 with the Josephson frequency $f_J = 2eV/\hbar$.
The Josephson current assuming p-wave pairing is given by

$$I_S^{p-wave} = \pm\frac{e\Delta_0\sqrt{D}}{\hbar}\sin(\varphi/2). \tag{2.3.29}$$

The resulting 4π-periodic current-phase relation is plotted in figure 2.17(e). If a small voltage $eV \ll \Delta_0$ is applied to the junction, the phase difference acquires a

dependence on time $\varphi(t) = 2eVt/\hbar$, and an occupied state produces the current

$$I_S^{p-wave} = \frac{e\Delta_0\sqrt{D}}{\hbar}\sin(\frac{eVt}{\hbar}). \tag{2.3.30}$$

The frequency of the current $f_{J/2} = eV/\hbar$ is exactly half of the conventional Josephson frequency f_J. The fractional frequency has its origin in the fact that the energy in equation (2.3.26) has the period 4π in φ, rather than the conventional 2π. This has also consequences for the appearance of Shapiro steps. In section 2.2.4 and 2.2.5, we discussed the washboard potential and the emergence of Shapiro steps with respect to a 2π-periodic supercurrent $I_S \sim \sin(\varphi)$ in the presence of microwave radiation. If such a current is replaced by a 4π-periodic supercurrent of the form $I_S \sim \sin(\varphi/2)$, also the washboard potential becomes 4π-periodic. Here, when irradiated with microwaves, a phase particle descends m minima during one period of oscillation, and the resulting phase difference is $\Delta\varphi = 4\pi m$. Thus, the Shapiro steps appear at voltages $V_m = mhf/e$ for $m = 0, 1, 2, ...$ or written alternatively

$$V_n = n\frac{hf}{2e} \text{ for } n = 0, 2, 4, ... \tag{2.3.31}$$

Hence, the Shapiro steps with odd numbers are missing compared to the 2π-periodic case (see equation (2.2.33)). The expected I-V traces of a junction in the presence of microwave radiation are shown in figure 2.17(c, f) for a 2π- and a 4π-periodic supercurrent, respectively. Therefore, the missing of odd steps is an indication for an effective p-wave pairing and a signature of a gapless Majorana bound state.

Finally, we take a look at the temperature dependence of the current-phase relations. In order to get the resulting currents at a finite temperature, one had to sum up over all states and multiply with the Fermi occupation function:

$$I_S(T) = \frac{2e}{\hbar}\sum_{j=\pm}\frac{\partial E_j}{\partial\varphi}f_\alpha \tag{2.3.32}$$

with the Fermi occupation function $f_j = \frac{1}{e^{E_j/k_BT}+1}$. The results are given by

$$I_S^{s-wave}(T) = I_S^{s-wave}(0)\tanh\left(\frac{E_-}{2k_BT}\right) \tag{2.3.33}$$

and

$$I_S^{p-wave}(T) = I_S^{p-wave}(0)\tanh\left(\frac{\Delta_0\sqrt{D}\cos(\varphi/2)}{2k_BT}\right). \tag{2.3.34}$$

2.3.5 Majorana fermions in topological insulator nanowires

As discussed in section 2.3.3, Kitaev introduced the Majorana number $\mathcal{M}$ and formulated criteria for the emergence of topological superconductivity in one dimension.

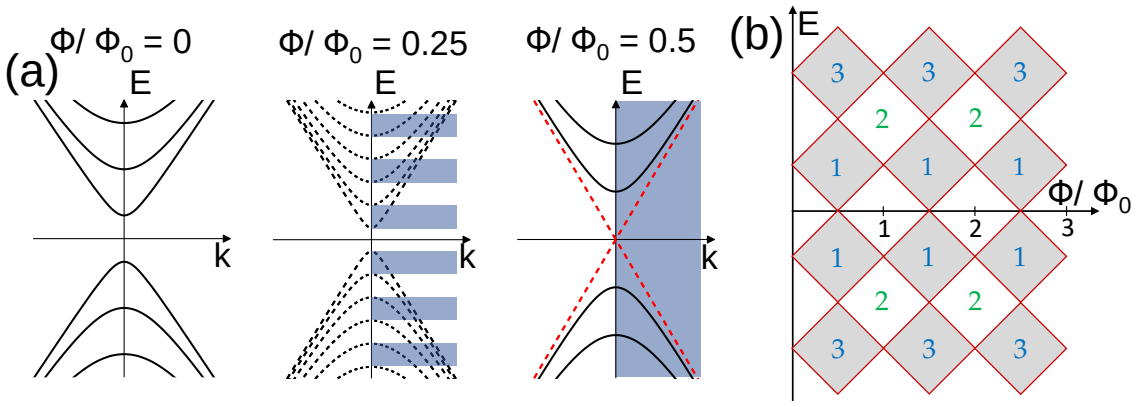

FIG. 2.18: (a) Subband structure of a topological insulator nanowire for three characteristic values of the magnetic flux. Solid lines describe degenerate bands, while dashed lines show nondegenerate states. The blue sections illustrate positions where the number of subbands crossing the Fermi level is odd. (b) Phase diagram of a topological insulator nanowire as a function of energy the E and the magnetic flux Φ. The numbers count subbands crossing the Fermi level. An even number corresponds to a trivial phase, while an odd number labels a topologically nontrivial phase. Adapted from [23].

Consequently, an odd number of Fermi level crossings in the right half of the Brillouin zone of the normal-state band structure is needed. Based on this criterion, Cook and Franz [23, 24] proposed that a nanowire formed of a 3D topological insulator represents a quasi 1D topological superconductor when it is proximitized by an s-wave superconductor. For illustration, we plot again the band structure (see section 2.1.4) of a topological insulator nanowire for three values of the magnetic flux in figure 2.18(a). Degenerate bands with respect to angular momentum are shown as solid lines, while nondegenerate bands are sketched as dashed lines. Since all bands are twofold degenerate for $\Phi/\Phi_0 = 0$, the number of Fermi level crossings in the right half of the Brillouin zone is even for any value of E. Thus, the system is trivial, and $\mathcal{M} = 1$. By increasing the flux, the degeneracy of the bands is lifted. Hence, positions of the energy E emerge where the number of Fermi level crossings in the right half of the Brillouin zone is odd. These are exemplarily shown for $\Phi/\Phi_0 = 0.25$ and marked in blue. For $\Phi/\Phi_0 = 0.5$, the linear, nondegenerate bands evolve while all other bands are again twofold degenerate. Therefore, the number of Fermi level crossings in the right half of the Brillouin zone is odd, and $\mathcal{M} = -1$ for any value of E. Figure 2.18(b) shows the corresponding phase diagram. The numbers count the Fermi level crossings in the right half of the Brillouin zone at the specific values for E and Φ/Φ_0. In the grayish areas, the Majorana number is $\mathcal{M} = -1$, and the system is topologically nontrivial. Thus, it is possible to tune the system from a trivial state at $\Phi/\Phi_0 = 0$ to a topological state at $\Phi/\Phi_0 = 0.5$ by changing the external magnetic field. So far, we only looked at the Majorana number $\mathcal{M}$. The second criterion is that a superconducting gap emerges when the topological insulator nanowire is

proximitized by an s-wave superconductor. Thus, we derive the energy spectrum of proximitized topological insulator nanowires. The system is described by the BdG Hamiltonian (2.2.14) [57, 73]. The Hamiltonian is given by $H \sim \frac{1}{2}\Psi^\dagger \mathcal{H} \Psi$ with

$$\mathcal{H} = \begin{pmatrix} H_{Wire} & \Delta \\ \Delta^* & -\sigma_y H_{Wire}^* \sigma_y \end{pmatrix}. \tag{2.3.35}$$

Here, $H_{Wire} = -i\partial_x \sigma_x + \frac{1}{R}\left(-i\partial_\varphi + \eta\right)\sigma_y - \mu\sigma_0$ as it was derived in section 2.1.4. For the sake of simplicity, we neglect the prefactor 1/2, set $\hbar v_F$ to 1, and define $\eta \coloneqq \Phi/\Phi_0$. Though, we explicitly add the Fermi level μ. The superconducting pairing is given by $\Delta = \sigma_0 \Delta_0 \mathrm{e}^{i n_\nu \varphi}$ with a constant Δ_0. The exponential factor $\mathrm{e}^{i n_\nu \varphi}$ allows the order parameter Δ to wind around the perimeter of the wire. This describes vortices present in the system where n_ν denotes their number. Whether a vortex is present in the system or not, depends on the detailed layout of the sample geometry. If the wire is surrounded by a superconducting shell as it is sketched in figure 2.19(a), the shell likely develops a phase winding at certain values of the magnetic flux, and $n_\nu = 1$. A different situation is shown in figure 2.19(b). The wire lies on top of a flat superconductor. Here, a roughly homogeneous order parameter Δ_0 is expected, i.e. $n_\nu = 0$ [73, 99].

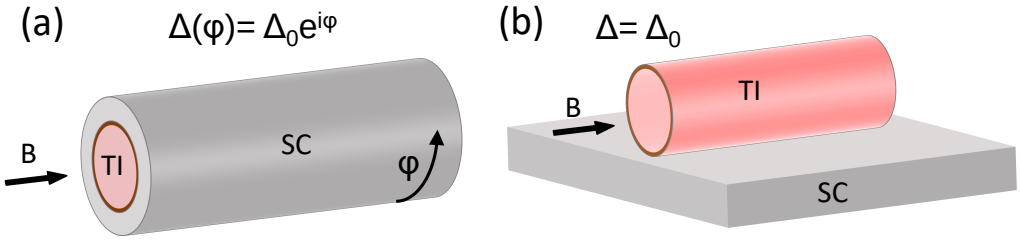

FIG. 2.19: Sketch of a topological insulator nanowire proximitized by an s-wave superconductor. In (a), the wire is surrounded by the superconductor. The superconducting phase winds around the perimeter, and a vortex can be present for certain values of the magnetic flux. In (b), the wire is on top of a superconductor. Here, Δ is homogeneous, and no vortex is present. Adapted from [73].

By substituting H_{Wire} and Δ in equation (2.3.35), the resulting Hamiltonian is given by

$$\mathcal{H} = \begin{pmatrix} -\mu & -i\partial_x - \frac{1}{R}\left(\partial_\varphi + i\eta\right) & \Delta_0 \mathrm{e}^{i n_\nu \varphi} & 0 \\ -i\partial_x + \frac{1}{R}\left(\partial_\varphi + i\eta\right) & -\mu & 0 & \Delta_0 \mathrm{e}^{i n_\nu \varphi} \\ \Delta_0 \mathrm{e}^{-i n_\nu \varphi} & 0 & \mu & i\partial_x + \frac{1}{R}\left(\partial_\varphi - i\eta\right) \\ 0 & \Delta_0 \mathrm{e}^{-i n_\nu \varphi} & i\partial_x - \frac{1}{R}\left(\partial_\varphi - i\eta\right) & \mu \end{pmatrix}.$$

We now introduce the Pauli matrices τ_i in the particle-hole space. Thus, the Hamiltonian can be written in the compact form

$$\mathcal{H} = \left[-i\sigma_x\partial_x + \frac{1}{R}\left(-i\partial_\varphi + \eta\tau_z\right)\sigma_y - \mu\sigma_0\right]\tau_z + \Delta_0\sigma_0\left[\tau_x \cos(n_\nu\varphi) - \tau_y \sin(n_\nu\varphi)\right].$$

The trigonometric terms are removed by the unitary transformation $U = \sigma_0 \mathrm{e}^{i\tau_z n_\nu \varphi/2}$ $= \sigma_0 \left(\tau_0 \cos(\varphi) - \frac{i}{2}\tau_z \sin(\varphi)\right)$ where τ_0 is the unit matrix in particle-hole space. The transformed Hamiltonian $\tilde{\mathcal{H}} = U\mathcal{H}U^\dagger$ reads

$$\tilde{\mathcal{H}} = \left[-i\sigma_x\partial_x + \frac{1}{R}\left(-i\partial_\varphi + \left(\eta - \frac{n_\nu}{2}\right)\tau_z\right)\sigma_y - \mu\sigma_0\right]\tau_z + \Delta_0\sigma_0\tau_x. \tag{2.3.36}$$

However, the transformation also modifies the boundary condition of the transformed wave function $\tilde{\Psi} = U\Psi$ since
$\tilde{\Psi}(\varphi + 2\pi) = U(\varphi + 2\pi)\Psi(\varphi + 2\pi) = U(\varphi)\,\mathrm{e}^{i\tau_z n_\nu \pi}(-\Psi(\varphi)) = -\tilde{\Psi}(\varphi)(-1)^{n_\nu}$. If no vortex is present, i.e. $n_\nu = 0$, the exponential term disappears, and we derive an antiperiodic boundary condition as in section 2.1.4 with $k_\varphi = \pm\frac{1}{2}, \pm\frac{3}{2}, \pm\frac{5}{2}, ...$ When $n_\nu = 1$, the exponential term gives an additional factor of -1, and the boundary condition becomes periodic. Thus, it follows $k_\varphi = 0, \pm1, \pm2, ...$ For the case that half a magnetic flux quantum is applied to the wire ($\eta = 1/2$) and a vortex is present ($n_\nu = 1$), the Hamiltonian simplifies to

$$\tilde{\mathcal{H}} = \left[\hat{k}_x\sigma_x + \frac{1}{R}\hat{k}_\varphi\sigma_y - \mu\sigma_0\right]\tau_z + \Delta_0\sigma_0\tau_x. \tag{2.3.37}$$

The eigenvalues are extracted by squaring the Hamiltonian twice:

$$\tilde{\mathcal{H}}^2 - \left[|\hat{k}_x|^2\mathbb{1}_4 + \frac{1}{R^2}|\hat{k}_\varphi|^2\mathbb{1}_4 + \mu^2\mathbb{1}_4 + \Delta_0^2\mathbb{1}_4\right] = -2\mu\left(\hat{k}_x\sigma_x + \frac{1}{R}\hat{k}_\varphi\sigma_y\right)\tau_0.$$

$$\left[\tilde{\mathcal{H}}^2 - \left[|\hat{k}_x|^2\mathbb{1}_4 + \frac{1}{R^2}|\hat{k}_\varphi|^2\mathbb{1}_4 + \mu^2\mathbb{1}_4 + \Delta_0^2\mathbb{1}_4\right]\right]^2 = 4\mu^2\left(|\hat{k}_x|^2\mathbb{1}_4 + \frac{1}{R^2}|\hat{k}_\varphi|^2\mathbb{1}_4\right).$$

This equation contains only unit matrices. Thus, the eigenvalues can be directly extracted from the equation

$$\left[E^2 - \left[k_x^2 + \frac{1}{R^2}k_\varphi^2 + \mu^2 + \Delta_0^2\right]\right]^2 = 4\mu^2\left(k_x^2 + \frac{1}{R^2}k_\varphi^2\right). \tag{2.3.38}$$

When only the first mode is occupied ($k_\varphi = 0$), the energy spectrum is given by

$$E = \pm\sqrt{k_x^2 + \mu^2 + \Delta_0^2 \pm 2\mu k_x}. \tag{2.3.39}$$

The resulting spectrum for $n_\nu = 1$ and $\eta = 1/2$ is shown in figure 2.20(a) with $R = 1$, $\mu = 0.3$, and $\Delta_0 = 0.15$, while figure 2.20(b) shows the energy spectrum for $n_\nu = 0$. For the latter case, we dispense with a detailed calculation since it is more complicated. Here, the eigenvalues of the Hamiltonian have been derived numerically for $k_\varphi = \pm 1/2$.

When a vortex is present, the resulting spectrum, sketched in figure 2.20(a), is gapped. Hence, both criteria for the emergence of Majorana bound states are fulfilled. On the other hand, the spectrum remains gapless in the absence of a vortex.

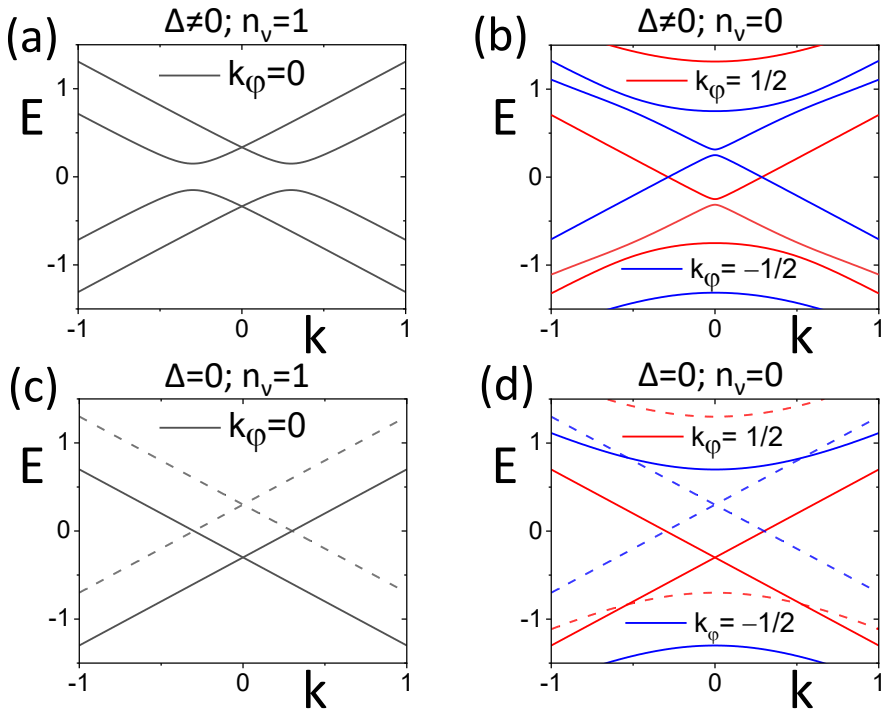

FIG. 2.20: (a) Energy spectrum of a superconducting topological insulator nanowire if only one subband ($k_\varphi = 0$) is occupied, a vortex is present ($n_\nu = 1$), and $\eta = 0.5$ with $R = 1$, $\mu = 0.3$, and $\Delta_0 = 0.15$. The spectrum is gapped. (b) Energy spectrum of a superconducting topological insulator nanowire in the absence of a vortex ($n_\nu = 0$). Here, the lowest subbands are described by $k_\varphi = \pm 1/2$. The other parameters are identical as in (a). The spectrum is gapless. (c-d) The corresponding spectra to (a) and (b) for $\Delta = 0$. Electron-like branches are shown as solid lines, while dashed lines describe the hole-like spectrum. When a vortex is present (c), the linear modes are given by $k_\varphi = 0$. In the absence of a vortex, the linear hole mode has $k_\varphi = -1/2$, while $k_\varphi = +1/2$ holds for the linear electron mode. Adapted from [73].

To give a more demonstrative argument for the differences of both cases, we plot the spectrum in the absence of a pairing potential ($\Delta_0 = 0$) for $n_\nu = 0$ in figure 2.20(d). For $\Delta_0 = 0$ the upper left block and the lower right block of the Hamiltonian (2.3.35) are fully decoupled. The upper left block describes electrons. Their energy was already calculated in section 2.1.4 and gives $E = \pm\sqrt{k_x^2 + (k_\varphi - \eta)^2} - \mu$ for $\hbar v_F = 1$ and $R = 1$. The resulting spectrum is shown by the solid lines in figure 2.20(d). The blue line describes the case $k_\varphi = -1/2$ and the red trace $k_\varphi = +1/2$. The latter presents the linear mode. To get the solution for the lower right block, we derive the energy for holes (time-reversed electrons). This gives $E = \pm\sqrt{k_x^2 + (k_\varphi + \eta)^2} + \mu$. The resulting spectrum is shown by the dashed lines in figure 2.20(d). Again, the blue line describes the case $k_\varphi = -1/2$ and the red trace $k_\varphi = +1/2$. Here, $k_\varphi = -1/2$ leads to the linear branch. Therefore, the electron and the hole branch at $E = 0$

have different angular momenta. If we include superconducting pairing, different angular momentum subblocks of the Hamiltonian cannot be mixed by the pairing potential. Thus, the spectrum cannot be gapped out [73].

The situation is different for $n_\nu = 1$ where $k_\varphi = 0$ if only the first mode is occupied. The energy in the absence of pairing can simply be derived by setting $\Delta_0 = 0$ in equation (2.3.39). It yields $E = \pm k_x \pm \mu$. The spectrum is shown in figure 2.20(c). The linear branches are identical to the case $n_\nu = 0$. However, they are now particle-hole conjugates of $k_\varphi = 0$, and the pairing can gap them out as it is sketched in figure 2.20(a) [73].

This argumentation suggests that it is only possible to observe induced superconductivity in a topological insulator nanowire when a vortex is present. However, de Juan et al. [73] showed that this statement is only true for nanowires with discrete rotational symmetry. If the symmetry is broken, e.g. by disorder, a gap also develops without a vortex even if this one is much smaller than the one obtained with a vortex. Another work by Legg et al. [100] showed that a nonuniform chemical potential across the cross-sectional area of the wire also enables the emergence of Majorana bound states without a vortex. Typically, such a nonuniform distribution is present in the wires used for the experiments [31, 32]. These results are important since they suggest that it is also possible to obtain Majorana bound states in the absence of a vortex. This makes the experiments more feasible since we do not have to clarify the existence of a vortex in the experiment.

3 Experimental methods

This chapter deals with the methods of nanofabrication and the experimental setup. Firstly, the wafer design is reviewed, and the different fabrication techniques are explained. Furthermore, the cryogenic system, i.e. the dilution refrigerator, and the sample holder are presented. After a special focus is placed on the filtering of the measurement lines, the electronic circuit of the measurement setup will be described.

3.1 Wafer material

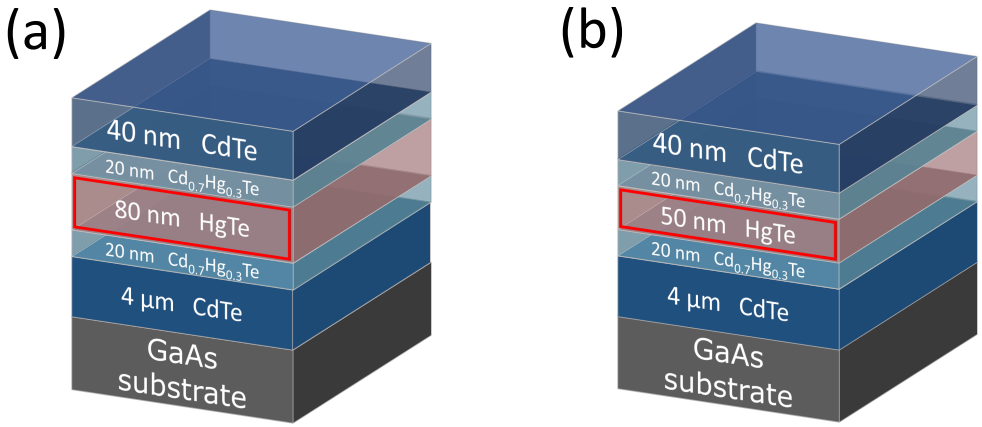

FIG. 3.1: Wafer design of the investigated samples. The 80 nm HgTe film (a) and the 50 nm HgTe film (b) are sandwiched between two $Cd_{0.45}Hg_{0.55}Te$ layers, respectively. The structure is grown on a GaAs substrate and a CdTe layer. Finally, the wafers are capped by CdTe. The surface states are indicated in red. Adapted from [31].

The investigated wafers were grown by molecular beam epitaxy (MBE) at the A. V. Rzhanov Institute of Semiconductor Physics in Novosibirsk. Wafer designs with different thicknesses of the HgTe film were used during this thesis. The structure of a wafer consisting of an 80 nm HgTe layer is illustrated in figure 3.1(a), while the HgTe film in figure 3.1(b) has a thickness of 50 nm. In both cases, the layers are grown on a (013) GaAs and an MBE-grown CdTe substrate. As discussed in section 2.1.3, the HgTe is strained due to the growth on CdTe, and a band gap is opened in

the bulk band structure of HgTe. Additionally, a 20 nm $Cd_{0.7}Hg_{0.3}Te$ buffer layer is introduced between the HgTe and the substrate to reduce dislocations induced by the lattice mismatch. This increases the electron mobility by one order of magnitude [30]. Finally, the wafers are capped by a 20 nm $Cd_{0.7}Hg_{0.3}Te$ and a 40 nm CdTe layer to protect the top interface. Typically for these structures, the Fermi energy is located in the valence band where surface electrons and bulk holes co-exist [30, 31].

Furthermore, wafers with an 80 nm HgTe layer were grown where an Indium doping was added in the $Cd_{0.7}Hg_{0.3}Te$ layers. This leads to a strong n-doping, and the Fermi energy is expected to be in the conduction band.

3.2 Sample fabrication

An essential part of this project was spent on developing and optimizing the fabrication techniques. The fabrication of nanowires requires suitable lithographic processes and etching procedures. However, the biggest task was the deposition of superconducting contacts onto the HgTe nanowire since contacts with high transmissions are an indispensable prerequisite for successful experiments. This section covers the illustration of the different fabrication steps while a special focus lies on the optimization of the deposition of the superconductor. A detailed list of process parameters can be found in appendix A.

3.2.1 Nanowire structuring

The structuring of the nanowire is done by electron beam lithography (EBL). Figure 3.2 illustrates the basic principle of this method. After coating an etch resistant resist on the wafer, it is rotated with high speed using a spin coater. Thus, the resist is spread equally over the whole sample. In the following, the resist is heated up in order to evaporate the solvent which contains the resist. The sample is then placed in a scanning electron microscope (SEM) and irradiated by the computer-controlled electron beam. The area where the nanowire is supposed to be is excluded from the irradiation. The exposed parts of the resist change their chemical structure and become soluble by a developer. A wet chemical etching solution composed of Bromine (Br_2), ethylene glycol ($C_2H_6O_2$), and pure water (H_2O) at a ratio 0.1 : 100 : 25 is used to etch the developed nanowire into the sample. The etching solution is cooled down to 0 °C to enable a slow and controllable etching rate. When the desired etching depth is reached, the sample is taken out of the solution and put into pure water to stop the etching process. Finally, the remaining resist is stripped by a remover. Thus, nanowires with typical widths between 200 nm and 700 nm are fabricated. Due to the proximity effect, i.e. also nearby parts of the irradiated areas get developed

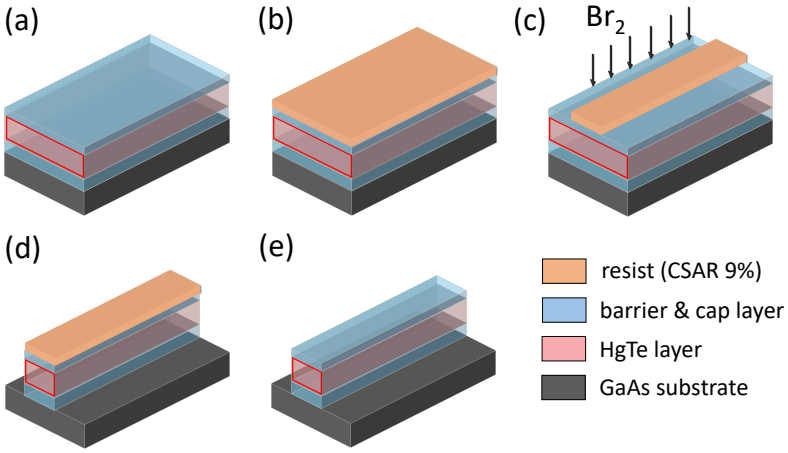

FIG. 3.2: Basic principle of electron beam lithography. (a-b) An etch resistant resist is coated on the wafer. (c) After irradiation by the electron beam, the exposed areas are removed, and the sample is etched using a Br_2 based solution. (d-e) The remaining resist on the etched sample is removed.

during EBL, and the isotropic etching process, where the resist is underetched on a similar scale as the total etching depth, the width of the nanowire has to be chosen approximately 500 nm larger in the computer software than the desired final width. The isotropic etching process also leads to a rounding of the etched structure. This concerns in our case the sidewalls of the nanowire. Hence, we obtain rather a trapezoidal than a perfectly rectangular shape [101].

3.2.2 Removal of the cap layer

Since the superconducting contacts should be directly grown onto the HgTe layer, the cap layer has to be removed in particular areas. This is again achieved by EBL. The steps are visualized in figure 3.3(a-c). The sample is coated with a resist, and stripes crossing the nanowire are developed. These stripes define the positions of the superconducting contacts. The cap layer is removed by wet chemical etching. At this step, it is very important to get a very precise etching depth of 60 nm in order to not remove too much of the HgTe, but to eliminate precisely the entire cap layer. Therefore, we use an etching solution at a ratio $Br_2 : C_2H_6O_2 : H_2O = \sim 0.015 : 100 : 25$ cooled down to 0 °C. Due to the low proportion of Br_2, the etching rate is much slower and more controllable as for the etching of the nanowire. Again, we also have to compensate for the proximity effect and the isotropy of the etching process. The width of the stripes should be chosen approximately $300 - 350$ nm smaller than the desired final width of the contacts. This must also to be taken into account by determining the distance between the contacts. The etched stripes can now be filled with a superconducting material.

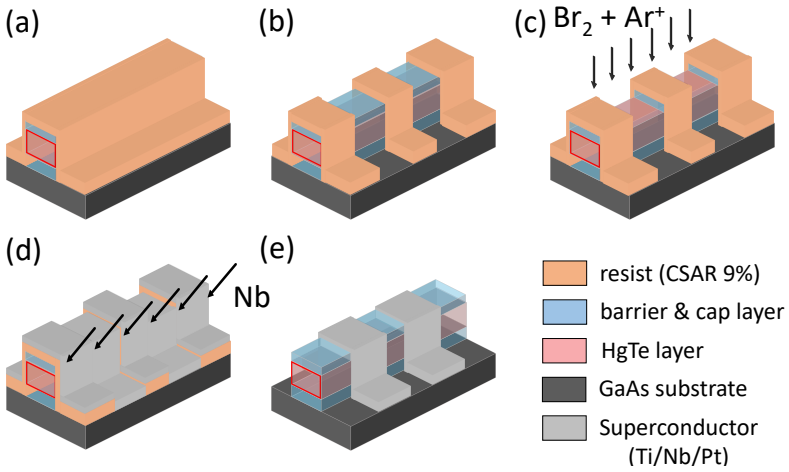

FIG. 3.3: Deposition of the superconductor. (a) The nanowire is coated by a resist. (b) Stripes are developed using EBL. (c) The cap layer is removed by wet chemical etching and a short Ar^+-milling. (d) A thin seed layer of Ti, Nb, and a thin protective layer consisting of Pt are deposited on the sample. (e) The remaining resist with the metal on top is removed in a lift-off process.

Before discussing the deposition of the superconductor, we give a short overview about the problems and solutions during the removal of the cap layer. The goal was to achieve a flat etching profile in order to deposit the superconductor homogeneously onto the HgTe. To analyze the etching profiles and to determine the etching rate, the resist is removed after the wet chemical etching. Hence, the etched stripes could be investigated using an atomic force microscope (AFM). Here, the sample is scanned by a cantilever, and we get a profile of the surface. By etching a single stripe into the material, two different scenarios could be observed. For stripes with widths $W \lesssim 1\,\mu m$, a rounded etching profile is achieved as it is sketched in the lower panel of figure 3.4(a). For widths $W \gtrsim 1\,\mu m$, large trenches are formed at the boundaries as shown in the upper panel of figure 3.4(a). These observations are in agreement with the results of M. Pleyer [102]. For a homogeneous deposition of the superconductor, the first scenario seems preferable. However, by placing two stripes each with $W < 1\,\mu m$ close to each other, we found that the trenches still arise, even if only on the outermost boundaries when the widths of the two stripes plus the distance between them is $> 1\,\mu m$. A 3D AFM image of such a structure is shown in the upper panel of figure 3.4(b). The lower panel shows a line cut along the red dashed line in the 3D image. Here, the trenches at the outer boundaries of the stripes are visible. Thus, the desired flat etching profile cannot be achieved with this simple layout. To overcome this problem, we fabricate structures with four stripes next to each other. Figure 3.4(c) shows the corresponding AFM images. Of course, there are again trenches on the outer stripes, but the etching profile of the two inner stripes is perfectly flat. Therefore, our layout consists of four stripes while only the inner ones represent the junction where the measurements are taken. During the

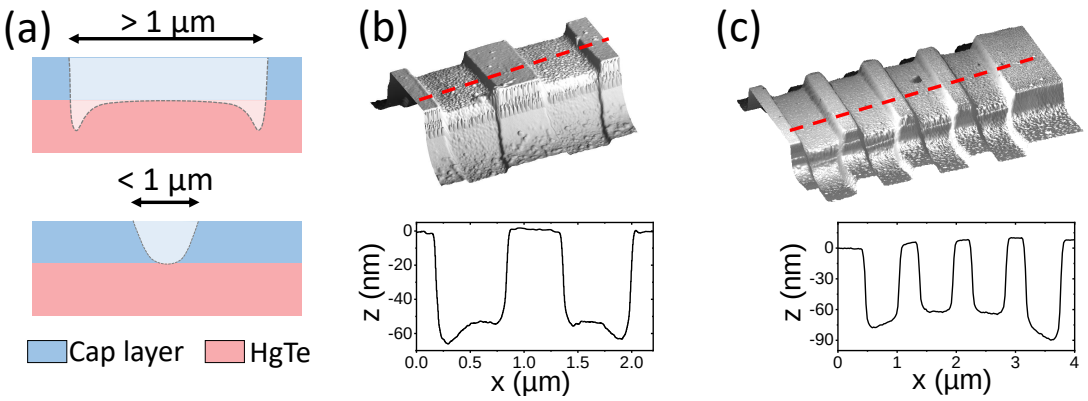

FIG. 3.4: (a) Typical profiles after wet chemical etching. For stripes with widths $W \gtrsim 1\,\mu m$, large trenches are observed at the boundaries, while we observe a rounded profile for $W \lesssim 1\,\mu m$. (b) 3D AFM image of two stripes next to each other (upper panel) where the total width of the structure exceeds $2\,\mu m$. A linecut along the red dashed line is shown in the lower panel. Trenches emerge at the outermost boundaries. (c) 3D AFM image of four stripes next to each other (upper panel) and a linecut (lower panel) along the red dashed line. Despite there are trenches at the outer boundaries, the two inner contacts, which are used for the measurements, are very homogeneous.

analysis of the etching profiles, the etching rates can also be determined. It was found that the rate strongly depends on the exact geometry, i.e. the width of the nanowire and the width of the stripes. Thus, the rate has to be checked each time after changing the geometric parameters.

3.2.3 Contact cleaning and deposition of the superconductor

Once the etching rate for a specific geometry is determined, the superconducting material is deposited into the stripes without removing the resist after etching the cap layer. Figure 3.3(c-e) summarizes the process steps. The deposition is done in an ultra-high vacuum (UHV) chamber. The structure of the chamber is sketched in figure 3.5(a). We use Niobium (Nb) as the superconducting material. From the starting point of depositing only Nb, a few steps were added before and afterwards which all continuously improved the quality of the samples. Fortunately, all of these steps can be done in the same chamber without breaking the vacuum in between. Here, we present the final version of the fabrication process.

Contact cleaning

Since a high quality of the interface between the superconductor and the HgTe is needed, i.e. it should be free from impurities and oxides, the contacts are cleaned by

a short Argon (Ar^+)-milling before the deposition of the superconductor. This is necessary because oxides are continuously formed on the surface when the sample is exposed to air, even at the short time transferring it from the etching lab to the UHV chamber. The contact cleaning is done in the evacuated prechamber using a Kaufman ion source. The right half of figure 3.5(a) illustrates a sketch of the Kaufman source. The sample is placed onto a movable transfer rod and aligned above of the Kaufman source. Ar is admitted to the prechamber, and electrons are emitted from a cathode. A positive voltage V_{dis} is applied to the Kaufman source in order to accelerate the electrons through the Ar atoms. The electrons discharge the atoms, and Ar^+ ions remain. By applying a positive beam voltage V_b at the bottom of the Kaufman source as well as a negative voltage V_{acc} at an acceleration grid on top of the Kaufman source, the Ar^+ ions are accelerated towards the sample. Their kinetic energy is determined by the values of V_{acc} and V_b. The Ar^+ ions dislodge atoms on the surface of the sample. Hence, the surface is effectively etched. To remove at least the oxides on the surface, an etching depth of approximately 3 nm is desirable. A detailed analysis of the etching rates for various parameters can be found in the bachelor's thesis of J. Maier [103].

Thermal evaporation

Subsequently, the sample is transferred to the main chamber without breaking the vacuum via a load lock. Here, it is placed onto a rotable sample holder. It was found that a small seed layer (~ 3 nm) of Titanium (Ti) additionally improves the quality of the interface. Thus, the sample is moved into a horizontal position which is labeled as 'Pos 1' in figure 3.5. Ti is evaporated using an electron gun (e-gun), and the material finally condenses at the cold surface of the sample.

dc sputtering

The Nb is deposited using dc sputtering. Similar to the Kaufman source, Ar is admitted to the main chamber, and the atoms are discharged. They are now accelerated towards the Nb target by applying a negative voltage to the target. The Ar^+ ions dislodge Nb particles from the target. These particles are deposited on the sample. Since the Nb target sits on the slant, we have to adjust the right position of the sample during sputtering. Normally, we would adjust the sample perpendicular to the sputtering direction. However, we tune the sample to 'Pos 2' in figure 3.5(a) where an angle α describes the tilt of the sample with respect to the position perpendicular to the sputtering direction. Hence, Nb is deposited at an angle. This ensures that Nb preferentially covers one sidewall of the nanowire. Thus, a good electrical connection around one edge of the nanowire is guaranteed. Figure 3.5(b) shows a SEM image of a nanowire where Nb was sputtered at an angle

$\alpha \approx 45\,^{\circ}$. One can clearly observe that the right sidewall is preferably covered by Nb. The measurement devices are connected to the nanowire via this side.

As Nb oxidizes exposed to air, we add a thin layer ($\sim 3\,\mathrm{nm}$) of Platinum (Pt) to protect the Nb. The Pt layer is deposited via thermal evaporation analogous to the deposition of Ti. After the deposition, the remaining resist including the materials on top of it is stripped by a remover in an ultrasonic bath. Hence, the materials only remain at the beforehand exposed and developed areas. Finally, metallic contacts consisting of Ti and gold (Au) are fabricated using EBL and thermal evaporation. These contacts are shown in figure 3.5(c). They connect the superconducting leads and form large bond pads in the outer area of the sample (not shown in the figure). The sample is glued into a chip carrier, and a thin gold wire is bonded between the contact pads of the chip carrier and the Ti/Au pads.

For one sample, which is labeled as rI, a topgate is added before gluing the sample into the chip carrier. Here, an insulator consisting of 30 nm SiO_2 grown by plasma enhanced chemical vapor deposition (PECVD) and 100 nm Al_2O_3 grown by atomic layer deposition (ALD) is deposited. Finally, a Ti/Au gate is fabricated by thermal evaporation.

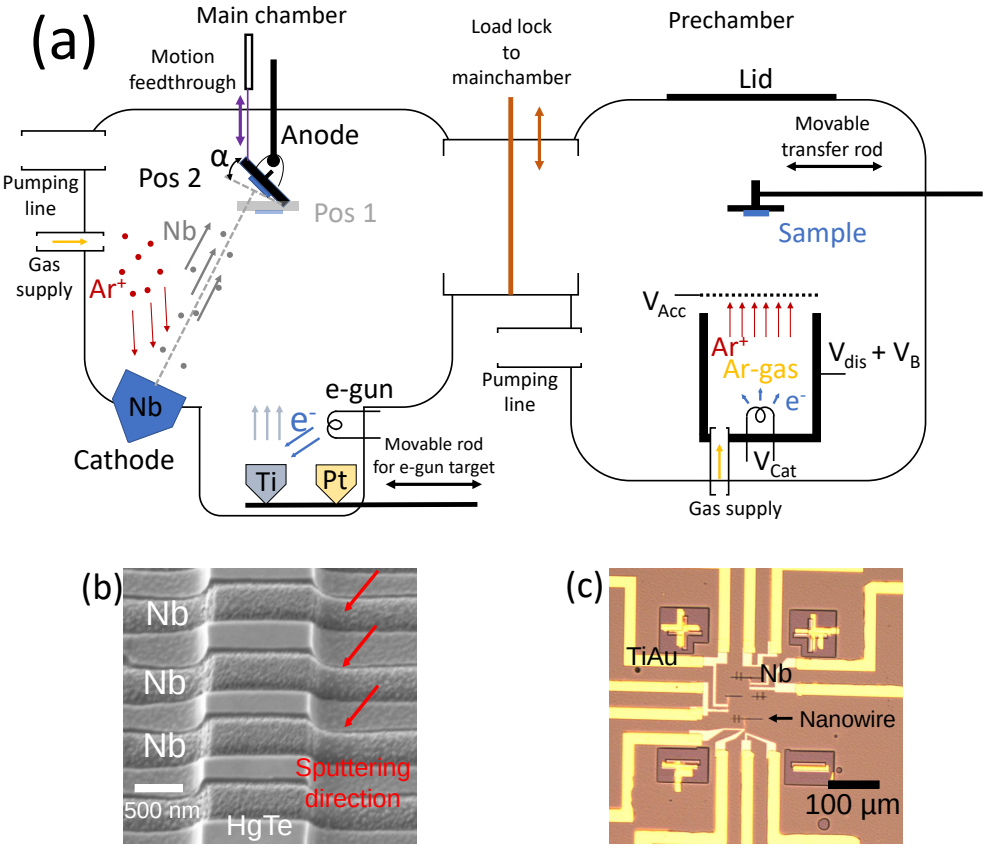

FIG. 3.5: (a) Basic structure of the UHV chamber. The sample is placed into the prechamber (right) via the lid. Here, a Kaufmann ion source enables the etching of the sample. The sample can be directly transferred to the main chamber (left) via a load lock. In the main chamber, Nb is deposited using dc sputtering. Additionally, the deposition of Ti and Pt is possible by thermal evaporation using an e-gun. Between the different deposition methods, the position of the sample has to be changed by a motion feedthrough. (b) SEM image of a nanowire after the deposition of superconducting contacts. Since Nb is deposited under an effective angle, one sidewall of the wire, here the right one, is preferentially covered by the superconductor. (c) Picture of a sample consisting of three junctions taken with an optical microscope. The superconducting contacts look white. The leads to these contacts are made of Ti/Au to enable bonding to a chip carrier.

3.3 Cryostats and sample holder

Most experiments were carried out in a ^{3}He/^{4}He dilution refrigerator. The cooling mechanism is based on the phase separation of ^{3}He/^{4}He mixtures. The binding forces between ^{3}He atoms are smaller due to a stronger zero-point motion than between a ^{3}He atom and a ^{4}He atom. This causes that both isotopes form not well separated phases, even at $T = 0\,K$. Only at a ^{3}He content of 6.4 % in ^{4}He, the binding energies are low enough so that ^{3}He is no longer soluble in ^{4}He. Hence, two phases emerge: A concentrate phase which consists of pure ^{3}He and a dilute phase consisting of $\sim$ 6.4 % ^{3}He and $\sim$ 93.6 % ^{4}He[1]. By continuously removing ^{3}He from the dilute phase, ^{3}He from the concentrate phase enters the dilute phase to keep the most favorable concentration. This phase transition costs energy which is taken from the environment and provides a cooling effect [104].

The following explains how this is technically realized. In this project, an *Oxford Instruments Kelvinox TLM* dilution refrigerator was used. Figure 3.6 sketches the structure of the dilution refrigerator and its working principle. The dilution unit chamber is enclosed by an inner vacuum chamber, followed by a ^{4}He reservoir, a nitrogen shield, and an outer vacuum chamber. The gaseous ^{3}He/^{4}He mixture flows

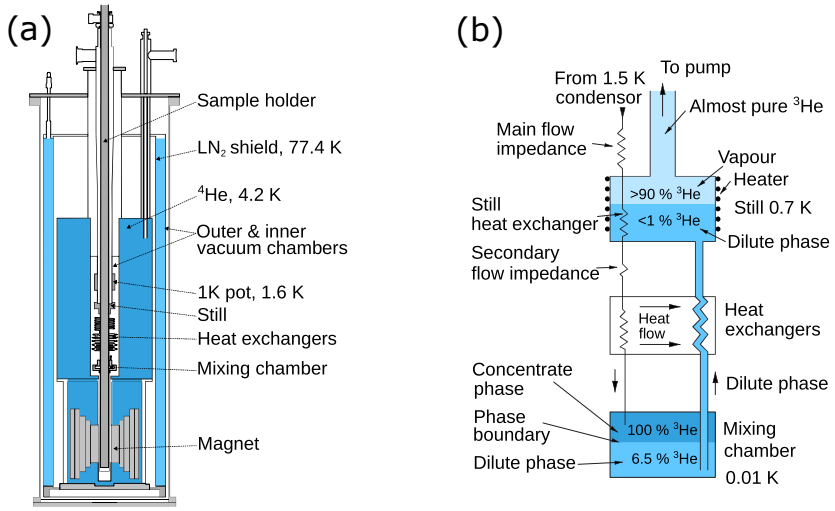

FIG. 3.6: Sketch of a dilution refrigerator. The mixing chamber is enclosed by an inner vacuum chamber, a ^{4}He reservoir, a nitrogen shield, and an outer vacuum chamber. The sample holder can be directly inserted into the mixing chamber. (b) Working principle of a dilution refrigerator. ^{3}He is continuously drawn out of the dilute phase via the still. Thus, ^{3}He from the concentrate phase enters the dilute phase to keep the most favorable concentration. This leads to a cooling effect. Taken from [101].

[1]The exact ratio depends on temperature and pressure.

into the dilution unit, passes the ^{4}He bath and the 1 K-pot where it cools down and liquefies. Below 0.872 K, the mixture separates into the concentrate and the dilute phase. By continuously pumping on the dilute phase via the still, ^{3}He is drawn out of the dilute phase until it evaporates. To keep the energetically most favorable condition, ^{3}He from the concentrate phase enters the dilute phase leading to a cooling effect. With the *Kelvinox TLM* system, temperatures down to 15 mK can be achieved depending on the sample holder. The upper limit for a stable temperature is at 1 K. Experiments at higher temperatures were carried out in a ^{4}He bath cryostat which is not discussed here. Additionally, the *Kelvinox TLM* consists of a superconducting coil inside the ^{4}He bath providing magnetic fields up to 19 T.

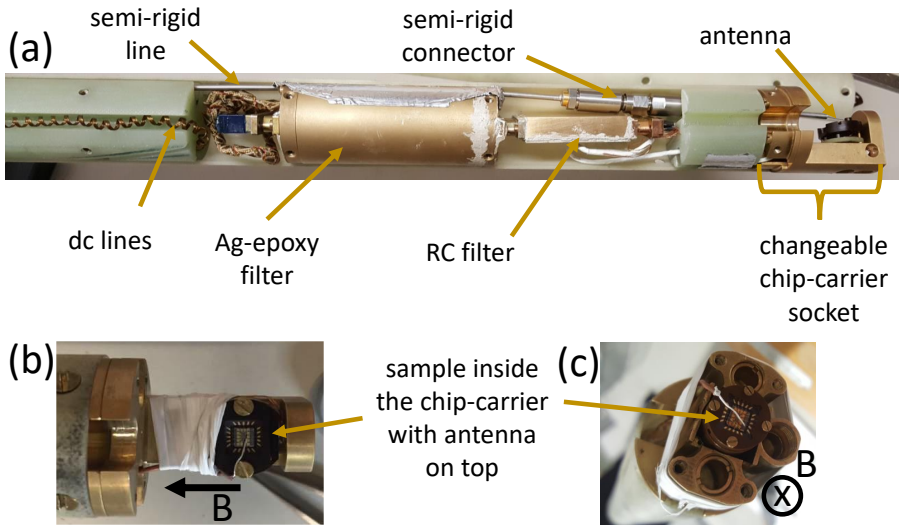

FIG. 3.7: (a) Lowest part of the sample holder. The electric lines are routed towards two filtering stages to the chip carrier socket. An open-ended semi-rigid line acts as an antenna and enables the application of microwave radiation. (b-c) Two different types of the chip carrier socket. The socket in (b) is used for the application of in-plane magnetic fields, while the socket in (c) has to be installed if an out-of-plane field is required.

The special feature of this system is that the sample can be directly introduced into the mixing chamber with the aid of a sample holder. A picture of the lowest part of the sample holder is shown in figure 3.7(a). Electric lines are routed to the sample via the sample holder. The wires are made of manganin to cause a low heat input. Before connecting the sample inside the chip carrier socket, the lines pass two filtering stages which will be discussed in the next section. To apply microwave radiation near the sample, an additional semi-rigid cable is fed into the mixing chamber. The outer conductor of the semi-rigid cable is stripped at the lowest part and acts as an antenna. Since the direction of the external magnetic field is fixed, the orientation of the sample must be changed to study the influence of different directions of magnetic field on the devices. Therefore, two interchangeable chip carrier sockets were used

which are presented in figure 3.7(b-c). They differ in the orientation of the sample to the magnetic field. This enables us to investigate effects considering an in-plane as well as an out-of-plane field with respect to the sample.

3.4 Filtering

In section 2.2.4, we discussed the sensitivity of Josephson junctions to electric noise. The noise has its origin either from electro-magnetic radiation in the environment or from parts of the measurement setup. A big ratio is thermal noise, so-called Johnson-Niquist noise [105, 106]. Here, temporary fluctuations of the current arise due to the thermal motion of charge carriers. Since this effect is suppressed at low (electron) temperatures, a big advance during this thesis was the implementation of low-temperature filters in the electric measurement lines. During the bachelor's thesis of W. Wittl [107], Ag-epoxy filters based on [108] were fabricated. These filters are predicted to have an attenuation $\geq 100\,\mathrm{dB}$ in the frequency range $150\,\mathrm{MHz} - 10\,\mathrm{GHz}$ and $\geq 50\,\mathrm{dB}$ for frequencies $\geq 10\,\mathrm{GHz}$. Furthermore, these properties persist to the low temperatures of the cryostat [108]. Here, we give only a short overview of the fabrication and functionality. A more detailed description is found in [107]. A filter body is cast of Ag-epoxy[2] and subsequently shaped. A picture of the filter body is shown in figure 3.8(a). It contains four segments. A Cu-wire[3] is wound around the body and forms a coil. The winding direction is reversed in adjacent segments to cancel the arising magnetic fields of the coils. During the winding procedure, the wire is steadily covered with Ag-epoxy to fully embed the wire. Figure 3.8(b) shows a finished filter. Additionally, a case was constructed where ten filters could be inserted. A CAD drawing is presented in figure 3.8(c). Filters are placed in each hole of the middle plate. The plate is sealed using Ag-epoxy to separate the two sides of the case. Furthermore, both sides of the case are filled with the silicone rubber material *Eccosorb-CRS-117* which leads to a high attenuation in the microwave frequency range in embedded electric wires [109]. The wires are soldered to micro-D connectors at the cover plates of the case. Finally, all slots on the case are sealed with Ag-epoxy. The filter case can be embedded into the sample holder and is located in the mixing chamber during the measurement. The functionality of the filters is based on the skin-effect [110]: While the current density of a dc current is distributed homogeneously in the cross-sectional area of a conductor, an ac current mainly flows at the surface of the conductor. In particular, the current distribution exponentially drops from the surface to the inner part. This effect is enhanced at higher frequencies. Therefore, the effective area of the conductor is smaller for an ac signal than for a dc current. This leads to an effective higher resistance for an ac current and, thus,

[2] *EPO-TEK E4110.*
[3] *CUL 200/0.1*; 105 windings per segment.

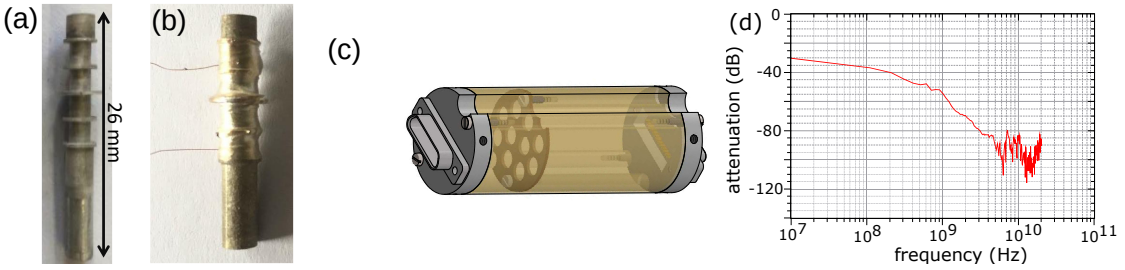

FIG. 3.8: (a) A filter body cast of Ag-epoxy. (b) A single filter after the Cu-wire was wound around, and it was embedded by Ag-epoxy. (c) CAD drawing of the case where ten filters are placed into the holes of the middle plate. After sealing the middle plate with Ag-epoxy and filling the case with *Eccosorb-CRS-117*, the filters are soldered to micro-D connectors at the cover plates. (d) Attenuation of a single filter as a function of the frequency. For frequencies in the GHz-regime, the Ag-epoxy filters show the highest attenuation. The measurement was taken by T. Huber.

a higher attenuation. Consequently, we are able to filter our measurement signals which are mainly dc or low-frequency ac signals and eliminate high-frequency noise. The attenuation curve of a single filter is shown in figure 3.8(d). The curve was taken using a network analyzer where the frequency-dependent attenuation of a reference signal through the filter was detected. The data show an attenuation $> 40\,\mathrm{dB}$ in the GHz-regime and, thus, confirms the functionality of the filters.

Since the enhanced resistance of ac currents causes Joule heating, another important issue is the thermal dissipation. This is the reason why Ag-epoxy was the material of choice. Because of its high electric conductivity[4], it has also a high thermal conductivity due to the Franz-Wiedemann law. Therefore, the emerging heat is rapidly released to the environment.

As the Ag-epoxy filters attenuate frequencies above several hundreds of MHz, additional filters are needed for lower frequencies. Hence, RC low-pass filter were produced. A custom-made circuit board was fabricated where surface mounted devices (SMD) can be soldered onto. A circuit board consists of ten measurement lines in accordance with the Ag-epoxy filters. The board was glued into a case, and the lines were soldered to micro-D plugs. The case is placed directly next to the Ag-epoxy filters. Two different configurations of the RC elements were used while only one of them could be implemented during a temperature cycle due to shortage of space. Figure 3.9(a) shows the two unclosed cases with circuit boards inside. A filtering line of the first board consists of two resistors[5] with $R = 1\,\mathrm{k\Omega}$ and a capacitor[6] with $C = 15\,\mathrm{nF}$. They are orientated in a T-shaped structure as it is sketched in figure 3.9(b). The cutoff frequency is $f = 1/(2\pi RC) \approx 10\,\mathrm{kHz}$. It

[4] $\sigma = 2 \cdot 10^5 \mathrm{S/m}$.
[5] Vishay Dale (Part number: *TNPW08051K00BEEA*).
[6] Murata Electronics (Part number: *GRM2195C1H153JA01D*).

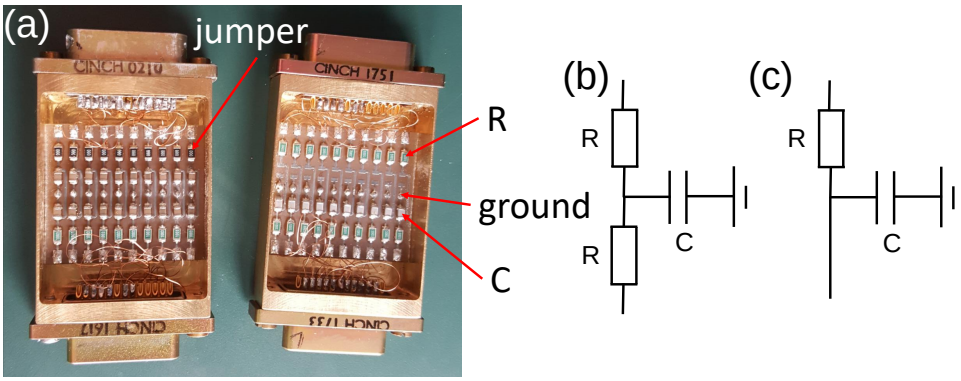

FIG. 3.9: (a) RC low-pass filters on circuit boards inside the unclosed cases. The circuit board in the right case consists of ten measurement lines with a cutoff frequency $f \approx 10\,\mathrm{kHz}$. The electronic parts are ordered in a T-shaped structure as shown in (b). The lines in the left case have a cutoff frequency $f \approx 17\,\mathrm{Hz}$. The electronic parts are ordered in a L-shaped structure as shown in (c). Here, a zero-ohm jumper is used to enable the usage of an unique circuit board structure for both types of filter.

is important to utilize ceramic (NP0) capacitors and thin film resistors since their properties are quite stable while cooling them down to millikelvin temperatures. The second configuration contains one resistor[7] with $R = 100\,\mathrm{k\Omega}$ and a capacitance[8] $C = 94\,\mathrm{nF}$. They are orientated in a L-shaped configuration as sketched in figure 3.9(c). The cutoff frequency is $f \approx 17\,\mathrm{Hz}$. The latter version is the preferable choice in order to reduce effects of noise to the Josephson junctions. However, if three-point measurements are necessary, the first configuration has to be used due to the smaller series resistance while a reduction of noise is still guaranteed.

Finally, commercial π-filters[9] were used at room temperature. They typically have the highest attenuation in the intermediate MHz-regime.

3.5 Measurement setup

The measurement setup including the filters and a sketch of the sample is illustrated in figure 3.10. The two inner superconducting leads on the nanowire are used for the measurements. They are splitted up, respectively, and are connected to four lines of the sample holder. Since the splitting still takes place within the superconductor, four-point probe measurements can be performed as long as the contacts are superconducting.

[7] Vishay Dale (Part number: *TNPW0805100KBEEN*).
[8] The capacitance consists of two 47 nF capacitors (Kemet, Part number: *C0805C473J3GACAUTO*) which are placed in parallel.
[9] *Tusonix 4201-001.*

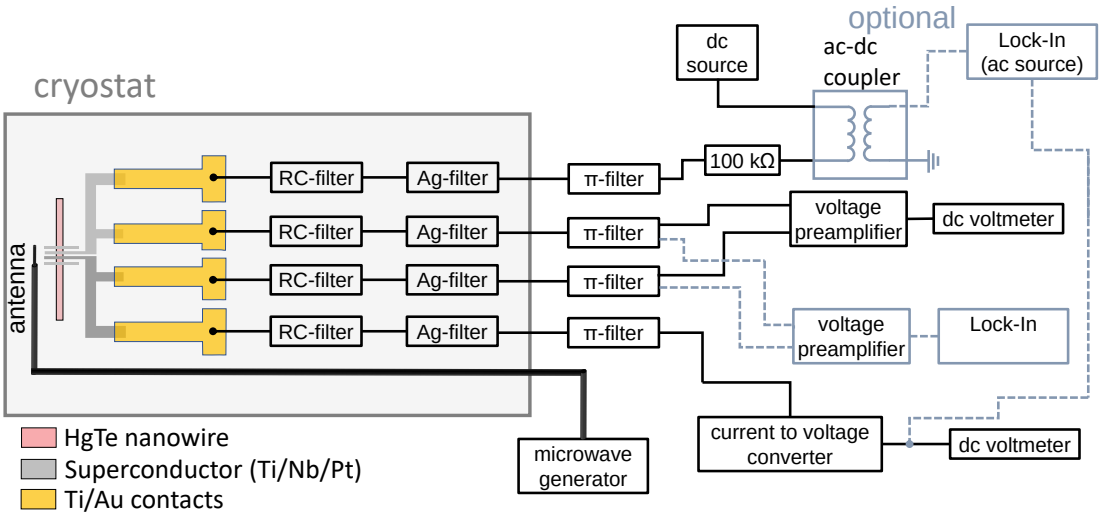

FIG. 3.10: Sketch of the measurement setup. The sample, RC-filters, and the Ag-epoxy filters are placed inside the cryostat. The room temperature setup consists of a pure dc part shown by solid lines. This part is sufficient to measure I_{dc}-V traces. A semi-rigid line enables the application of microwave radiation to the sample. The optional ac part is illustrated by dashed lines. Here, a small ac signal is coupled into the dc line via an ac/dc coupler. This gives us the possibility to directly measure the differential resistance, i.e. the slope of the I_{dc}-V trace.

The external setup can be divided into a pure dc part which is shown by solid lines in figure 3.10 and an optional ac part which enables measurements of the differential resistance. Firstly, we concentrate on the dc part: A dc source (*Yokogawa 7651*) supplies a voltage V_{bias} which is applied over a resistor ($R = 100\,\mathrm{k\Omega}$) and the sample. The resulting current I_{dc} flowing across the sample is determined by a dc voltmeter (*Agilent 34410A*) after it is converted to a voltage signal by a current/voltage converter (*Ithaco 1211 Current Preamplifier*). Since the resistor is chosen to comply with $R \gg R_{sample}$, the current I_{dc} can be changed in equidistant steps with the applied voltage V_{bias}. In this situation, the junction is current-biased.

The voltage drop across the sample V is measured by a dc voltmeter (*Agilent 34420A*). A voltage amplifier (*Femto DLPVA-100-F-D*) is placed in front of the voltmeter to amplify the small voltage signals. Furthermore, it maximizes the input resistance and prevents the sample from noise generated by the voltmeter.

To resolve small changes of the resistance, the setup can be extended to measure the differential resistance dV/dI_{dc}. The extended part is sketched by the dashed lines in figure 3.10. A lock-in amplifier (*Signal Recovery DSP 7265*) generates a small ac signal which is coupled into the dc line using a transformer as an ac/dc coupler. The ac current I_{ac} flowing across the sample is measured by the same lock-in amplifier. The fact that this setup enables the measurement of the differential

resistance can be understood by expanding a voltage signal which arises from a dc current superimposed by a small ac current I_{ac} with frequency ω. It yields

$$V\left(I_{dc} + I_{ac} sin\left(\omega t\right)\right) = V\left(I_{dc}\right) + \frac{dV}{dI_{dc}} I_{ac} \sin\left(\omega t\right) + ... \tag{3.5.1}$$

Hence, we get the differential resistance dV/dI_{dc} by measuring the amplitude of the ac voltage at the frequency ω and dividing it by I_{ac}. In our setup, this is achieved by measuring the voltage drop across the junction with another lock-in amplifier (*Signal Recovery DSP 7265*). Again, a voltage amplifier (*Femto DLPVA-100-F-D*) is used.

To enable the application of microwave radiation, an antenna is placed next to the sample. The antenna is connected to a microwave generator (*Anritsu MG3691A*), which controls the power and frequency of the radiation, via a semi-rigid cable.

The magnetic field at the sample is generated by superconducting coils inside of the cryostat and is adjusted by a magnetic field controller (*Oxford Instruments IPS 180-20*). Typically, the coils show magnetic remanence which depends on the maximum field generated by the coils. Since our devices are sensitive to small magnetic fields, the remanent field has to be reduced before the sample is loaded to the cryostat. This is achieved by a demagnetization procedure: Starting from the maximum generated field, the magnetic field is driven repeatedly from positive to negative values while continuously lowering the amplitude.

A computer-controlled operation of the instruments is realized with the software package *Lab::Measurement* [111].

For the characterization of the samples, which is described in chapter 4, it is also useful to get access to the energetic scales of our devices. This is achieved by applying a specific voltage V to the device since it is related to energy by eV. Here, it is useful to perform voltage-biased measurements where the applied voltage to the sample can be directly controlled. The existing system can easily be modified in this respect by removing the resistor in front of the sample. The voltage output from the dc source is now applied directly to the sample.

4 Material and device characterization

The knowledge about the basic properties of the materials and devices used is important for the later analysis of the experimental results. Thus, we evaluate the transport properties of the HgTe films and the critical parameters of Nb in the first part of this chapter. After that, important parameters of the fabricated Josephson junctions, e.g. the transmissions, are extracted.

4.1 Material characterization

In this section, the transport characteristics of HgTe and HgTe nanowires as well as the critical parameters of the superconducting Nb films are evaluated. The measurements presented in this section were performed in a ^{4}He bath cryostat at $T_{bath} \approx 1.3\,\mathrm{K}$.

HgTe

To determine the properties of the HgTe layers, a Hallbar geometry with length L and width W is fabricated onto a wafer as sketched in figure 4.1(a). The transport measurements are performed with four-point probe methods. A lock-in amplifier is connected to contacts 1 and 4. On the oscillator output of the lock-in amplifier, an ac voltage with a frequency of 13 Hz and an amplitude of 1 V is emitted. By connecting a series resistance of 10 MΩ, a current of $I = 100\,\mathrm{nA}$ flows through the Hallbar. The voltage drops V_{xx} and V_{xy} along the sample are also detected by lock-in amplifiers. Typical traces for $\rho_{xx} = V_{xx}W/IL$ and $\rho_{xy} = V_{xy}/I$ as a function of an out-of-plane magnetic field B are presented in figure 4.1(b-c). The data stem from a sample made of wafer 170713. The Hall curves $\rho_{xy}(B)$ are nonlinear. This is typical for electron-hole systems [112]. The Fermi energy is located in the bulk valence band where surface electrons and bulk holes co-exist. The Drude formalism for two types of carriers is applied to extract the carrier density n and mobility μ. In this case, the

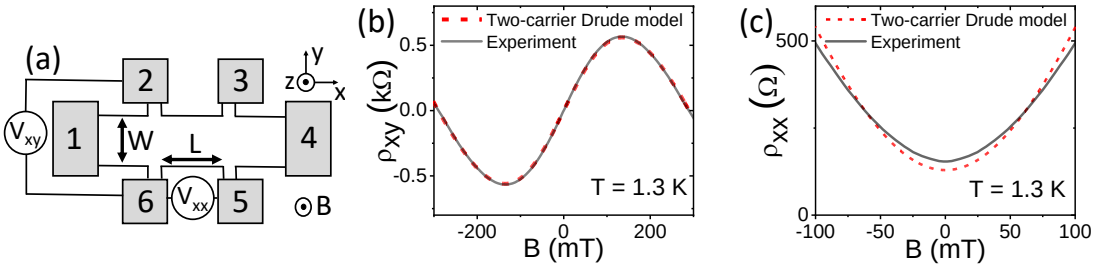

FIG. 4.1: (a) Hallbar geometry for transport experiments. The length between two adjacent contacts is $L = 100\,\mu\text{m}$ while the width of the current path is $W = 50\,\mu\text{m}$. The current I is applied between contacts 1 and 4. The Hall voltage V_{xy} is measured between 2 and 6. The longitudinal voltage V_{xx} is measured between 5 and 6. (b) The Hall resistance $\rho_{xy} = V_{xy}/I$ as a function of the magnetic field B (black curve). The nonlinearity suggests the existence of an electron-hole system. (c) The longitudinal resistance $\rho_{xx} = V_{xx}W/IL$ as a function of the magnetic field B (black curve). A Fit with the two-carrier Drude model, which simultaneously reproduces the traces in (b) and (c), is shown as red dashed lines.

total longitudinal conductance σ_{xx} and Hall conductance σ_{xy} is given by the sum of the conductances of holes σ^h and electrons σ^e:

$$\sigma_{xx} = \sigma^e_{xx} + \sigma^h_{xx}, \qquad \sigma_{xy} = \sigma^e_{xy} + \sigma^h_{xy} \qquad \text{with} \tag{4.1.1}$$

$$\sigma^{e(h)}_{xx} = \frac{q_{e(h)} n_{e(h)} \mu_{e(h)}}{1 + \left(\mu_{e(h)} B\right)^2}, \qquad \sigma^{e(h)}_{xy} = \mu_{e(h)} B \frac{q_{e(h)} n_{e(h)} \mu_{e(h)}}{1 + \left(\mu_{e(h)} B\right)^2}. \tag{4.1.2}$$

Here, $q_{e(h)}$ is the elementary charge of electrons or holes. The expressions for $\rho_{xx}(B)$ and $\rho_{xy}(B)$, which are obtained by tensor inversion of the conductances, can be fitted to the experimental data [30]. The fits are plotted in figure 4.1(b-c) as red dashed lines. The extracted values for different wafers are summarized in table 4.1. Additionally, we calculate the mean free path of the different types of charge carriers $\ell^{mfp}_{e,\,h} = \mu_{e,\,h} \hbar k_F / e$, where $k_F = \sqrt{c\pi n_{e,\,h}}$ with $c = 2$ for bulk carriers or $c = 4$ for surface carriers. For the doped wafers, we only give a span for the mean free path ℓ^{mfp}_e as the Fermi energy is located in the conduction band where surface electrons and bulk electrons co-exist. Here, the two types of charge carriers cannot be distinguished by the two-carrier Drude model. Thus, the extracted mobility is an average value of surface and bulk carriers' mobility. Furthermore, the value of c cannot be unambiguously determined.

In the following section, the extracted parameters are used to determine specific properties of the superconducting devices. However, it is important to note that the values can only be regarded as a rough estimation since the different fabrication process of Hallbar devices and Josephson junctions is expected to produce deviations regarding the individual device parameters.

Wafer	**d** $[nm]$	$\mathbf{n_e}$ $[10^{11}\frac{1}{cm^2}]$	$\mathbf{n_h}$ $[10^{11}\frac{1}{cm^2}]$	$\mu_\mathbf{e}$ $[10^5\frac{cm^2}{Vs}]$	$\mu_\mathbf{h}$ $[10^5\frac{cm^2}{Vs}]$	ℓ_e^{mfp} $[\mu m]$	ℓ_h^{mfp} $[\mu m]$
140826,140827	80	1.0	2.0	2.1	1.4	1.5	1.2
170713	50	0.7	1.9	5.3	0.3	3.2	0.2
190304*	80	63	-	1.0	-	4-6	-
190306*	80	6.5	-	0.4	-	0.5-0.8	-

Table 4.1: Overview of the different wafers where d is the thickness of the HgTe layer, $n_{e(h)}$ is the carrier density of electrons (holes), $\mu_{e(h)}$ is the mobility of electrons (holes), and $\ell_{e(h)}^{mfp}$ is the mean free path of electrons (holes). In the undoped wafers, the Fermi energy is located in the valence band where surface electrons and bulk holes co-exist, while the Fermi energy of the n-doped wafer is shifted into the conduction band. Doped wafers are indicated by an asterisk. The wafers 190304 and 190306 were characterized by J. Ziegler.

HgTe Nanowires

Experiments on nanowires fabricated from HgTe have been performed in earlier works by S. Weishäupl [113] and J. Ziegler [32, 101]. Here, the nanowires showed distinct conductance oscillations which indicate surface-mediated quasiballistic transport. In combination with a theoretical analysis of the observed phenomena, the topological nature of the surface states was confirmed. Furthermore, the phase-coherence lengths of the wires were found to be in the range $2-5\,\mu$m. This gives an upper limit for the circumference of the fabricated wires; below, phase-coherent transport is possible [32].

Niobium

For the fabrication of the superconducting contacts, Niobium (Nb) was the material of choice due to the simplicity in processing. To extract the critical parameters of the Nb films, we fabricated a nanowire with superconducting contacts as described in section 3.2. Though, we short-circuit two of the superconducting leads on top of the wire as shown in the inset of figure 4.2(a). The resistance R of the two shorted leads as a function of an out-of-plane magnetic field B is illustrated in figure 4.2(a). We extract a critical field $B_C \approx 3.5\,\mathrm{T}$ where the superconductivity of Nb breaks down. Figure 4.2(b) shows the resistance R as a function of the temperature T_{bath}. The critical temperature is $T_C \approx 8\,\mathrm{K}$. Deviations from the literature value ($\sim 9.3\,\mathrm{K}$ [114]) arise due to the nonperfect quality of the sputtered Nb film.

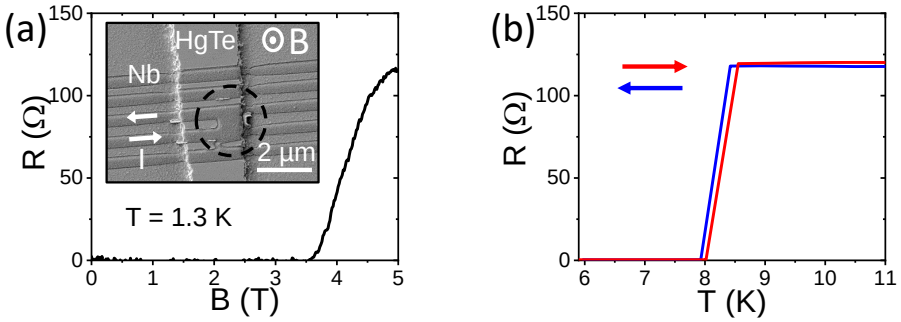

FIG. 4.2: (a) The resistance R of the Nb film as a function of an out-of-plane magnetic field B which is measured among two shorted leads. The critical field is $B_C \approx 3.5\,\mathrm{T}$. The inset shows a SEM image of the device with the shorted leads inside the dashed circle. (b) The resistance R as a function of the temperature T_{bath}. The arrows indicate the respective sweep direction. The critical temperature is $T_C \approx 8\,\mathrm{K}$.

4.2 Properties of the fabricated junctions

In this section, we summarize the properties of the fabricated devices and explain how they are extracted. The results of sample r1, which stems from wafer 140827, are exemplarily shown while table 4.2 contains the data of various devices. The measurements presented in this section were carried out at a temperature of $T_{bath} \approx 40\,\mathrm{mK}$.

The geometric dimensions of the junctions are obtained from the electron micrographs. Figure 4.3(a) shows a SEM image of junction r1. Due to wet-chemical etching, the wires have a trapezoidal cross-sectional area. The top width is $W = 500\,\mathrm{nm}$, the bottom width $W = 580\,\mathrm{nm}$, and the thickness $d = 80\,\mathrm{nm}$ resulting in an effective rectangular cross-sectional area of $A = 80\,\mathrm{nm} \cdot 540\,\mathrm{nm}$. The width can only be determined with some uncertainty which is 12 % for sample r1. The circumference of all wires is shorter than the phase coherence length which is of the order of several microns [32]. Thus, transport within the junction is phase coherent. The distance between adjacent superconducting contacts is $L = 170\,\mathrm{nm}$.

For the topological surface states, this implies a Thouless energy of $E_{Th}^S = \hbar v_F^S / L \approx 1.6\,\mathrm{meV}$ where $v_F^S = \hbar\sqrt{4\pi n_e}/m^* \approx 4.3 \cdot 10^5\,\mathrm{m/s}$ is the Fermi velocity of the surface states with the effective mass $m^* = 0.03\,m_0$ [115] and $n_e = 1.0 \cdot 10^{11}\,1/\mathrm{cm}^2$.

For bulk states, we obtain $E_{Th}^B \approx 0.2\,\mathrm{meV}$ with $v_F^B = \hbar\sqrt{2\pi n_h}/m^* \approx 6.4 \cdot 10^4\,\mathrm{m/s}$ where $m^* = 0.2\,m_0$ and $n_h = 2.0 \cdot 10^{11}\,1/\mathrm{cm}^2$. Here, we used the definition of E_{th} for a clean junction, which requires $L < \ell^{mfp}$. By comparing the length L with the values of sample r1 in table 4.1, we note that this holds for the bulk as well as for the surface carriers.

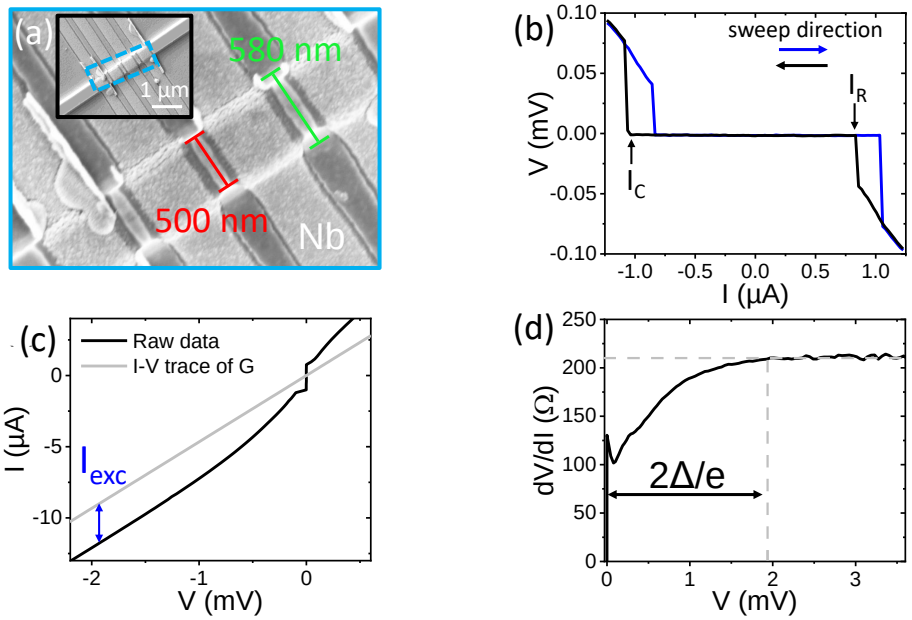

FIG. 4.3: (a) Electron micrograph showing the superconducting Nb stripes placed across the HgTe wire. The wires have a trapezoidal cross-sectional area. In the case of wire r1, the top width is 500 nm and the bottom width 580 nm. For further calculations, we choose the mean value. The inset shows a zoomed out picture. (b) I-V traces of sample r1 at $B = 0$. A distinct hysteresis depending on the sweep direction of the current is observed. (c) I-V curve of sample r1 at $B = 0$. For high bias voltages, the slope represents the normal-state conductance $G = 1/R_N$, while Andreev reflections influence the trace at lower voltages. The presence of an excess current $I_{exc} = 2.75\,\mu\text{A}$ demonstrates the high quality of the interface. (d) The corresponding differential resistance dV/dI plotted as a function of the bias voltage V. An estimation for the superconducting gap of Nb Δ can be extracted from the curve as the trace starts to deviate from the constant normal-state resistance if $eV < 2\Delta$.

Additionally, the number of occupied subbands can be extracted from the geometric parameters of the nanowire. By analyzing equation (2.1.10), we realize that subbands with adjacent angular momentum quantum number ℓ are separated by $\Delta k_l = 1/R$ at $\Phi = 0$. Since we do not have a cylindrical wire, we rewrite $\Delta k_l = 2\pi/P$ with the perimeter P of the wire. With the Fermi wave vector $k_F = \sqrt{4\pi n_e}$ of the surface states, the number of occupied subbands is estimated as $N_e = k_F/\Delta k_l$. Assuming the surface states are located 5 nm below the HgTe surface, the number of occupied subbands is $N_e \approx 20$.

An I-V trace of sample r1 is shown in figure 4.3(b). The critical current is $I_C \approx 1\,\mu\text{A}$ while the retrapping current is $I_R \approx 0.8\,\mu\text{A}$. The hysteresis could stem from capacitive effects as discussed in section 2.2.4. Another possible origin of the hysteresis is Joule heating. Here, the hysteresis is explained as follows: When the junction is in the superconducting regime ($V = 0$), and the bias is increased, the junction switches

to the resistive branch at I_C. If the junction is in the resistive regime ($V \neq 0$), the effective temperature is higher due to the additional resistive heat. Accordingly, the junction becomes superconducting at a lower value I_R when the bias is decreased again [116, 117]. Both potential options will be discussed in section 6.2.

Voltage-biased measurements of sample r1 are presented in figure 4.3 (c-d). The V-I trace is plotted in (c). The differential resistance dV/dI, which presents the derivative of the V-I trace, is shown in (d). The differential resistance, i.e. the slope of the V-I trace, stays constant and represents the normal-state resistance $R_N = 1/G = 214\,\Omega$ for bias voltages $V > 1.9\,\mathrm{mV}$, while for lower voltages Andreev reflections modify the slope [66, 75, 118]. The situation is visualized in figure 4.4. If the voltage across the junction is $V > 2\Delta/e$ (a), charges can flow between the superconductors and the normal conductor. However, electrons cannot be transferred from the normal conductor to the superconductor when $V < 2\Delta/e$ (b). Though, Andreev reflections are possible which modify the conductance of the junction. Hence, the change of the conductance gives an estimation for the superconducting gap of Nb $\Delta = eV/2 \approx 0.95\,\mathrm{meV}$. The additional current flowing across the junction caused by the Andreev reflections is called excess current I_{exc}. It is extracted from the high voltage regime in figure 4.4(c) by comparing the experimental trace with the linear V-I trace defined by the normal-state conductance G. Thus, we obtain $I_{exc} = 2.75\,\mu\mathrm{A}$ for sample r1.

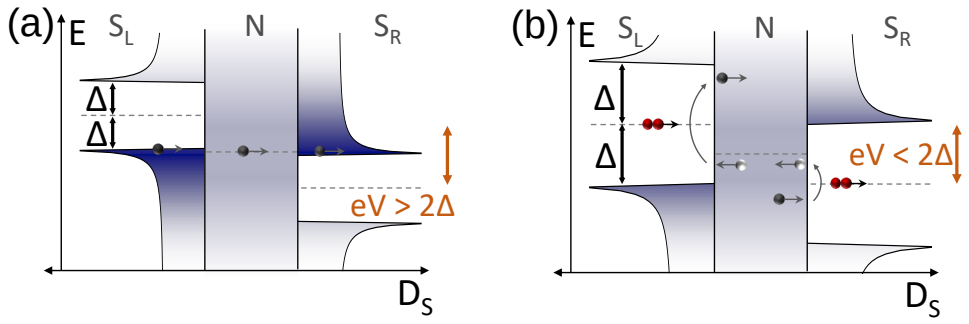

FIG. 4.4: (a) Schematic picture of an S_LNS_R interface for a voltage drop across the junction $V > 2\Delta/e$. Charges can directly flow between the left and right superconducting electrodes. (b) Schematic picture of twofold Andreev reflections. An incoming electron is Andreev-reflected on the right NS interface. The resulting hole is Andreev-reflected on the left NS interface while the created electron can be directly transmitted to the right superconductor. Thus, the amount of charges flowing from the left to the right electrode is increased compared to the situation shown in (a). This process takes place if $V < 2\Delta/e$ and leads to an increased conductance.

With the extracted values, we estimate the average transmission D of the SN interfaces. We show two different approaches: The first one is given by Flensberg et al. [119] which is based on the OBTK theory [118]. By calculating $eI_{exc}R_N/\Delta$, we

extract the parameter Z, which is related to the transmission D by $D = 1/(1+Z^2)$, by using an analytical expression[1] calculated by Niebler et al. [120]:

$$\frac{eI_{exc}R_N}{\Delta} = 2\left(1+2Z^2\right)\frac{\tanh^{-1}\left[2Z\sqrt{(1+Z^2)/(1+6Z^2+4Z^4)}\right]}{Z\sqrt{(1+Z^2)(1+6Z^2+4Z^4)}} - \frac{4}{3}. \quad (4.2.1)$$

By inserting the values of sample r1 and solving for Z, we get $Z \approx 0.8$, and $D_{OBTK} \approx 0.61$. A weak point of this model is the fact that it treats a SNS junction as two NS contacts in series. This neglects the possibility of a quasiparticle interfering with itself which is only valid in the absence of normal reflection, i.e. with perfect transmission [121].

Therefore, we also use the theory for ballistic point contacts [121–123] where the relation between the excess current and the transmission is given by [121]

$$\frac{1}{2}\frac{I_{exc}}{\Delta_i}\frac{h}{Ne^2} = \frac{D^2}{1-D}\left[1 - \frac{D^2}{2(2-D)\sqrt{1-D}}\ln\left(\frac{1+\sqrt{1-D}}{1-\sqrt{1-D}}\right)\right] \quad (4.2.2)$$

with the induced gap Δ_i and the number of contributing channels N. An upper limit for the induced gap is $\Delta_i^{max} \leq \Delta = 0.95\,\text{meV}$. Assuming perfect transmission $D = 1$ of our junctions, we use the relation $I_{exc} = 8\Delta_i/3eR_N$ [121–123] to derive a lower limit $\Delta_i^{min} \geq 0.22\,\text{meV}$. Below, we use the average value $\Delta_i \approx 0.59\,\text{meV}$ of the two limits as a measure of the induced gap. The number of participating channels is estimated from the normal-state resistance R_N using

$$R_N = \frac{1}{G} = \frac{h}{N \cdot D \cdot 2e^2}. \quad (4.2.3)$$

Solving the system of equations (4.2.2) and (4.2.3) with the values of sample r1, we obtain $N \approx 103$ and $D_{BPC} \approx 0.58$. Although this theory describes the physical processes better, there is the problem that the induced gap can only be determined with some inaccuracy. Since both theories provide similar values despite different weaknesses, they seem to be acceptable at least for a rough estimation of the transmission. Table 4.2 summarizes the parameters of several devices fabricated during this thesis.

As some of the theoretical descriptions, shown in chapter 2.3, are only valid for short junctions, we prove if this holds for our devices, especially for the topological surface states. In general, junctions are in the short-junction limit when the induced gap is smaller than the Thouless energy $\Delta_i < E_{th}$. For the surface states, $E_{Th}^S \approx 1.6\,\text{meV}$. This value is even larger than the upper limit of $\Delta_i^{max} \leq 0.95\,\text{meV}$. Thus, we conclude that the short-junction limit holds for the surface states. The situation is different for bulk hole states. Here, $E_{Th}^S \approx 0.2\,\text{meV}$ is smaller than the induced gap $\Delta_i = 0.59\,\text{meV}$. Hence, the device is in the long-junction limit for bulk holes.

[1] In reference [119], the relation between I_{ecx} and Z was determined numerically. Hence, only a graphical evaluation would be possible which might be less precise.

Sample (Wafer)	**W** [nm]	**L** [nm]	**d** [nm]	$\mathbf{I_C}$ [nA]	$\mathbf{R_N}$ [Ω]	$\mathbf{I_{exc}}$ [nA]	$\mathbf{\Delta_i}$ [meV]	**N** (N_S)	$\mathbf{D_{BPC}}$	$\mathbf{D_{OBTK}}$
r1 (140827)	520	170	80	1020	214	2750	0.59	103 (20)	0.58	0.61
r2 (170713)	250	170	50	180	1200	580	0.65	17 (8)	0.61	0.62
r3 (170713)	470	160	50	265	724	694	0.52	31 (14)	0.57	0.60
rD (190306*)	600	180	80	650	331	1800	0.54	70	0.60	0.63
rG (190304*)	700	110	80	600	130	2200	0.50	860	0.23	0.51
rI (140826)	520	240	80	137	614	158	0.52	131 (20)	0.16	0.43

Table 4.2: Overview of different samples where W is the width, L is the length of the junction, and d is the thickness of the HgTe layer. I_C is the critical current of the junction. The transmission D_{OTBK} is estimated from the values of normal-state resistance R_N and the excess current I_{exc} following [119]. Within a different model, D_{BPC} is determined from the number of channels N, the excess current I_{exc}, and the average value of the induced gap Δ_i following [121]. Additionally, the wafer, from which the respective sample stems, and the number of surface channels N_S are listed.

5 Topolgical insulator nanowire junctions in a magnetic field

This chapter describes the study of HgTe wire based Josephson junctions in a magnetic field at millikelvin temperatures ($T_{bath} \approx 40\,\mathrm{mK}$). In the first part, the evolution of the critical current is investigated as a function of an out-of-plane magnetic field.

For a magnetic field aligned parallel to the HgTe wire, we find oscillations of the critical current which are $h/4e$- and even $h/8e$-periodic. These findings are discussed both experimentally and theoretically in the second part of the chapter.

Finally, we deal with resistance oscillations as a function of an axial magnetic field with unusual period of $h/3e$ which appear in the transition from the superconducting to the normal state.

5.1 Evolution of the critical current in an out-of-plane magnetic field

For the first experiments presented, the magnetic field is orientated perpendicular to the sample plane as it is sketched in figure 5.1(a). The observation of the Fraunhofer pattern, as discussed in section 2.2.6, is expected in this configuration.

Exemplarily, we show data of junction r1 which has a width of $W = 520\,\mathrm{nm}$ and a length of $L = 170\,\mathrm{nm}$. Moreover, it has one of the highest transmissions $D_{OBTK} = 0.61$ among the samples studied. With the geometric values, we estimate the magnetic field corresponding to one superconducting flux quantum $\Phi_S = h/2e$: $B_\Phi = \Phi_S/(L + 2\lambda_L)W = 16\,\mathrm{mT}$. Here, we use the London penetration depth of Nb $\lambda_L = 39\,\mathrm{nm}$ [124]. Figure 5.1(c) shows a color map of the differential resistance dV/dI as a function of the applied magnetic field B and the current I. Dark blue regions correspond to superconducting states. The critical current I_C oscillates as a function of B resembling a Fraunhofer pattern where the first minima appear at $+6.8\,\mathrm{mT}$ and $-4.8\,\mathrm{mT}$, respectively. This is in contradiction to the theoretical expectations where the minima should appear at $\pm B_\Phi$. A possible explanation could be a larger λ_L caused by a nonperfect quality of the sputtered Nb film. However,

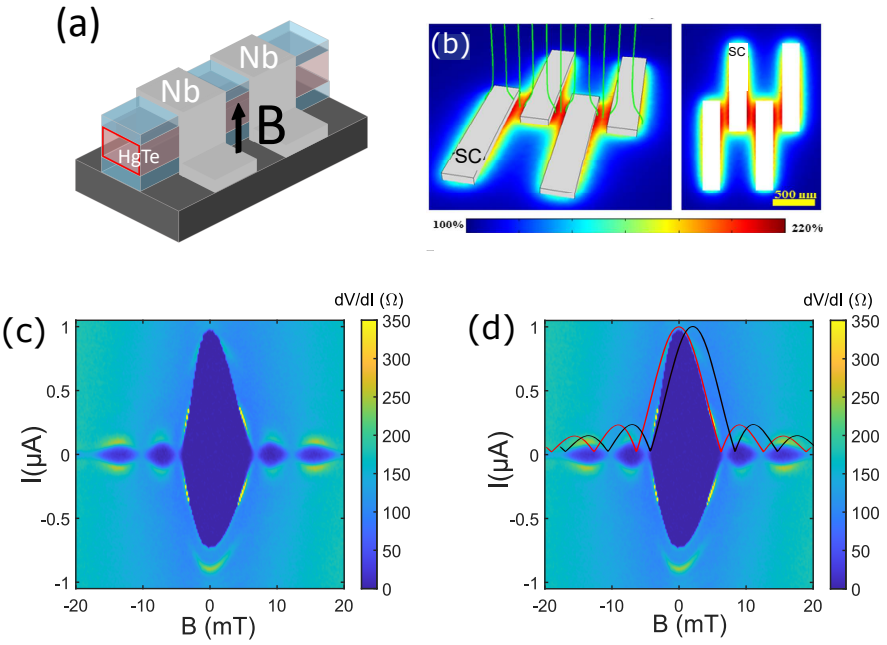

FIG. 5.1: (a) Sketch of the experimental setup. The magnetic field is orientated perpendicular to the sample plane. (b) COMSOL simulation describing the effect of magnetic flux focusing on Josephson junctions. The applied magnetic field B is expelled by the superconducting leads. Thus, the effective field B_{eff} between the contacts is enhanced by a factor C. The local strength of B_{eff} is illustrated by different colors. Blue corresponds to $B_{eff} = B$, while red resembles $B_{eff} = 2.2\,B$. Taken from [125]. (c) Color map of the differential resistance dV/dI as a function of the applied magnetic field B and the current I for sample r1. Dark blue regions correspond to superconducting states. The critical current I_C oscillates as a function of B resembling the Fraunhofer pattern. (d) Fit of the Fraunhofer pattern to the data shown in (c) where a factor $C = 2.4$ is included due to magnetic flux focusing. The red curve perfectly fits the $I_C(B)$-oscillations for positive B while the black curve fits the data for negative B. Both curves show the same fit, but shifted by ΔB to each other.

the values for $2\lambda_L$ would have to be comparable to the width of the superconductor ($\sim 550\,\text{nm}$) in order to obtain the experimentally observed values for the minima. Thus, this argument does not explain the discrepancy, at least not in its entirety.

Another approach, which can explain the discrepancy, is magnetic flux focusing [125]. The applied magnetic field B is expelled by the superconducting contacts. As a result, the magnetic field lines run past the superconductor, and an accumulation of field lines exists between the leads. Therefore, the effective magnetic field B_{eff} between the contacts is higher than the applied field B. We define the constant $C = B_{eff}/B$ as a measure of the strength of magnetic flux focusing. Figure 5.1(c) shows an

illustration of magnetic flux focusing which is based on a COMSOL[1] simulation performed in [125]. By implementing C into equation (2.2.41), the dependence of the critical current I_C is given by

$$I_C(\Phi) = I_C(0)\left|\frac{\sin(C\pi\Phi/\Phi_S)}{C\pi\Phi/\Phi_S}\right|. \tag{5.1.1}$$

In figure 5.1(d), we plot equation (5.1.1) for $C = 2.4$ above the data shown in (c). The red and black curves are identical except for the fact that they are shifted by a value ΔB relative to each other. The red curve perfectly fits the periodicity for positive B while the black curve fits the data for negative B. The shift of the two curves, i.e. the asymmetry of the main peak, is independent of the sweep direction. This asymmetry could be a consequence of the strong spin-orbit interaction occurring in HgTe. Without the asymmetry, magnetic flux focusing explains the experimental data very well. However, it should be mentioned that the determined value for C is probably somewhat smaller since a slightly increased value of λ_L is additionally possible.

Most devices with high transmission and sufficient width show the behavior just described. Now, we also show how samples with poor transmission or very thin wires behave in an out-of-plane magnetic field. Figure 5.2(a) shows a color map of the differential resistance dV/dI as a function of the applied magnetic field B and the current I for sample rG. This junction has a width of $W = 700\,\mathrm{nm}$ and a length of $L = 110\,\mathrm{nm}$ while it has one of the lowest transmissions $D_{OBTK} = 0.51$. This sample does not show $I_C(B)$-oscillations if at all barely visible additional side maxima are present. The position at which the critical current disappears does also not fit the expected theoretical value for the first minimum of the Fraunhofer pattern, even if one assumes a very large magnetic focusing constant $C = 3.1$. The expected Fraunhofer pattern for $C = 3.1$ is indicated by the white trace in figure 5.2(a). The collapse of the superconductivity before the expected minimum can be explained by an inhomogeneous current distribution along the junction. With the low average transmission, many modes hardly contribute to the supercurrent while there are probably also a few individual ones with somewhat higher transmissions. These are localized at certain areas on the junction, i.e. the transmission is somewhat increased at certain points along the width of the wire. The arising $I_C(B)$-pattern is connected to the current distribution along the width by a Fourier transformation. Thus, the pattern experimentally observed can be explained by a specific current distribution in the junction.

Figure 5.2(b) presents a color map of the differential resistance dV/dI as a function of the applied magnetic field B and the current I for sample r2. This junction has a comparable transmission $D_{OBTK} = 0.62$ and length $L = 170\,\mathrm{nm}$ as sample r1. However, sample r2 consists of a very thin nanowire with a width of $W = 250\,\mathrm{nm}$.

[1]COMSOL Multiphysics is a software for simulations of physical processes.

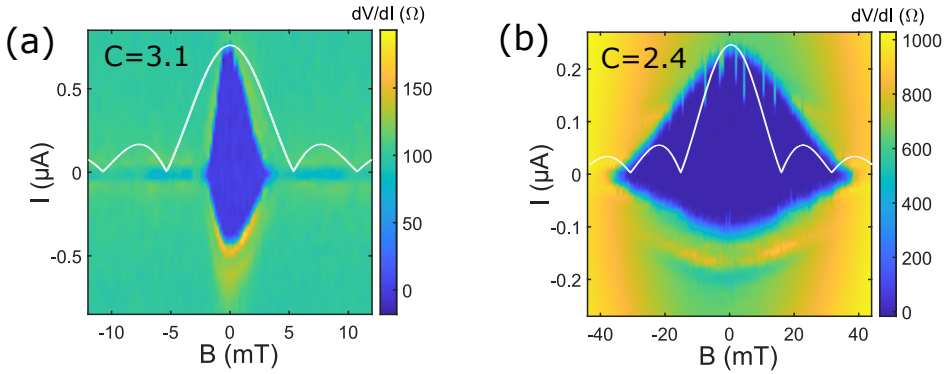

FIG. 5.2: (a) Color map of the differential resistance dV/dI as a function of the applied magnetic field B and the current I for sample rG. The white line shows the expected Fraunhofer pattern for $C = 3.1$. Very small, if any, side maxima are observed due to an inhomogeneous current distribution along the junction. (b) Color map of the differential resistance dV/dI as a function of the applied magnetic field B and the current I for sample r2. The white line shows the expected Fraunhofer pattern for $C = 2.4$. Instead of showing a pattern, I_C monotonously decays since the width of the wire W is smaller than the magnetic length $\epsilon_B = \sqrt{\Phi_S/B}$.

The white trace in figure 5.2(b) illustrates the expected Fraunhofer pattern for $C = 2.4$. In contrast to that, the experimental data show a monotonic decay of I_C by increasing B. Similar observations were found for junctions with a small width in other works [126, 127]. Cuevas et al. [128] theoretically explained the absence of a pattern in very thin wires by the fact that the width W of the junction is smaller than the magnetic length $\epsilon_B = \sqrt{\Phi_S/B}$. In this scenario, pair-breaking effects reduce the induced gap until I_C is fully suppressed. To check if this argumentation holds for our device, we calculate the magnetic length at the position $B_\Phi = 33\,\mathrm{mT}$ where the first minimum of the regular Fraunhofer pattern is expected:

$$\epsilon_B = \sqrt{\frac{\Phi_S}{B_\Phi}} \approx 250\,\mathrm{nm}. \tag{5.1.2}$$

As this value is comparable to the width W, the absence of a magnetic interference pattern can be ascribed to the small width of the junction.

5.2 Critical current oscillations in an axial magnetic field

A magnetic field applied parallel to the current direction in a Josephson junction as it is sketched in figure 5.3(a) is expected to act as a Cooper pair-breaking mechanism

[84–87]. In this scenario, the critical current of the device decreases monotonously with increasing magnetic field strength. For some of our devices, however, we find a strong modulation of the critical current I_C as a function of the axial magnetic field B. Oscillations of the critical current arise which are $h/4e$- and even $h/8e$-periodic. Thus, they constitute a highly unusual interference pattern. In this section, we relate these findings both experimentally and theoretically to the coupling of the superconducting contacts to the topological insulator nanowire junction.

5.2.1 Experimental results

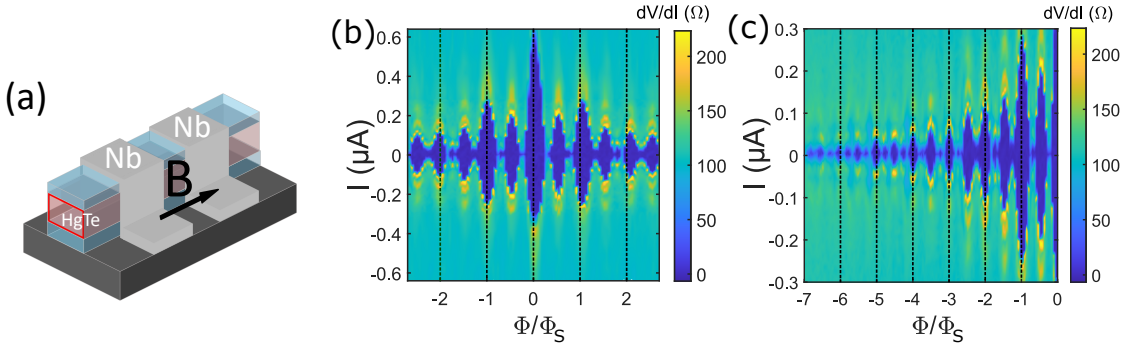

FIG. 5.3: (a) Sketch of the experimental setup. The magnetic field B is orientated along the nanowire. (b) Color map of the differential resistance dV/dI of sample rG as a function of the current I and the magnetic flux Φ/Φ_S. For sample rG, Φ/Φ_S corresponds to $B \approx 36\,\mathrm{mT}$. Superconducting regions are shown in blue. The critical current oscillates with a period of $\Phi_S/2 = h/4e$ while the side maxima at $\Phi = \pm\Phi_S$ are most pronounced. (c) Color map of the differential resistance dV/dI of sample rG up to higher values of the magnetic flux. For $|\Phi/\Phi_S| > 3$, additional maxima appear resulting in a period of $h/8e$.

Figure 5.3(b) presents a color map of the differential resistance dV/dI for sample rG as a function of the current I and the magnetic flux Φ threading the cross-sectional area of the nanowire. This device has a critical current $I_C \approx 600\,\mathrm{nA}$ and shows the most prominent oscillations of I_C among the samples studied. With the width of the wire $W \approx 700\,\mathrm{nm}$, one superconducting flux quantum $\Phi_S = h/2e$ corresponds to $B \approx 36\,\mathrm{mT}$. Blue regions in the color map illustrate superconducting states. The pattern displays maxima of I_C for $\Phi = j \cdot \Phi_S/2$ with j an integer, while I_C is fully suppressed in between them. Furthermore, the maxima at $\pm\Phi_S$ are more pronounced than the $\pm\Phi_S/2$ maxima. Data of the same device up to higher fluxes are shown in figure 5.3(c). Here, additional maxima appear in between the $j \cdot \Phi_S/2$ maxima. Hence, the $h/4e$ periodicity is changed to a $h/8e$ one for higher magnetic fields. The envelope of this pattern can be ascribed to the expected pair-breaking mechanism. We note at this point that roughly $h/2e$-periodic oscillations were observed by Stampfer et al. and ascribed to oscillations of the transmission due to

the conventional Aharonov-Bohm effect [129]. Nonmonotonic behavior of $I_C(B)$ with multiple nodes and lobes but without clear periodicity was observed in semiconductor nanowire based Josephson junctions in an axial field [130, 131]. Though, a regular periodicty as observed in some of our devices was not observed.

Only a fraction of the investigated junctions show a modulation of the critical current as a function of the flux, while the critical current monotonously decreases with the magnetic field for other samples. Even the exact shape and periodicity of the pattern, if it exists, differs for various devices. Therefore, we analyze the emergence of $I_C(B)$-oscillations for different experimental parameters in the following.

Gated devices

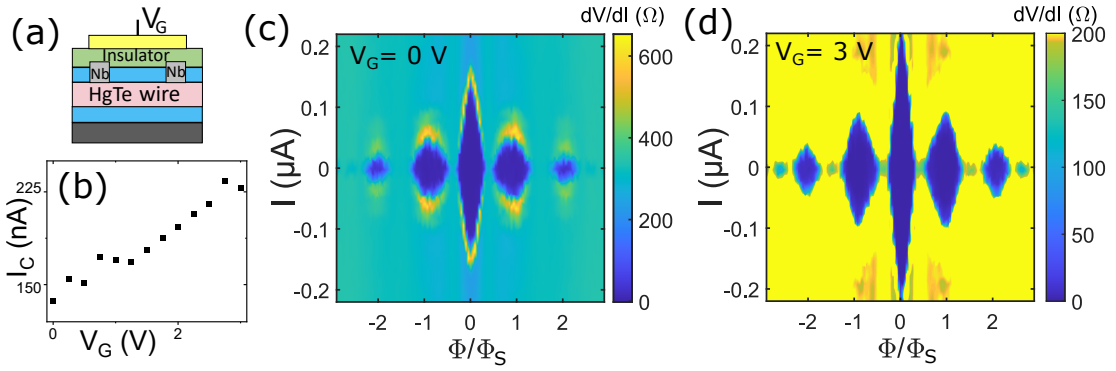

FIG. 5.4: Gate dependence of $I_C(B)$-oscillations for sample rI. (a) Sketch of the sample layout. An insulator and a metallic topgate is placed on top of the junction. (b) The critical current I_C increases for higher gate voltages V_G. (c) Color map of the differential resistance dV/dI as a function of the current I and the magnetic flux Φ/Φ_S at $V_G = 0$. The critical current oscillates with a period of Φ_S. (d) The corresponding color maps at $V_G = 3\,\mathrm{V}$. Additional oscillations of I_C appear recovering the $\Phi_S/2$-periodicity.

Figure 5.4(c) shows the data of sample rI. This device has a critical current $I_C = 136\,\mathrm{nA}$ and an average transmission $D = 0.43$ while one superconducting flux quantum Φ_S corresponds to $B \approx 50\,\mathrm{mT}$. Here, we also observe $I_C\,(B)$-oscillations. However, only maxima at $\Phi = j \cdot \Phi_S$ are visible leading to a $h/2e$ periodicity. For more detailed studies, a topgate was added to the junction. This allows to investigate the $I_C\,(B)$-oscillations as function of the gate voltage V_G. The structure of a gated device is sketched in figure 5.4(a). An insulator made of $\sim 30\,\mathrm{nm}$ SiO_2 and $\sim 100\,\mathrm{nm}$ Al_2O_3 was deposited above the junction. The topgate voltage V_G is applied via a metallic Ti/Au layer. Figure 5.4(b) shows the critical current I_C as a function of the topgate voltage V_G. By tuning V_G from $0 - 3\,\mathrm{V}$, I_C increases by a factor ~ 1.7. Figure 5.4(d) illustrates $dV/dI\,(\Phi,\, I)$ of sample rI for $V_G = 3\,\mathrm{V}$. Additional maxima

appear at $\Phi = (2j+1) \cdot \Phi_S/2$ in contrast to the data at $V_g = 0$. Hence, the $h/4e$ periodicity is recovered by increasing V_G. This observation emphasizes that the $h/2e$ oscillations are the dominating ones and are observable for any V_G. The maxima at $\Phi = (2j+1) \cdot \Phi_S/2$ cannot be resolved for $V_G = 0$ due to the low I_C at these positions. By increasing V_G, the number of contributing channels rises enabling to resolve I_C at $\Phi = (2j+1) \cdot \Phi_S/2$. Compared to sample rG, however, $I_C(B)$-oscillations with a period of $h/8e$ are not observable, although the transmissions of the devices are similar. As sample rG stems from a doped wafer, the electron density is much higher and a large amount of transport channels contributes to the signal. Such high densities cannot be reached in the undoped sample, even for high gate voltages. Thus, we conclude that the number of transport channels influences the period of the $I_C(B)$-pattern where more channels lead to the visualization of higher periodicities.

Influence of the transmission

In addition to differences in geometry, the transmission of the superconductor /nanowire interface is the decisive parameter that differentiates the devices studied. Figure 5.5 shows color maps of the differential resistance dV/dI as a function of the current I/I_C and the magnetic flux Φ/Φ_S for several samples with different transmissions. The transmission D_{OBTK} is calculated as explained in section 4.3. The extracted transmission gives a value averaged over all contributing transport channels. Thus, it can vary locally at the superconductor/nanowire interface. In Figure 5.5, the color maps are ordered by the transmission of the devices, descending from the highest (a) to the lowest (i) values. Moreover, the capital letter in the labeling of the devices A-I follows the labeling in the figure (a)-(i)[2]. Devices wA and wB have the highest transmissions $D_{OBTK} \approx 0.70$ and $D_{OBTK} \approx 0.66$ among the samples investigated. For these high-transmission devices, the critical current I_C monotonously decays by increasing the magnetic flux Φ. For samples with slightly lower transmission $D_{OBTK} \approx 0.64$ and $D_{OBTK} \approx 0.63$, as in samples wC and rD, the monotonic decrease of the critical current still prevails, but an additional shoulder comes out. This shoulder can be considered as a precursor of the oscillations appearing at still lower transmissions. The oscillations start for device wE ($D_{OBTK} \approx 0.62$). Initially, I_C decreases and is almost fully suppressed below $\Phi = \Phi_S$. Then, I_C increases again and shows a maximum around $\Phi = \Phi_S$. The oscillations become more pronounced for samples wF ($D_{OBTK} \approx 0.57$), rG ($D_{OBTK} \approx 0.51$), wH ($D_{OBTK} \approx 0.49$), and rI ($D_{OBTK} \approx 0.43$) which have even lower transmissions. These samples show clear $I_C(B)$-oscillations with periodicities $h/2e$ or $h/4e$. For samples

[2]The lower case letter indicates the fabricator of the sample: Samples starting with 'w' were fabricated and measured by W. Himmler.

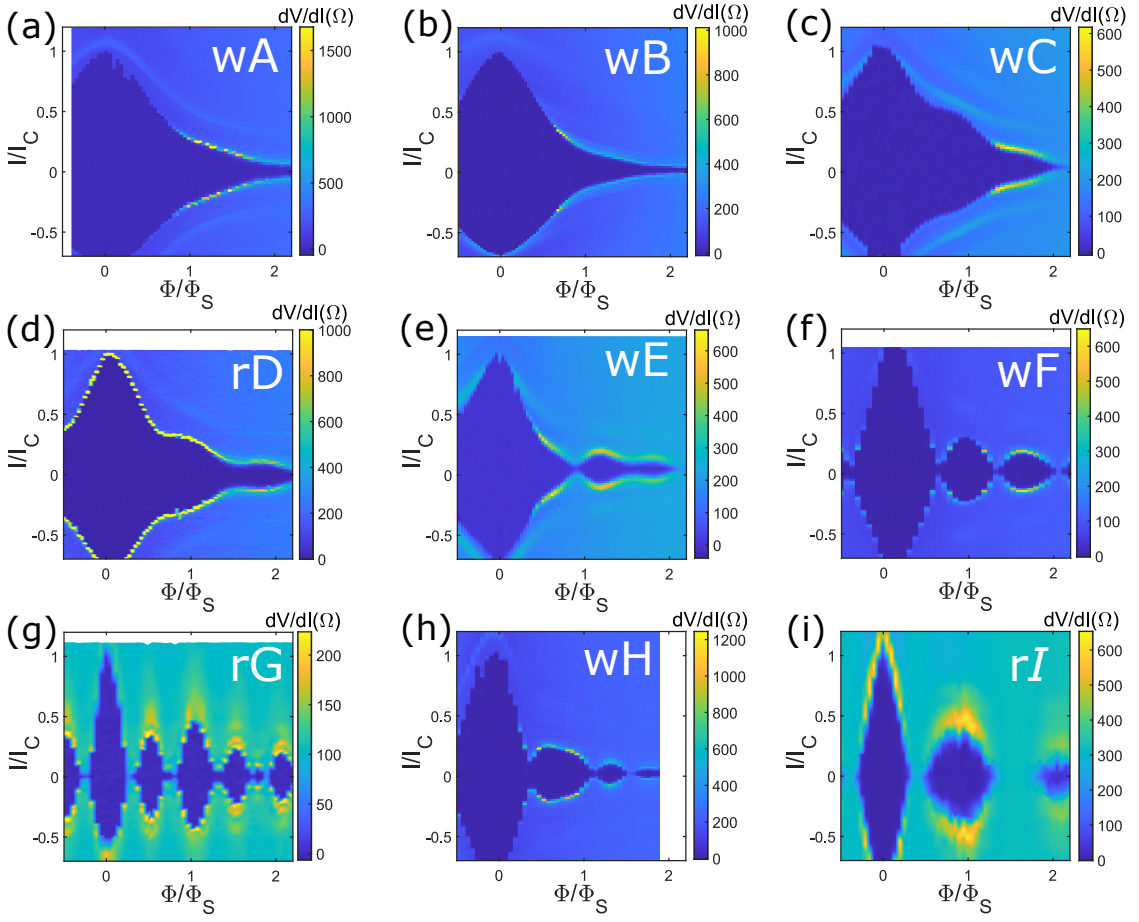

FIG. 5.5: Impact of sample transmission on $I_C(B)$-oscillations. Color maps of the differential resistance dV/dI as a function of the normalized current I/I_C and the magnetic flux Φ/Φ_S for different samples. The color maps are ordered by decreasing transmission of the junctions with the highest transmission shown in (a) to the lowest in (i). (a-b) Samples with high transmission ($D_{OBTK} \approx 0.70$ and $D_{OBTK} \approx 0.66$) show no oscillations as a function of the magnetic field. (c-e) For intermediate transmissions ($D_{OBTK} \approx 0.64$, $D_{OBTK} \approx 0.63$, and $D_{OBTK} \approx 0.62$), the shape of the $I_C(B)$-contour starts to deviate and first shoulders are observable. (f-i) Samples with the lowest transmissions ($D_{OBTK} \approx 0.57$ to $D_{OBTK} \approx 0.43$) show distinct oscillations as a function of the axial magnetic field. Samples with initial letter 'w' were fabricated and measured by W. Himmler.

rG and rI, the maxima appear exactly at positions $\Phi = j \cdot \Phi_S/2$ and $\Phi = j \cdot \Phi_S$, respectively, while the positions are slightly shifted for devices wF and wH.

Based on these experimental observations, we conclude that the transmission D_{OBTK} is the most influential parameter that determines whether $I_C(B)$-oscillations occur or not. The oscillations appear preferentially for samples with low average transmission, while they are fully absent for high transmissions.

5.2.2 Theoretical model

To understand the observed experimental phenomena, a theoretical model was developed by J. Fuchs and M. Barth [132–134]. Within this model, semiclassical and numerical simulations were performed to explain the experimental findings. Here, we outline the basic principles of the model in a simplified way and show the results of the simulations. A more detailed version of the theory can be found in [132, 133].

Geometry and model

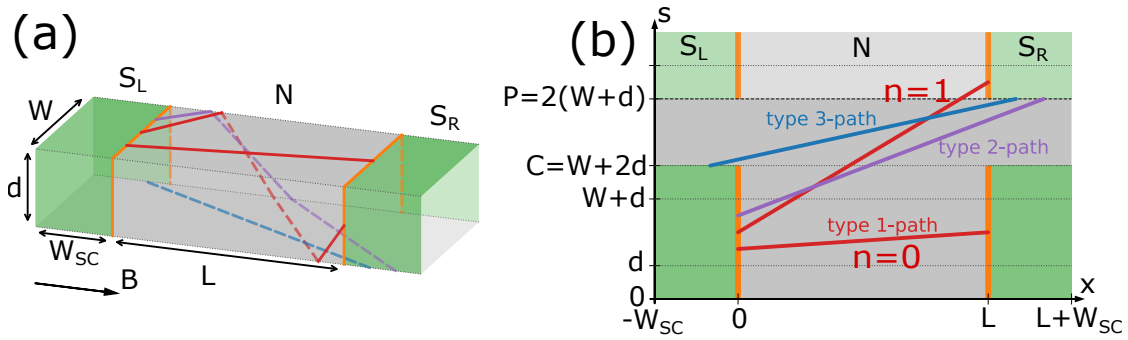

FIG. 5.6: (a) Sketch of the topological insulator nanowire Josephson junction. The surfaces are illustrated in gray while surfaces with proximity induced superconductivity are shown in green. The bottom side of the nanowire is not affected by the induced superconductivity. The barriers at the NS interfaces are marked in orange. The different types of paths are illustrated in red, purple, and blue, respectively. (b) Sketch of the uncoiled nanowire to improve the illustration of the different types of paths. Adapted from [132].

The geometry of the model is presented in figure 5.6(a). To improve the visualization of the different parameters, the uncoiled nanowire is sketched in figure 5.6(b). Here, we define the coordinate s which winds around the perimeter. The nanowire with a rectangular cross-sectional area A is considered to be orientated along the x-axis. It is contacted by two superconducting leads with width W_{SC}. The distance between the leads is given by L. The width of the nanowire is labeled as W, while d is its height. Thus, the perimeter is $P = 2(W + d)$. The magnetic field B is aligned along

the wire just like in the experiment. In the model, only surface states are considered while any contribution of the bulk is neglected. Since only the top surface and the side surfaces of the nanowire are covered by a superconductor, these surfaces are assumed to become superconducting by the proximity effect. The bottom surface stays normal-conducting. Thus, the superconducting pairing is given by

$$\Delta = \begin{cases} \sigma_0 \Delta_0 \mathrm{e}^{i\phi_L} & \text{for } 0 \leq s \leq C \text{ and } -W_{SC} \leq x \leq 0 \\ \sigma_0 \Delta_0 \mathrm{e}^{i\phi_R} & \text{for } 0 \leq s \leq C \text{ and } L \leq x \leq L + W_{SC} \\ 0 & \text{otherwise} \end{cases} \tag{5.2.1}$$

with a constant Δ_0, the phase difference of the superconductors $\varphi = \phi_L - \phi_R$, and the length of the perimeter which is covered by the superconductor $C = W + 2d$. Additionally, the potential U describing the barrier between the nanowire and the superconductor can be written as

$$U(x,\, s) = \begin{cases} U_0[\delta(x) + \delta(x - L)] & \text{for } 0 \leq s \leq C \\ 0 & \text{otherwise} \end{cases} \tag{5.2.2}$$

with a constant U_0. In figure 5.6(a), the superconducting regions are illustrated in green, while the normal-conducting parts are gray. The barrier is shown in orange. The choice of the introduced barrier is justified by taking a closer look at the fabrication process of the nanowire junctions. We assume a low average transmission since the $I_C(B)$-oscillations preferentially appear in such devices. A low average transmission is most likely caused by an incomplete removal of the cap layer in the fabrication process. This only concerns the top surface of the nanowire. The corresponding barriers are at $x = 0 \vee x = L$ and $d < s < d + W$. The side surfaces are already fully uncovered by the etching of the nanowire. Thus, the transmission at the side surfaces is much higher than the transmission at the top surface if the average transmission of the whole device is rather low. This explains the absence of a barrier at $s = C$ or/and $s = 0 \equiv P$, which corresponds to the lowest part of the side surfaces. Strictly speaking, the barrier should also be missing at $x = 0 \vee x = L$ and $0 < s < d$, $W + d < s < W + 2d$ as this is also a part of the side surface. Though, this deviation from the experimental situation does not qualitatively affect the results, but simplifies the classification of the paths.

Classification of the trajectories

The idea of the semiclassical analysis is that each classical trajectory between the leads contributes a current i to the total current I_S. By considering only straight paths and neglecting normal reflections, the total current is the integral over all trajectories:

$$I_S \sim \int ds \int dk_s i\,(s,\, k_s)\,. \tag{5.2.3}$$

The trajectories can be classified into three different categories and the integral for each is evaluated separately. The classification of the trajectories is based on its starting point and end point. For the sake of simplicity, we use a fixed direction for the explanation of the paths. The different paths are visualized in figure 5.6.

- Type-1 paths are 'direct' paths. The starting point at the left S_LN interface is located at $x = 0$ while the end point at the right S_RN interface is at $x = L$. If the wire is fully surrounded by a superconductor, i.e. $C = P$, this type of paths exists exclusively.
- Type-2 paths are 'mixed' paths. The starting point at the left S_LN interface is also located at $x = 0$. However, the end point is at $s = 0 \equiv P \vee s = C$ and $L < x \leq L + W_{SC}$ at the S_RN interface. Since this scenario can also take place with exchanged interfaces, we can divide these paths further into type-2L and type-2R paths depending whether they start on the S_LN or S_RN interface.
- Type-3 paths are 'side' paths. They start at $s = 0 \equiv P \vee s = C$ and $-W_{SC} \leq x < 0$ at the S_LN interface while the end is at $s = 0 \equiv P \vee s = C$ and $L < x \leq L + W_{SC}$ at the S_RN interface.

Additionally, a crossing number n is assigned to every path. For a given slice along the x-axis in the region $C < s < P$, we count the number a path crossing this slice. Here, a positive count indicates a passing through in positive s-direction, while a negative count labels a passing through in negative s-direction. Exemplarily, figure 5.6(b) illustrates the crossing numbers $n = 0$ and $n = 1$ for a red type-1 path. Additionally, we notice that no paths of type-2 and type-3 with crossing number $n = 0$ exist.

Andreev bound states

The modeled system is described by the BdG Hamiltonian of a topological insulator nanowire proximitized by an s-wave superconductor as it was derived in section 2.3.5:

$$\mathcal{H} = \begin{pmatrix} H_{Wire} & \Delta \\ \Delta^* & -\sigma_y H^*_{Wire} \sigma_y \end{pmatrix} \tag{5.2.4}$$

where the Hamiltonian of the nanowire in the normal-state is given by

$$H_{Wire} = \hbar v_F \left[-i\partial_x \sigma_x + \left(-i\partial_s + \frac{4\pi}{P} \frac{\Phi}{\Phi_S} \right) \sigma_y \right] - \mu\sigma_0 + U\sigma_0. \tag{5.2.5}$$

Here, small adjustments compared to section 2.3.5 are applied: $1/R$ is replaced by $2\pi/P$ and ∂_φ by $\frac{P}{2\pi}\partial_s$ ($\hat{k}_\varphi$ by $\frac{P}{2\pi}\hat{k}_s$) to account for the rectangular shape of the wire [56, 132].

To calculate the current contribution i for each classical trajectory, the Andreev bound states for a type-m path are calculated using a scattering matrix approach [132]. Similar to equation (2.3.25), they yield

$$E_{m,n} = \pm\Delta_0\sqrt{1 - D_m \sin^2\left(\frac{1}{2}\varphi_0 - \gamma\right)}. \tag{5.2.6}$$

Here, the values for the transmission D_m depend on the specific type of the path, where θ is the angle of its incidence:

$$D_1 = \frac{1}{\sin^2(\varphi_N) + \left[1 + 2Z^2\left(1+Z^2\right)^{-1}\tan^2(\theta)\right]^2 \cos^2(\varphi_N)},$$
$$D_2 = \frac{1}{1 + Z^2\left(1+Z^2\right)^{-1}\tan^2(\theta)}, \quad \text{and} \quad D_3 = 1$$

with

$$\varphi_N = 2\arctan\left(\frac{\cos(\theta) + Z\tan(\theta)}{Z - \sin(\theta) - \sqrt{1 + Z^2 + Z^2\tan^2(\theta)}}\right)$$

and $Z = U_0/\hbar v_F$. Thus, type-1 paths have barriers at both NS interfaces. Type-2 paths have a barrier at one NS interface while $Z = 0$ at the other NS interface. For type-3 paths, $Z = 0$ at both NS interfaces. Additionally, the gauge-invariant phase difference $\varphi_0 - 2\gamma$ appears in equation (5.2.6). The phase difference between the left and the right superconducting lead is described by φ_0. The second part of the phase is induced by the magnetic field. It evolves for transport paths which wind around the perimeter and pick up an Aharonov-Bohm phase [66]

$$\gamma = \frac{e}{\hbar}\int d\vec{s}\cdot\vec{A} = 2n\pi\frac{\Phi}{\Phi_S}. \tag{5.2.7}$$

Theoretical results

In figure 5.7, we present the results of the semiclassical model. Here, the current i for every trajectory is determined from the energy-phase relation (5.2.6). The supercurrent I_S is given by the integral over all trajectories. For the calculations, realistic parameters were used: The width of the nanowire is $W = 300\,\text{nm}$, its height is $d = 80\,\text{nm}$, the width of the superconducting contacts is $W_{SC} = 1\,\mu\text{m}$, and the distance between them is $L = 200\,\text{nm}$. The chemical potential is set to $\mu = 30\,\text{meV}$, $\hbar v_F = 330\,\text{meV nm}$, $k_F = 0.09\,\text{nm}^{-1}$, and $\Delta_0 = 0.8\,\text{meV}$. Only paths with crossing numbers $n = 0, \pm 1$ are considered. A low barrier $U_0 = 100\,\text{meV nm}$ is assumed for the results shown in figure 5.7(a). In the upper panel, the current-phase relation is shown for different values of the magnetic flux. The current-phase relation shows a jump whenever there is a sign change in the Andreev bound state. This happens

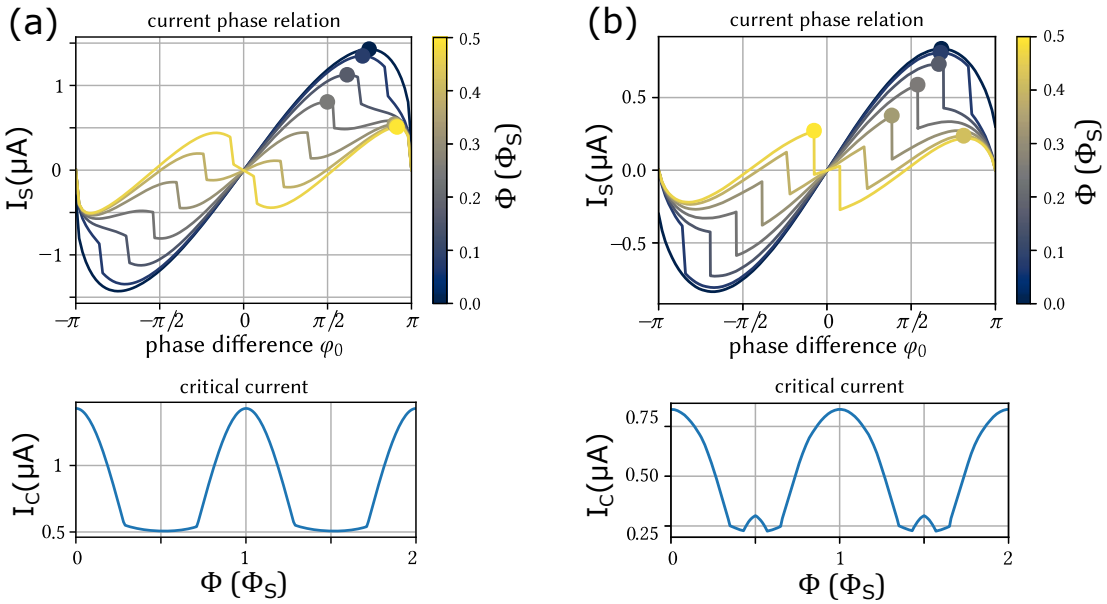

FIG. 5.7: Results of the semiclassical analysis. (a) Current-phase relation for a low barrier strength $U_0 = 100\,\text{meV nm}$ and different values of the magnetic flux Φ (upper panel). The current arising from type-1 paths dominates while jumps in the current-phase relation occur at $\varphi_0 = \pm\pi \pm 2\pi\Phi/\Phi_S$ due to type-2 and type-3 paths. The maxima of the current-phase relation for a specific magnetic flux are indicated by circles. Critical current I_C as a function of the magnetic flux Φ when a low barrier is assumed (lower panel). The trace shows a period of $h/2e$. (b) Current-phase relation for a large barrier $U_0 = 600\,\text{meV nm}$ and different values of the magnetic flux Φ(upper panel). The current arising from type-2 and type-3 paths gains in importance. Critical current I_C as a function of the magnetic flux Φ for a large barrier (lower panel). The trace shows a period of $h/4e$. Adapted from [132].

at $\varphi_0 = \pm\pi$ for paths with crossing number $n = 0$. Paths with crossing numbers $n = \pm 1$ are shifted due to the Aharonov-Bohm phase. Therefore, the jumps occur at $\varphi_0 = \pm\pi + 2\pi\Phi/\Phi_S$ and at $\varphi_0 = \pm\pi - 2\pi\Phi/\Phi_S$. The maxima of the current-phase relation, i.e. the critical currents, for a specific magnetic flux are indicated by circles. The critical current as a function of the magnetic flux is shown in the lower panel of figure 5.7(a). Here, the critical current oscillates with a period of $\Phi_S = h/2e$. In the scenario described, the current carried by type-1 paths manifests the dominating contribution to the results obtained.

By considering a higher barrier $U_0 = 600\,\text{meV nm}$, the results change. The transmissions D_1 and D_2 of type-1 and type-2 paths decrease, while type-3 paths are not affected by the barrier. Thus, especially the current of type-1 paths drops its predominance, and the paths with crossing numbers $n = \pm 1$ gain in importance. The upper panel of figure 5.7(b) illustrates the resulting current-phase relation for different values of the magnetic flux while the critical current as a function of the

magnetic flux is shown in the lower panel. The critical current shows oscillation with a period of $\Phi_S/2 = h/4e$. Here, the additional peaks at $\Phi = (2j+1) \cdot \Phi_S/2$ with j an integer are weaker similar as observed in the experiment. At this point it is worth mentioning that the enveloping drop of the critical current with the magnetic field is not considered in the model.

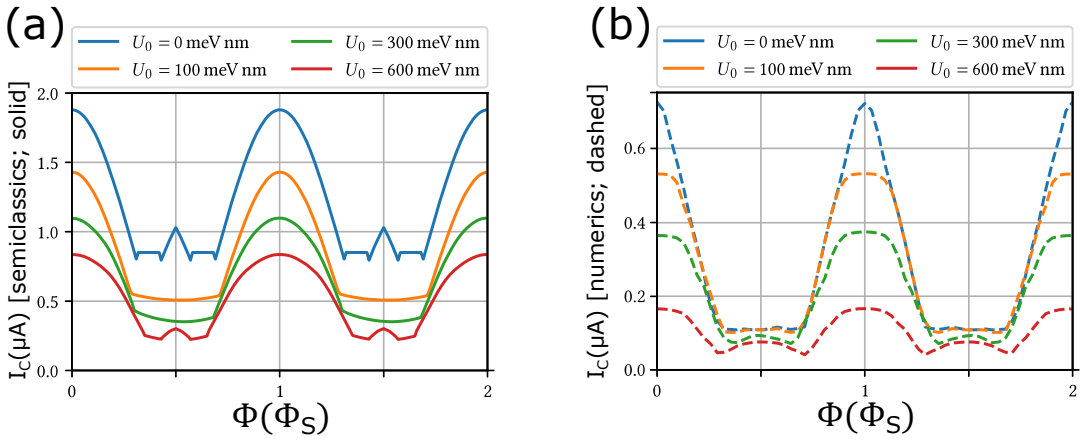

FIG. 5.8: (a) Results of the semiclassical analysis. For a small barrier strength U_0 (green and orange), the critical current I_C oscillates as a function of the magnetic flux Φ with a period of $h/2e$. By increasing the barrier, additional maxima appear leading to a $h/4e$ periodicity (red). A peak at $\Phi = (2j+1) \cdot \Phi_S/2$ also exists for $U_0 = 0$. Though, it immediately vanishes by introducing a small barrier. (b) Results of the numerical analysis. The results are qualitatively similar to the semiclassical analysis. However, the peak at $\Phi = (2j+1) \cdot \Phi_S/2$ for $U_0 = 0$ is absent in the numerics. Adapted from [132].

Figure 5.8(a) presents the critical current I_C as a function of the magnetic flux Φ_S for different barrier strengths U_0. Additionally, the numerical results from M. Barth [133, 134] are illustrated in figure 5.8(b). The latter are obtained by numerical tight-binding simulations with the Python package Kwant [135]. The semiclassical and the numerical results show the same qualitative behavior: $I_C(B)$-oscillations with a period of $h/2e$ are observed for low barriers, whereas a period of $h/4e$ evolves with an increasing barrier. The main difference between semiclassics and numerics is that a peak at $\Phi = (2j+1) \cdot \Phi_S/2$ also exists for $U_0 = 0$ in the semiclassical analysis only. It immediately vanishes by introducing a small barrier and appears again for high barrier strengths. However, this feature is not reproduced in the numerical simulations. A possible reason is that the numerical simulation respects the length of the different types of paths which is not captured by the semiclassical analysis. This causes that the type-2 paths have too much weight in the semiclassics. Furthermore, the critical currents obtained from the numerical simulations are smaller.

The same calculations were also performed for the Hamiltonian of a metal instead of the Hamiltonian of a topological insulator nanowire (5.2.5). The metallic Hamiltonian does not capture the topological properties of the system. The results show

qualitatively the same behavior as for the Dirac-like Hamiltonian [132]. Thus, the $h/4e$ oscillations have their origin in the geometry of the system, and a topological nature of the surface states is not required to experimentally observe them.

Comparison to the experiment

Finally, we summarize the experimental observations and relate them to the theoretical model. The $I_C(B)$-oscillations appear preferentially for samples with low average transmission. A low average transmission is caused by a bad transmission at the top interface while the transmissions at the side interfaces are rather high. As a consequence, transport channels of type-2 and type-3 provide a significant contribution to the signal. This leads to the $h/4e$ oscillations as illustrated by the theoretical model. For a low contribution of type-2 and type-3 paths, one would only expect $h/2e$ oscillations.

For samples with high average transmission, the coupling of the superconductor to the nanowire is quite good. Here, we expect a wide impact of the superconductivity. Thus, also the bottom side of the nanowire gets proximitized by the superconductivity. With this assumption, no transport channels of type-2 and type-3 with crossing numbers $n \neq 0$ exist, and only type-1 paths are present. Hence, the additional phase difference in equation (5.2.6) vanishes, and the Andreev bound states are similar to the ones of a planar junction. Here, the critical current monotonously decreases due to the reduction of Δ_0 by the magnetic field.

For sample rG, oscillations with a period of $h/8e$ are observed. Such period is expected if paths with crossing numbers $n = \pm 2$ provide a significant contribution to the current. The fact that these period is only observed for sample rG is explained by the high amount of transport channels compared to other samples. Here, the probability that a few contributing channels with crossing number $n = \pm 2$ exist is higher.

A similar argumentation can be applied for sample rI where $h/4e$ oscillations are only observed for $V_G = 3\,\mathrm{V}$. The maxima at $\Phi = (2j+1) \cdot \Phi_S/2$ cannot be resolved for $V_G = 0$ due to the low contribution of type-2 and type-3 channels to the absolute current. By increasing V_G, the number of contributing type-2 and type-3 channels raises leading to the resolution of the maxima at $\Phi = (2j+1) \cdot \Phi_S/2$.

Similar to previous works on semiconductor wires [130, 131], deviations from a $h/2e$ or $h/4e$ periodicity are observed for samples wE, wF, and wH. They were ascribed to subband supercurrent interference [136]. Here, the phase picked up by the quasiparticles depend on the difference of their wave numbers, the length of the junction, and the angular momentum quantum number. Since these oscillations depend on many parameters, they do not necessarily show any periodicity in the flux quantum. The fact that such oscillations are observed in several of our devices

while others show a clear periodicity in the flux quantum could not be clarified so far. One notable difference between the respective devices is the width of the superconducting contacts. For the samples (rG and rI) which show a periodicity with the flux quantum, $W_{SC} \approx 550 - 700\,\mathrm{nm}$. This value is significantly smaller than in samples (wE, wF, and wH) that showed no clear periodicity.

For the detection of Majorana bound states in chapter 6, we preferentially study devices which show a monotonic decay of I_C by increasing Φ, i.e. junctions with high transmission. For these devices, superconductivity is induced into the whole wire. This assumption is made in the theoretical proposals for the appearance of Majorana bound states in topological insulator nanowires. Thus, such devices are most promising for the verification of the theory.

5.3 Resistance oscillations in an axial magnetic field

In addition to the described $I_C(B)$-oscillations, other phenomena were also found in an axial magnetic field that were only observed on certain devices. Sample r1 shows oscillations of the resistance R as a function of the magnetic flux Φ/Φ_0 at the transition from the superconducting to the normal state. Note that we use the normal flux quantum $\Phi_0 = h/e$ at this point. A plot of the resistance $R(\Phi)$ is shown in figure 5.9(a) (blue trace). The resistance R increases from $R = 0$ to $R = R_N$ between $\Phi = 2\,\Phi$ and $4\,\Phi$. This corresponds to the transition from the superconducting state to the normal state. In the rise, oscillations of the resistance appear. To improve the visualization of the oscillations, we substract the background by a high-pass filter algorithm with a cutoff frequency of 0.6 Hz. The resulting trace is shown in red. Here, the oscillations are clearly visible. They show a period of $\sim h/3e$.

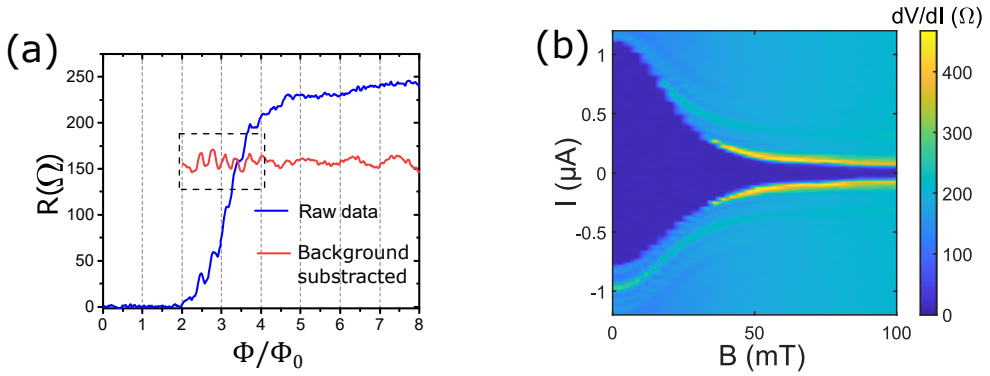

FIG. 5.9: (a) Resistance R of sample r1 as a function of the magnetic flux Φ (blue trace). Between $\Phi = 2\,\Phi_0$ and $4\,\Phi_0$, R increases from 0 to R_N resembling the transition from the superconducting state to the normal state. Oscillations with period of $h/3e$ occur during this ascent. The visualization of the oscillations is improved by subtracting the background, which is executed by a high-pass filter algorithm with a cutoff frequency of 0.6 Hz. The resulting trace is shown in red. (b) Color map of the differential resistance dV/dI as a function of an axial magnetic field B and the current I for sample r1. The critical current I_C monotonously decays by increasing B.

To check if these oscillations are related to the $I_C(B)$-oscillations shown in the previous section, we plot the color map of the differential resistance dV/dI as a function of an axial magnetic field B and the current I for sample r1 in figure 5.9(b). No $I_C(B)$-oscillations are observed due to the high transmission of sample r1. Thus, we assume a relation to the $I_C(B)$-oscillations to be improbable.

Another possible explanation could point to the Little-Parks effect which was discovered by W. A. Little and R. D. Parks in experiments with empty and thin-walled superconducting cylinders in an axial magnetic field [137]. As the topological surface

states of the nanowire may resemble such a cylinder, this is worth taking a closer look at. In the Little-Parks experiment, the resistance of the cylinders showed an oscillation with period of $h/2e$ as a function of the magnetic flux penetrating the cross-sectional area of the cylinder. This resistance oscillations reflect periodic oscillations of the critical temperature T_C. To understand this effect, one has to recall that the flux which is trapped in a superconducting cylinder is an integer multiple of $h/2e$ [138, 139]. By applying the magnetic flux, the kinetic energy of the superconducting electrons is increased. However, superconducting vortices appear periodically, and reduce the kinetic energy again. Thus, the kinetic energy oscillates as a function of the flux. Since the kinetic energies of normal and superconducting electrons are equal at T_C, the critical temperature T_C must also be a periodic function of the enclosed flux Φ/Φ_0 [137].

In our experiment, the transition from the superconducting state to the normal state is spread over a finite interval $(2\,\Phi_0 - 4\,\Phi_0)$. Hence, the critical temperature T_C varies for different parts of the nanowire at a given magnetic field. Since for a certain part of the nanowire the temperature is very close to T_C, Little-Parks oscillations which have their origin in the oscillation of T_C, should be apparent in the interval $2\,\Phi_0 - 4\,\Phi_0$ if they are present at all. Therefore, the regime, in which the oscillations occur, fit perfectly to the Little-Parks effect. However, the fact that we observe a period of $h/3e$, although a period of $h/2e$ is predicted, speaks against the Little-Parks effect. Deviations from the theoretical period could also be found in other works, e.g. $h/4e$ oscillations in disordered $Au_{0.7}In_{0.3}$ cylinders [140] or periodicities h/e, $3h/2e$, and $2h/e$ [141] in combination with a phase shift by a half flux quantum [142] in the topological superconductor β-Bi_2Pd. However, a period of $h/3e$ was not observed so far.

Therefore, no fully satisfying explanation can be given for the $R(\Phi)$-oscillations occurring in our experiment at the moment. Further experiments on several devices is necessary to get better insights into the observed behavior.

6 4π-periodic supercurrent in topological insulator nanowires

Topological insulator nanowires in proximity to conventional superconductors have been proposed as a tunable platform to realize topological superconductivity [23, 24]. The tuning is done using an axial magnetic flux Φ which allows transforming the system from trivial at $\Phi = 0$ to topologically nontrivial when half a magnetic flux quantum $\Phi_0/2$ penetrates the cross-sectional area of the wire. In this chapter, we explore the expected topological transition in Josephson junctions based on topological insulator nanowires. To probe signatures of topological superconductivity in our system, we measure the I-V characteristics under microwave irradiation and at millikelvin temperatures ($T_{bath} \approx 40\,\mathrm{mK}$). With a microwave field, quantized Shapiro steps appear at voltages $V_n = nhf/2e$. In the case of topological superconductivity, the current-phase relation is 4π-periodic, and the odd Shapiro steps, i.e. $n = 1, 3, ...$ are partially missing.

6.1 Microwave response in the absence of a magnetic field

The experimental setup to detect Shapiro steps is sketched in figure 6.1(a). An open-ended coaxial cable is placed a few millimeters away from the sample emitting microwave radiation. We are able to achieve frequencies in the range from 1.5 to 12 GHz. Firstly, we concentrate on the results in the absence of a magnetic field. Exemplarily, we show the results of sample r1 while samples r2, r3, and w1 show consistent results.

The I-V traces of sample r1 with and without applying microwaves are shown in figure 6.1(b). Without microwaves (blue line, right axis), a supercurrent of about $I_C = 1\,\mu\mathrm{A}$ flows across the junction. With microwaves turned on (red and green line, left axis), Shapiro steps appear in the I-V trace. Even and odd voltage steps appear for $f = 5.9\,\mathrm{GHz}$ while the $n = 1$ step, indicated by the black arrow, is missing, and the $n = 3$ step is barely visible at $f = 5.4\,\mathrm{GHz}$. To improve the visualization of the steps, we use bar charts. Here, the V-axis is divided into small intervals of $0.25\,hf/2e$ and the data points within them are counted. The intervals are illustrated

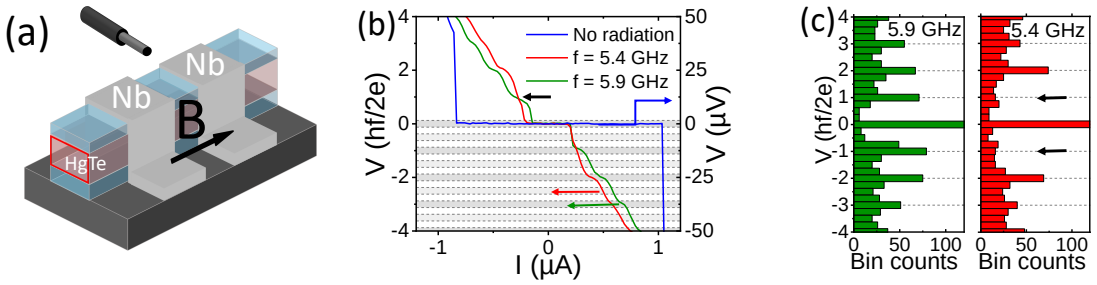

FIG. 6.1: (a) Sketch of the experimental setup. The magnetic field B is orientated along the nanowire while microwave radiation is applied via an antenna in vicinity to the sample. (b) I-V trace of sample r1 (blue trace). The junction has a critical current of $I_C \approx 1\,\mu A$. By adding microwave radiation, Shapiro steps appear in the I-V traces (red and green traces). The $n = \pm 1$ steps are visible at 5.9 GHz, while the first steps are absent at a lower frequency of 5.4 GHz. This is indicated by the black arrow. The V-axis is divided into intervals of $0.25\,hf/2e$ to create histograms. The intervals are shown for negative voltages. (c) Histogram of the data shown in (b) where the data points within each interval are counted. With this illustration, the missing first steps for $f = 5.4$ GHz are even better recognizable.

for negative voltages in figure 6.1(b). The corresponding histograms are shown in figure 6.1(c). An accumulation of data points marks a flat line in the I-V traces, i.e. a Shapiro step. Thus, the missing $n = 1$ plateau (black arrows) is clearly observable for $f = 5.4$ GHz in the bar plots while the $n = 1$ step is present for $f = 5.9$ GHz. For a quantitative study, we measure the frequency and power dependence which both affect the Shapiro steps. Figures 6.2(a-c) show color maps at three frequencies as a function of the power at $B = 0$. An increasing microwave power enhances the ac current flowing across the junction. For the color maps, the histograms are created as explained above. The color maps show these histograms as a function of microwave power. Yellow regions mark an accumulation of data points, i.e. Shapiro steps. For the evaluation of the maps, we limit ourselves to the low power regime which corresponds to the area up to the dashed line in figure 6.2(a). For higher powers, oscillations appear which are described by Bessel-like functions [83], but they are not of interest here. All Shapiro steps are visible for $f = 6.6$ GHz whereby steps with a lower index n appear at a lower power. By reducing the frequency to $f = 5.4$ GHz, the first steps $n = \pm 1$ becomes completely suppressed, and the third ones are slightly reduced, i.e. they start to disappear at lower powers. The sequence of all other steps is unchanged. At $f = 3.7$ GHz, the third steps are also fully quenched while the fifth ones are strongly reduced. So far, only a missing first step was observed in the literature [17, 33, 37], except in Josephson junctions made of 2D HgTe [34]. The absent higher steps $n \geq 3$ show the high quality of our samples and prove that hysteresis, occurring on a smaller bias current scale, is not the origin of the missing steps.

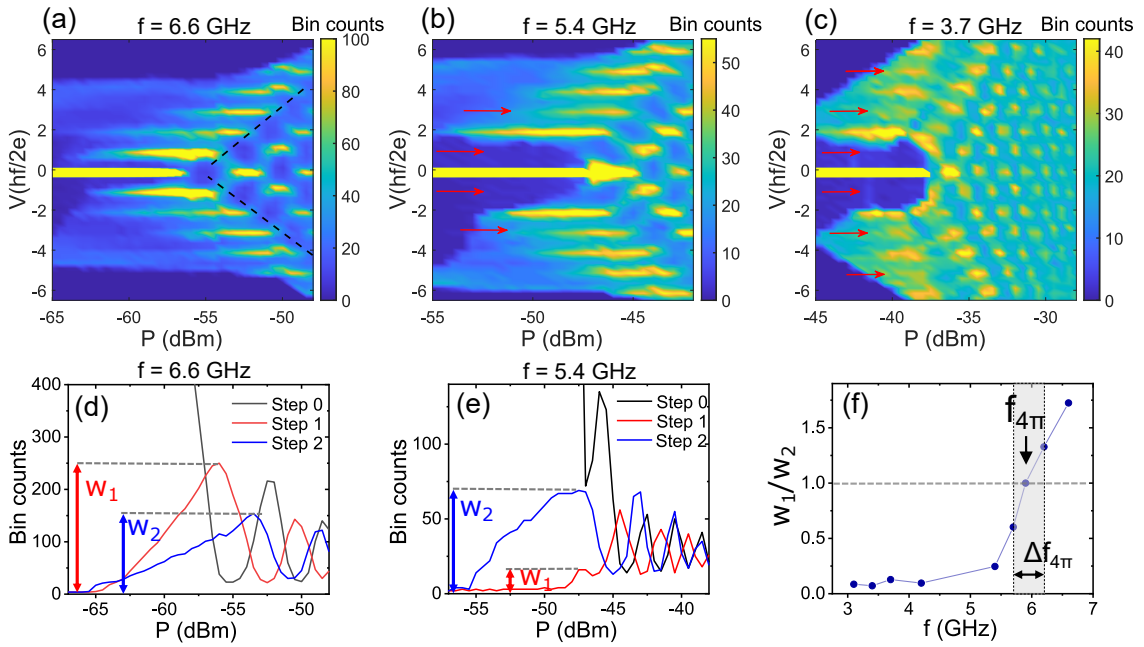

FIG. 6.2: (a-c) Color maps of the bin counts of sample r1 at frequencies $f = 6.6\,\mathrm{GHz}$, $5.4\,\mathrm{GHz}$, and $3.7\,\mathrm{GHz}$. The yellow color marks a step in the I-V traces. For the highest frequency, all Shapiro steps are visible. By lowering the frequency, the first step disappears and the third ones become slightly suppressed. Red arrows mark missing or suppressed steps. For the lowest frequency shown, the third step is also strongly suppressed while the fifth one is further reduced. (d-e) Amplitude of the Shapiro steps as a function of the microwave power P for the above color map, respectively. At $f = 6.6\,\mathrm{GHz}$, the maximum amplitude w_1 of the first Shapiro step is larger than of the second one w_2. For $f = 5.4\,\mathrm{GHz}$, the amplitude of the first step is almost fully suppressed and the second step dominates. (f) The ratio $\mathrm{w}_1/\mathrm{w}_2$ as a function of the frequency. The ratio decreases by lowering the frequency. At the point $\mathrm{w}_1/\mathrm{w}_2 = 1$, the second step starts to dominate. We indicate this point as the transition frequency $f_{4\pi}$. The grayish background indicates the uncertainty $\Delta f_{4\pi}$ in the determination of $f_{4\pi}$.

All in all, our observations indicate a 4π-periodic Josephson effect in topological insulator nanowires at $B = 0$. This is surprising since the wire structure is topologically trivial (see section 2.3.5), and a pure 2π-periodic Josephson effect is expected. Nevertheless, the presence of the higher order odd plateaus as well as the missing steps preferably at low frequencies and powers suggest that trivial 2π-periodic modes are also present in addition to the 4π-periodic ones. Before giving a potential explanation for the 4π-periodic supercurrent at $B = 0$ in section 6.3, we analyze the experimental data using a resistively shunted junction (RSJ) model and an extended resistively and capacitively shunted junction (RCSJ) model. This also permits to extract the ratio $I_{4\pi}/I_C$ from frequency-dependent measurements of the Shapiro spectrum [39, 143, 144].

6.2 Modelling of the experimental results

In section 2.2.4, we showed that the RCSJ model can be used to describe the dynamics of Josephson junctions and the formation of Shapiro steps. Here, we use two different approaches to analyze our data. Firstly, we take a simplified RSJ model based on [33, 39, 143] where the capacitive term is neglected. As the RSJ model neglects several effects that may influence the observed Shapiro signatures, numerical simulations based on an extended RCSJ model were additionally performed aiming to reproduce the experimental results as accurately as possible. Here, the effects of Joule heating and the excess current are also implemented.

6.2.1 RSJ model in the presence of 2π- and 4π-periodic supercurrents

For the simplified RSJ model, the supercurrent I_S is assumed to be a linear combination of a 2π-periodic and a 4π-periodic supercurrent. This implies that the two contributions are completely independent of each other. Additionally, a sinusoidal 2π-periodic current-phase relation is used. As shown in figure 2.17(b), this is only valid for low transmissions. With these considerations, equation (2.2.26) is adapted to

$$I_{ext} = \frac{\hbar}{2eR_N}\frac{\partial\varphi}{\partial t} + I_{2\pi}\sin(\varphi) + I_{4\pi}\sin(\varphi/2) \tag{6.2.1}$$

with $I_{ext} = I_{dc} + I_{ac}\cos(\omega_{ac}t)$. We rewrite this equation to

$$\left(\frac{\hbar}{2e}\right)^2 \frac{1}{R_N}\frac{\partial\varphi}{\partial t} + \frac{d}{d\varphi}\left[E_J\left(1 - \frac{I_{2\pi}}{I_C}\cos(\varphi) - 2\frac{I_{4\pi}}{I_C}\cos(\varphi/2) - \frac{I_{ext}}{I_C}\varphi\right)\right] = 0 \tag{6.2.2}$$

where the washboard potential is given by the expression in the square brackets just as in equation (2.2.29). The additional 4π-periodic contribution provides a change in the washboard potential compared to section 2.2.4. The maxima of the 2π- and 4π- component is superimposed at every second maximum that they add up. On the other hand, for the maxima in between, the maximum of the 2π-periodic part meets a minimum of the 4π-periodic part. Assuming that the 4π-periodic part is much smaller than the 2π-periodic part, this results in a reduced maximum.

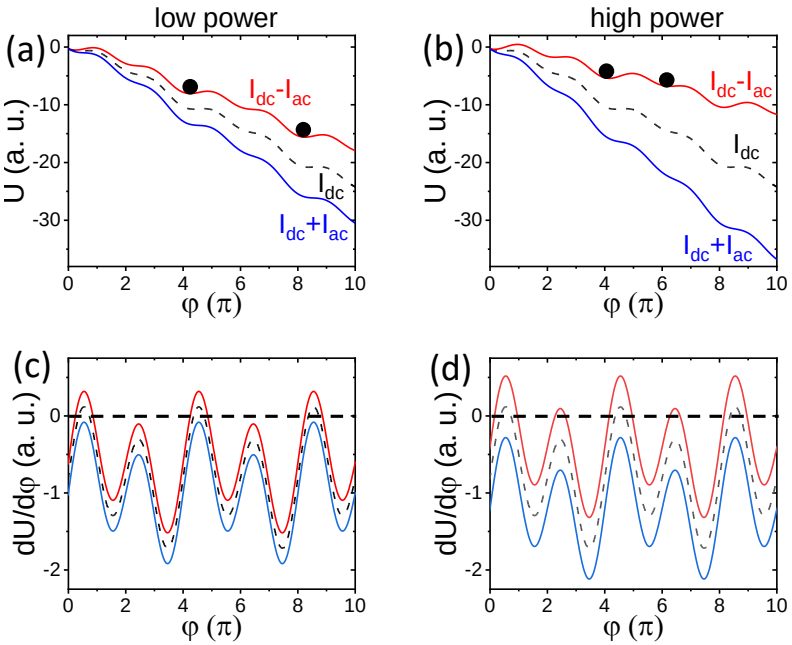

FIG. 6.3: (a-b) Washboard potential $U(\varphi)$ for two superconducting contributions $I_{2\pi}\sin(\varphi)$ and $I_{4\pi}\sin(\varphi/2)$ with $I_{4\pi} = 0.3\,I_C$, $I_{2\pi} = 0.7\,I_C$, and $I_{dc} = 0.8\,I_C$. In (a), the applied microwave power is $I_{ac} = 0.2\,I_C$. In (b), $I_{ac} = 0.4\,I_C$. The overall slope of the washboard potential changes between $I = I_{dc}+I_{ac}$ and $I = I_{dc}-I_{ac}$ during one period of oscillation. (c-d) Derivative $dU/d\varphi$ of the above washboard potential, respectively. During one oscillation, the slope $dU/d\varphi$ changes, and the phase particle slides down until the slope of the potential is positive again. Adapted from [145].

Firstly, we address the power dependence and explain why missing odd steps are preferably observed at low powers when the junctions are irradiated with microwave radiation. Therefore, the washboard potential is plotted for a low power ($I_{ac} = 0.2\,I_C$) and a high power ($I_{ac} = 0.4\,I_C$) in figure 6.2.1 (a-b). In both cases, $I_{dc} = 0.8\,I_C$, $I_{4\pi} = 0.3\,I_C$, and $I_{2\pi} = 0.7\,I_C$. The red line gives the top position during one oscillation, while the blue one illustrates the lowest position. To visualize the slope of the washboard potentials at each position, the derivatives are shown in the figure below, respectively. As a starting point, the particle sits in one of the deep minima where the derivative of the potential is positive, and $I = I_{dc} - I_{ac}$. For the sake of simplicity, let us consider a single period of oscillation. During the oscillation,

the slope changes, and the particle slides down until the slope of the potential is positive again[1]. As shown in figure 6.2.1(a, c), the slope does not reach a positive value at the position $\Delta\varphi = 2\pi$ for a low power. Thus, the particle falls down to the minimum at $\Delta\varphi = 4\pi$, and $\Delta\varphi/\Delta t = 4\pi f$. Consequently, steps of constant voltages appear at $V_n = nhf/2e$ with $n = 0, 2, 4, ...$, and the 4π-periodic contribution of the supercurrent is visible.

The amplitude of the oscillation is stronger for a high power as illustrated in figure 6.2.1(b, d). Thus, the slope at the position $\Delta\varphi = 2\pi$ becomes positive. The particle stops, and $\Delta\varphi/\Delta t = 2\pi f$. Shapiro steps appear at the regular values $V_n = nhf/2e$ with $n = 0, 1, 2, ...$ and the 4π-periodic contribution of the supercurrent is hidden.

Furthermore, the experimental data show that missing odd steps are preferably achieved below a certain driving frequency. To understand this within the RSJ model, we rewrite equation (6.2.1) to

$$\tau\frac{\partial\varphi}{\partial t} = i_{dc} + i_{ac}\cos(\omega_{ac}t) - i_{2\pi}\sin(\varphi) - i_{4\pi}\sin(\varphi/2) \tag{6.2.3}$$

where $\tau = \hbar/2eR_NI_C$ is the phase relaxation time, and each current i_x is given by its ratio of the critical current $i_x = I_x/I_C$. Firstly, we assume a pure 2π-periodic current-phase relation. Here, the phase relaxation time sets the time scale for the phase to adapt to a change of the current. When the oscillation period $1/\omega_{ac} > \tau$, the junction has enough time to relax during one oscillation. In this regime, we are able to observe Shapiro steps. For $1/\omega_{ac} < \tau$, the phase cannot follow the driving current. Therefore, the phase locking is not possible and Shapiro steps are absent. In our case, regarding a 2π-periodic and a 4π-periodic current contribution, the situation is more complicated. For each component there exists an own relaxation time $\tau_{2\pi} = \hbar/2eRI_{2\pi}$ and $\tau_{4\pi} = \hbar/eRI_{4\pi}$. However, the argumentation is similar as above. The 4π-periodic contribution influences the junction dynamics only for frequencies $\omega_{ac} < 1/\tau_{4\pi}$, while for $1/\tau_{2\pi} > \omega_{ac} > 1/\tau_{4\pi}$ the regular 2π-periodic dynamics dominate [146]. Hence, we are only able to observe missing odd Shapiro steps as a signature of 4π-periodic junction dynamics below a transition frequency $f_{4\pi}$ which is given by [39]

$$f_{4\pi} = \frac{\omega_{4\pi}}{2\pi} = \frac{1}{2\pi\tau_{4\pi}} = \frac{eR_NI_{4\pi}}{h}. \tag{6.2.4}$$

This equation gives us the opportunity to extract the 4π-periodic current $I_{4\pi}$ from frequency-dependent Shapiro step measurements.

With these results, we follow reference [33] to evaluate $f_{4\pi}$ from our experimental data. Figure 6.2(d, e) shows the histograms' power dependency of the above figure 6.2(a,b), respectively, at fixed voltages $V_n = nhf/2e$ for $n = 0, 1, 2$. This presentation

[1]Here, we assume that the frequency of the microwave radiation is in the right range to observe this behavior. The role of frequency is discussed later.

corresponds to slices in figure 6.2(a, b) at the fixed voltages. We extract the maximum step size (bin count) of the first step w_1 and the second one w_2. Figure 6.2(f) shows the ratio w_1/w_2 as a function of the microwave frequency f. A missing first step, i.e. a ratio $w_1/w_2 \ll 1$, indicates a 4π-periodic contribution to the supercurrent. This holds for frequencies below 5 GHz where the ratio w_1/w_2 is almost constant. For higher frequencies, the ratio w_1/w_2 rises. When $w_1/w_2 > 1$, all Shapiro steps are visible and the influence of the 4π-periodic contribution is suppressed. Thus, the frequency $f_{4\pi} \approx 5.9\,\mathrm{GHz}$, at which $w_1/w_2 = 1$ holds, is an estimation for the transition frequency $f_{4\pi}$. The error $\Delta f_{4\pi}$ describes the uncertainty of $f_{4\pi}$. It is given by the distance to adjacent frequencies for which a measurement is taken. With equation (6.2.4), we calculate the amplitude of the 4π-periodic supercurrent given by $I_{4\pi} = \frac{f_{4\pi}h}{2eR_N} \approx 57\,\mathrm{nA}$ where $R_N = 214\,\Omega$ is the normal-state resistance. This corresponds to $I_{4\pi}/I_C \approx 6\,\%$.

All in all, the RSJ model can explain the frequency- and power-dependence of the first and second Shapiro steps in the presence of a 2π- and 4π-periodic component of the supercurrent. Furthermore, it gives a first approximation for the ratio of the 4π-periodic current $I_{4\pi}$ to the total critical current I_C.

However, the arguments adapted from the RSJ model should also hold for steps with higher indices. Thus, all odd steps should be present or not. By looking at the experimental data, this is obviously not the case since odd steps at lower voltages are absent, while odd steps are still present at higher voltages. This is an indication that the RSJ model does not give an answer to all the phenomena observed in the experiment. Consequently, we also address the effects of the capacitance, Joule heating, and the excess current and discuss how they influence the observation of Shapiro steps.

6.2.2 Correction due to the excess current

By estimating the 4π-periodic current $I_{4\pi}$ with equation (6.2.4), we use the normal-state resistance $R_N = 1/G$. However, G only describes the conductance of the junction for voltages $V > 2\Delta/e$. Below this value, the conductance changes due to an excess current caused by presence of Andreev reflections. Since Shapiro steps usually occur at voltages $V_n \ll 2\Delta/e$, the usage of R_N for the calculation seems not to be ideal. To account for the excess current, an additional current source $I_{cor} = I_{exc} \tanh\left(V/V_{exc}\right)$ connected in parallel to the other circuit components of the model is considered. Thus, the current is given by [147]

$$I_{dc} = \frac{V}{R_N} + I_{cor} = \frac{V}{R_N} + I_{exc} \tanh\left(\frac{V}{V_{exc}}\right). \tag{6.2.5}$$

The excess voltage V_{exc} gives the voltage at which the current switches to the excess branch. I_{exc} is the magnitude of the excess current, i.e. the difference between the

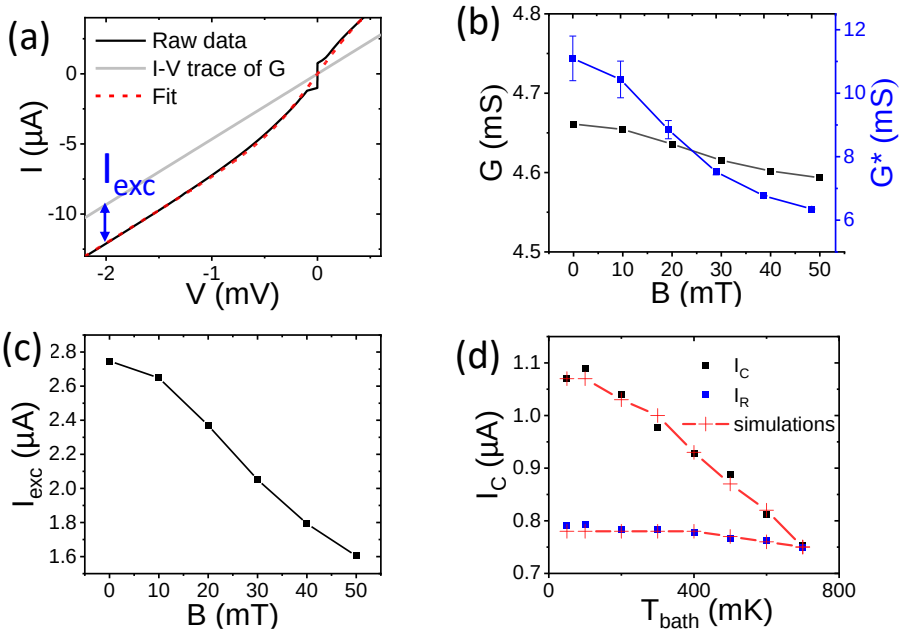

FIG. 6.4: (a) V-I curve of sample r1 at $B = 0$ up to high bias voltages. The fitting curve $I = VG + I_{exc} \tanh(V/V_{exc})$ perfectly reproduces the trace except for the zero-voltage plateau. (b) The conductances G and G^* as a function of the magnetic field B. While G^* has a strong dependence on the magnetic field, the normal-state conductance G hardly changes. (c) The excess current I_{exc} as a function of the magnetic field B. It is suppressed with increasing magnetic field from $B = 0$ to $B = 50\,\mathrm{mT}$ by a factor 0.57. (d) The critical current I_C and the retrapping current I_R as a function of the temperature T_{bath}. The red curve shows the simulated values from the extended RCSJ model with $Q = 2.1 \cdot 10^9\ eV/sK^5$.

measured value of the current at $V \gg V_{exc}$ and the expected ohmic value $GV = I_{dc}$. Figure 6.4 (a) illustrates a fit of equation (6.2.5) to the experimental V-I trace. It shows an excellent agreement for the values $R_N = 1/G = 214\,\Omega = 1/4.67\,\mathrm{mS}$, $I_{exc} = 2.75\,\mu\mathrm{A}$, and $V_{exc} = 0.48\,\mathrm{mV}$.

Hence, equation (6.2.5) produces a voltage-dependent effective conductance G^*. For $V \gg V_{exc}$, the effective conductance is $G^* = G$, while

$$G^* = G + \lim_{V \to 0} \frac{I_{cor}}{V} \tag{6.2.6}$$

holds for low voltages. Inserting the values obtained from the fit, we get $G^* = 4.67\,\mathrm{mS} + 5.7\,\mathrm{mS} = 10.4\,\mathrm{mS}$ for low voltages. As Shapiro steps appear in this low voltage regime, the use of the effective conductance G^* in an extended model is preferable.

So far, the data shown were conduced in the absence of a magnetic field. Since simulations should also be performed for a magnetic field applied along the wire,

we additionally extract the values for G, I_{exc}, V_{exc}, and G^* from the experimental data at different values of the magnetic field B. Figure 6.4(c) presents the excess current I_{exc} as a function of the magnetic field. The excess current is suppressed with increasing magnetic field from $B = 0$ to $B = 50\,\mathrm{mT}$ by a factor 0.57. From equation (4.2.2), we infer that the induced gap $\Delta_i(B)$ is suppressed by the same factor. The dependencies of G and G^* on the magnetic field B are shown in figure 6.4(b). G^* has a strong dependence on the magnetic field due to the dependence of I_{exc} on B, while G varies only by about 2 % between the lowest and the highest magnetic field values.

6.2.3 Influence of the capacitance

Within the RSJ model capacitive effects are neglected. To decide if the capacitance plays a role, we estimate the capacitance of our junctions, exemplarily shown for junction r1. Firstly, we treat the geometric capacitance. It is calculated by $C_{geo} = \epsilon_0 d_{SC} L_{SC}/L$ with the electric constant ϵ_0, the thickness of the superconducting leads $d_{SC} \approx 65\,\mathrm{nm}$, the distance between the leads $L \approx 170\,\mathrm{nm}$, and the length of the leads $L_{SC} \approx 20\,\mu\mathrm{m}$ at their closest distance. Here, we neglect the capacitance between other parts of the leads and the capacitance to the ground. Regarding only the closest part of the junction seems to be sufficient since $C \propto 1/L$. Hence, we obtain $C_{geo} \approx 68\,\mathrm{aF}$, and the Stuart-McCumber parameter is $\beta_C = 2eI_C C/\hbar(G^*)^2 \approx 4.5 \cdot 10^{-5} \ll 1$. Thus, the effect of the geometric capacitance is negligible.

However, the intrinsic capacitance of the junctions has also to be taken into account [148, 149]. The intrinsic capacitance arises due to quantum fluctuations and the resulting finite lifetime of the zero-voltage state. Using the washboard potential it can be explained as follows: A phase particle trapped in a minimum describes a metastable state since there is a finite probability for quantum-mechanically tunneling through the barrier. This phenomenon is called macroscopic quantum tunneling and is illustrated in the inset of figure 6.5(a). It is most prominent at low temperatures because thermally activated escaping as discussed in section 2.2.4 dominates for higher temperatures. Antonenko et al. [149] showed that the finite lifetime of the superconducting state results in an effective capacitance which is given by $C = \alpha\hbar G/E_g$. Here, α is a model-dependent parameter, G is the normal-state conductance, and E_g is the mini gap. The mini gap is $E_g = \Delta_i$ for short junctions, while $E_g = E_{Th}$ for long junctions. We consider two parallel contributions arising due to surface and bulk conduction. For our devices, the values α_{bulk} and α_{surf} are of the order of 1 while they generally depend on the phase φ [149]. The usage of this approximated value seems sufficient since a phase-dependent estimation would be excessive anyway. Thus, the intrinsic capacitance is given by

$$C_{int} = \alpha_{bulk}\frac{\hbar G^B}{E_{Th}^B} + \alpha_{surf}\frac{\hbar G^S}{\Delta_i} \approx 13\,\mathrm{fF} \tag{6.2.7}$$

with the conductance of the surface states $G^S = N_S D_{BPC} 2e^2/h \approx 0.9\,\mathrm{mS}$ and the conductance of the bulk states $G^B = (N - N_S)\, D_{BPC} 2e^2/h \approx 3.7\,\mathrm{mS}$. Consequently, the Stuart-McCumber parameter is $\beta_C \approx 0.4$. As the junction is only slightly overdamped, we conclude that the effects cannot be totally neglected in the Shapiro experiment. However, a large hysteresis in the I-V trace, e.g. observed in figure 4.3, is not expected as a consequence of the capacitance. Thus, we mainly ascribe the origin of the hysteresis to heating effects.
The Stuart-McCumber parameter increases with larger biases, but is reduced for higher magnetic fields as the critical current strongly decreases while the intrinsic capacitance and the conductance change weaker.

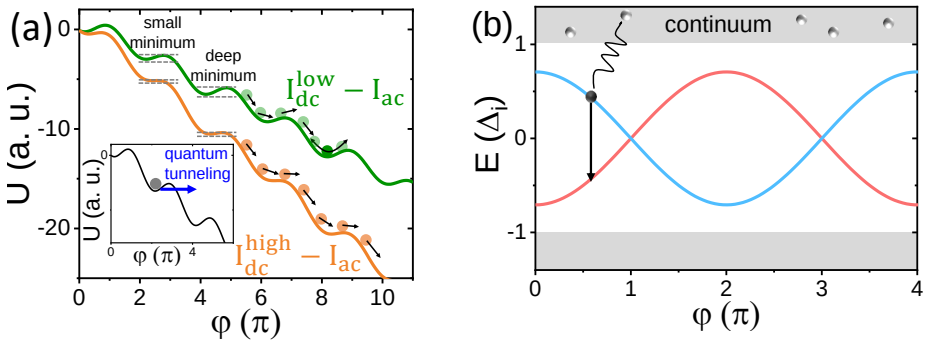

FIG. 6.5: (a) Washboard potential for $I_{dc}^{low} - I_{ac} = 0.5\, I_C$ and $I_{dc}^{high} - I_{ac} = 0.8\, I_C$ with $I_{4\pi} = 0.1\, I_C$ and $I_{2\pi} = 0.9\, I_C$. The phase particle is trapped in a minimum for both scenarios. For the low bias I_{dc}^{low}, the phase particle can possibly overcome the weak minimum when capacitive effects are considered. For a high bias I_{dc}^{high}, the phase particle is either trapped or can escape both types of minima. The inset illustrates the process of macroscopic quantum tunneling: A trapped phase particle has a finite probability for tunneling through the barrier. (b) Schematic sketch of quasiparticle poisoning. An excited bound state can relax to a lower energy state by accepting or giving a quasiparticle to the continuum. This process changes the measurable periodicity of the bound state. Adapted from [146].

As the capacitance of our junctions is not totally negligible, we discuss the consequences for the experiments. Picò-Cortés et al. [144] showed that the presence of a finite capacitance can explain the missing of the first Shapiro step only when both a 2π- and a 4π-periodic contribution of the supercurrent exist. For the explanation, we plot the washboard potential with a 2π- and a small 4π-periodic contribution for a low and a high bias current I_{dc} in figure 6.5(a) where the situation $I_{ext} = I_{dc} - I_{ac}$ for the same I_{ac} is shown, respectively. In the absence of a capacitance, the phase particle is trapped in a minimum for both I_{dc}. By considering the capacitance, the situation occur that the phase particle can overcome the weak minimum due to its inertia for a low bias I_{dc}^{low} (green trace), i.e. for a low Shapiro step index, while the barrier at a deep minimum is too high, and the particle is trapped. This scenario reveals the 4π-periodic contribution and leads to missing odd Shapiro steps. For a

high bias I_{dc}^{high} (orange trace), i.e. higher step indices, the situation is different. Here, the increased slope of the washboard potential results in a smaller difference between the depths of the minima. Thus, they are hardly distinguishable. A massive phase particle is either trapped or can escape both types of minima. In the first case, all Shapiro steps are observable, while no phase-locking occurs anymore in the latter case.

In addition to this explanation, there exists a suggestion that Joule heating is another cause explaining the absence of the first step only [146]. In the following, we discuss how heating influences our experiment.

6.2.4 Joule heating and quasiparticle poisoning

Our sample can be regarded as a thermodynamic system which is composed of two interacting subsystems, the electrons and the phonons. The electron and phonons are coupled together by the electron-phonon interaction. By applying an external current to the sample, the power P is added to the electron system. The electron temperature T rises and heat is transferred to the phonons until a steady-state condition is achieved [150]. We consider Joule heating by equating the average output power of the junction

$$\langle P\left(t\right)\rangle = \langle I(t)V(t)\rangle = \langle\left(I_{dc} + I_{ac}\sin\left(\omega_{ac}t\right)\right)V\left(t\right)\rangle \tag{6.2.8}$$

and the power dissipated through electron-phonon coupling

$$\langle P_{e-ph}\left(t\right)\rangle = Q\left(T^5 - T_{ph}^5\right) \tag{6.2.9}$$

where Q is a conversion constant describing electron-phonon coupling and T_{ph} is the phonon temperature. We assume that a device resting on a substrate has a constant phonon temperature $T_{ph} \approx T_{bath}$. Comparing both equations (6.2.8) and (6.2.9), gives the quasiparticle temperature T for each applied (I_{dc}, I_{ac}) [146, 151, 152]. The conversion constant Q can be calculated using microscopic parameters of the junction [153–155]. However, we can also extract Q from the experimental data. This will be shown below.

Beforehand, we explain how the Shapiro steps are affected by the heating. For the sake of simplicity, we use the RSJ model and set $I_{2\pi} = I_C$, $I_{4\pi} = 0$. The average heating power, using the second Josephson equation (2.2.24) and $I = I_{dc} + I_{ac}\sin(2\pi ft)$, is given by

$$\langle P\left(t\right)\rangle = \langle\left(I_{dc} + I_{ac}\sin\left(2\pi ft\right)\right)\frac{\hbar}{2e}\frac{\partial\varphi}{\partial t}\rangle. \tag{6.2.10}$$

By plugging in $\partial\varphi/\partial t$ from equation (6.2.1)[2], we obtain[3]

$$\begin{aligned}\langle P(t)\rangle &= \langle R_N \left(I_{dc} + I_{ac}\sin(2\pi f t)\right)\left(I_{dc} + I_{ac}\sin(2\pi f t) - I_C\sin(\varphi)\right)\rangle \\ &= R_N\left[I_{dc}^2 + I_{ac}^2/2 - I_{ac}\langle\sin(2\pi f t)\cdot\sin(\varphi)\rangle\right].\end{aligned} \tag{6.2.11}$$

If Shapiro steps appear, the phase is locked at a multiple n of the frequency. Hence, the phase is given by $\varphi = n2\pi f t$ (see equation (2.2.32)). In that case, the heating power yields[4]

$$\langle P(t)\rangle = R_N\left[I_{dc}^2 + I_{ac}^2/2 - I_{ac}\delta_{n,1}/2\right] \tag{6.2.12}$$

with the Kronecker delta $\delta_{n,m}$. This equation shows that the plateau $n = 1$ is less heated than the other Shapiro steps due to the additional summand. Additionally, the heating power increases for higher indices as the steps appear at a larger bias I_{dc} [146, 151].

To understand how heating suppresses the observation of missing odd steps we introduce the mechanism of quasiparticle poisoning: An excited bound state can relax to a lower energy state by accepting or giving a quasiparticle to the continuum. Figure 6.5(b) illustrates this process for a 4π-periodic bound state. Here, one state, say the blue trace, is half of the time at a higher energy than the other one (red trace). Thus, the ground state is not always the same state. When the system is in the state with higher energy, it is excited. Now, quasiparticle poisoning can switch the system to its ground state as indicated by the black arrow. If a switching event occurs when the curve is traversed, the resulting energy-phase relationship is 2π-periodic. Hence, to keep the 4π-periodicity, the measurement time has to be shorter than the quasiparticle lifetime τ_{sw} of the 4π-periodic state which is given by

$$\tau_{sw} = \tau_0 \mathrm{e}^{\frac{\Delta_i - E}{k_B T}} \tag{6.2.13}$$

with a phenomenological time scale τ_0 [151]. Therefore, it is most promising to check the periodicity by the ac Josephson effect.

From equation (6.2.13), we notice that an increased electronic temperature promotes quasiparticle poisoning and, thus, reduces the lifetime τ_{sw} of the 4π-periodic state. Since the electronic temperature T increases for Shapiro steps with higher indices, poisoning is enhanced, and the reveal of the 4π-periodicity is suppressed. Accordingly, missing odd steps are more likely to occur for a low step index n, especially for $n = 1$ [151].

[2] The external ac current is given by $I_{ac}\cos(\omega_{ac}t)$ in equation (6.2.1), while we use $I_{ac}\sin(\omega_{ac}t)$ at this point following the cited literature, respectively. This does not change any physics.

[3] $\langle\sin^2(2\pi f t)\rangle = 1/2$, $\langle\sin(2\pi f t)\rangle = 0$, and $\langle\sin(\varphi)\rangle = 0$.

[4] $\langle\sin(2\pi f t)\cdot\sin(\varphi)\rangle = \frac{1}{1/f}\int_0^{1/f}\sin(2\pi f t)\cdot\sin(2\pi n f t)\,dt = \frac{\sin(2\pi n)}{2\pi(n^2-1)}$. The result is 0 for every n, except $n = 1$. Here, $\lim_{n\to 1}\frac{\sin(2\pi n)}{2\pi(n^2-1)} = \frac{1}{2}$.

6.2.5 The extended RCSJ model

Since we discussed several issues, which are not covered by the RSJ model, we extend the model by considering the capacitance, Joule heating, and the excess current. Here, we limit the discussion to the physical basics. The associated numerical simulations were performed by J. Picò-Cortés [156].

The differential equation of the extended RCSJ model is given by

$$\frac{\hbar C(T)}{2e}\frac{\partial^2\varphi}{\partial t^2}+\frac{\hbar G}{2e}\frac{\partial\varphi}{\partial t}+I_S(\varphi,\ T)+I_{cor}\frac{\hbar}{2e}\frac{\partial\varphi}{\partial t}=I_{dc}+I_{ac}\sin(\omega_{ac}t)+I_n(t,\ T) \quad (6.2.14)$$

where φ is the phase difference between the two superconductors, T is the quasiparticle temperature, C is the effective capacitance of the junction, G is the normal-state conductance, I_{dc} and I_{ac} are the dc- and ac-current amplitudes, and ω_{ac} is the ac bias frequency. The effect of excess currents is introduced by adding an effective current element I_{cor} which introduces a voltage-dependent conductance. A Gaussian white noise term $I_n(t,T)$ with the autocorrelation function $\langle I_n(t_1)I_n(t_2)\rangle = 2k_BTG(T)u(t_1-t_2)$, where $u(t)$ is an unit impulse function, describes statistical noise. The supercurrent term $I_S(\varphi,\ T)$ is assumed to have the form

$$I_S(\varphi,\ T)=I_{2\pi}\mathrm{f}^{2\pi}(\varphi,\ T)+I_{4\pi}\mathrm{f}^{4\pi}(\varphi,\ T) \quad (6.2.15)$$

with $\mathrm{f}^{2\pi}(\varphi,\ T)=\mathrm{f}^{2\pi}(\varphi+2\pi,\ T)$ and $\mathrm{f}^{4\pi}(\varphi,\ T)=\mathrm{f}^{4\pi}(\varphi+4\pi,\ T)$. The functions $\mathrm{f}^{k}(\varphi,\ T)$ are normalized that $\max_\varphi\left[\mathrm{f}^{k}(\varphi,\ 0)\right]=1$. For the 2π-periodic part of the current-phase relation we consider the bulk as well as the surface contribution

$$\mathrm{f}^{2\pi}=\frac{1}{N^{2\pi}}\left(\frac{I_C^{Bulk}}{I_C^{Bulk}+I_C^{Surf}}\mathrm{f}^{2\pi}_{Bulk}(\varphi,\ T)+\frac{I_C^{Surf}}{I_C^{Bulk}+I_C^{Surf}}\mathrm{f}^{2\pi}_{Surf}(\varphi,\ T)\right) \quad (6.2.16)$$

where $N_{2\pi}$ is a normalization constant to ensure $\max_\varphi\left[\mathrm{f}^{2\pi}(\varphi,\ 0)\right]=1$. For the surface contributions, we apply the temperature-dependent results of section 2.3.4 for a short junction[5]. Thus, the 2π- and 4π- current-phase relations yield

$$\mathrm{f}^{2\pi}_{Surf}(\varphi,\ T)=\frac{1}{N^{2\pi}_{Surf}}\frac{\Delta_i(T)}{\Delta_i(0)}\frac{\sin(\varphi)}{\sqrt{1-D_{BPC}\sin^2(\varphi/2)}}\tanh\left(\frac{\Delta_i(T)}{2k_BT}\right), \quad (6.2.17)$$

$$\mathrm{f}^{4\pi}_{Surf}(\varphi,\ T)=\frac{\Delta_i(T)}{\Delta_i(0)}\sin\left(\frac{\varphi}{2}\right)\tanh\left(\frac{\Delta_i(T)\sqrt{D_{BPC}}}{2k_BT}\right) \quad (6.2.18)$$

where D_{BPC} is the average transmission and $N^{2\pi}_{Surf}$ is a normalization constant.

[5] Compared to the result of section 2.3.4, $\tanh\left(\Delta_i\sqrt{D_{BPC}}\cos(\varphi/2)/2k_BT\right)$ is simplified to $\tanh\left(\Delta_i\sqrt{D_{BPC}}/2k_BT\right)$. This is valid assuming that the occupation numbers of the subgap states instantaneously are in thermal equilibrium for each φ [27, 28]. Additionally, we explicitly use the induced gap Δ_i.

For the bulk part, we consider the current-phase relation of a long, clean junction. It is obtained from solving the Eilenberger equations with rigid boundary conditions (see [156, 157] for details).

Finally, the conversion constant Q has to be determined in order to estimate the quasiparticle temperature T for each (I_{dc}, I_{ac}). For that, the temperature dependence of the critical current I_C and the retrappping current I_R is reproduced within the extended RCSJ model for $I_{ac} = 0$. The experimental data of I_C (black dots) and I_R (blue dots) as a function of the bath temperature T_{bath} are plotted in figure 6.4 (d). The red lines illustrate the results of the simulations for $Q = 2.1 \cdot 10^9\ eV/sK^5$. Since the simulations fit almost perfectly the experimental results, this value is chosen for further simulations.

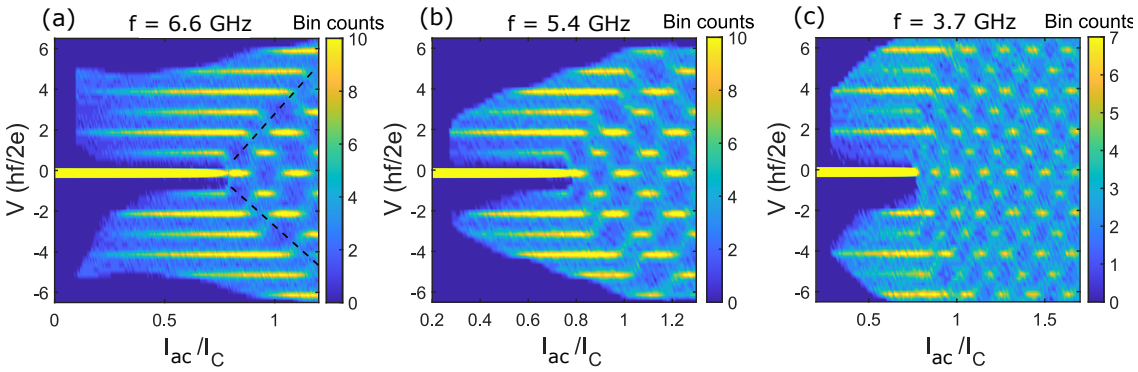

FIG. 6.6: Frequency dependence of Shapiro steps at $B = 0\,\mathrm{mT}$. (a-c) Color maps obtained from numerical simulations for frequencies $f = 6.6\,\mathrm{GHz}$, $5.4\,\mathrm{GHz}$, and $3.7\,\mathrm{GHz}$ using the extended RCSJ model. The corresponding experimental data are shown in figure 6.2(a-c). The simulations match the experimental results best for $I_{4\pi}/I_C \approx 0.06$. The simulations were performed by J. Picò-Cortés.

As now all parameters of the RCSJ model are clarified, I-V traces in the presence of microwave radiation were simulated. The bin maps are created analogously to the experimental approach. The results of the simulations for frequencies $f = 6.6\,\mathrm{GHz}$, $f = 5.4\,\mathrm{GHz}$, and $f = 3.7\,\mathrm{GHz}$ are presented in figure 6.6. These are the frequencies for which the corresponding experimental data are shown in figure 6.2. Note that the Shapiro profiles are represented in terms of the amplitude of the ac bias I_{ac} in the simulations, while the experimental results are represented in terms of the microwave power $P \propto I_{ac}^2$. Minor deviations in the x-axis scaling of experiment and simulation occur since the exact relation between P and I_{ac} is unknown. By choosing $I_{4\pi}/I_C = 6.1\,\%$, the simulations show a great agreement with the experimental data. One discrepancy is that the first step is less quenched at high frequencies in the experiment compared to the calculations. Likewise, frequency-dependent damping [158] being stronger at higher frequencies could explain this feature. A stronger damping, i.e. a smaller β_C, would mask the presence of 4π-periodic current.

Alternatively, the difference could originate from the temperature dependence of the conductance at low bias or the phase dependence of the effective capacitance which both are not captured by the model. Accordingly, we prioritize reproducing the lowest frequency results when a single match for all frequencies is not possible.

6.3 Trivial origin of 4π-periodic supercurrents: Landau-Zener transitions

The observation of a 4π-periodic supercurrent at $B = 0$ is surprising as the subband structure of the wire is topologically trivial. However, it is conceivable that Landau-Zener transitions between trivial Andreev bound states with a small gap mimic 4π periodicity [40]. The principle of Landau-Zener transition is illustrated in figure 6.7(a). Here, transitions from the lower bound state to the higher one or vice versa take place. The transitions are indicated by black arrows. This process has the highest probability to occur at the anticrossings of the two states at $\varphi = (2n + 1)\,\pi$ where $n \in \mathbb{Z}$. Consequently, the effective energy-phase relation in the presence of Landau-Zener transitions is 4π-periodic as sketched by the green dashed line in figure 6.7(a). Furthermore, the corresponding current-phase relation is plotted in figure 6.7(b). The black dashed line shows the current-phase relation of the Andreev bound state, while the blue trace illustrates the current-phase relation in the presence of Landau-Zener transitions. The latter is 4π-periodic. Hence, missing odd steps are expected by probing the fractional Josephson effect even if only 2π-periodic Andreev bound states are present.

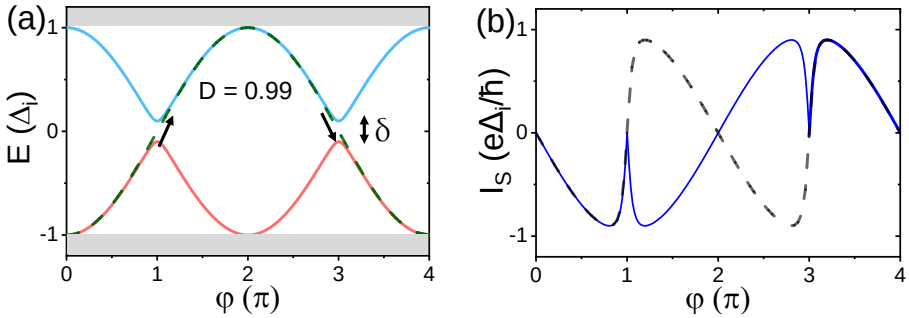

FIG. 6.7: (a) Illustration of Landau-Zener transitions exemplarily shown between trivial Andreev bound states (solid lines) with a transmission $D = 0.99$. At the anticrossings of the upper and the lower bound state, a transition between the states can take place. This is indicated by the black arrows. This process can mimic a 4π-periodicity of the energy-phase relation as illustrated by the dashed line. (b) The resulting current-phase relation in the presence of Landau-Zener transitions (blue line) is 4π-periodic. The dashed line shows the current-phase relation when no Landau-Zener transitions occur. Adapted from [145].

The probability of a Landau-Zener transition at $\varphi = \pi$ is given by [40, 122]

$$P_{LZT} = \mathrm{e}^{-2\pi\delta^2/(\Delta_i \hbar \frac{d\varphi}{dt}|_{\varphi=\pi})} = \mathrm{e}^{-\pi\Delta_i(1-D)/(e|V(t_{LZT})|)} \tag{6.3.1}$$

where $2\delta = 2\Delta_i\sqrt{1-D}$ is the gap between the Andreev bound states and $V(t_{LZT}) = (\hbar/2e)d\varphi/dt|_{\varphi=\pi}$ is the voltage across the junction when the system goes across the anticrossing. Thus, a high transmission D favors Landau-Zener transitions since the probability decays exponentially with the size of the gap δ. In addition, the probability increases at higher bias voltages V. Since this is contrary to the experimental observation, where the missing steps are predominantly appear at low voltages, i.e. low frequencies, Landau-Zener transitions were ruled out to be origin of the missing steps in previous works [33, 146]. However, this argumentation only holds for a single channel while many channels with various transmissions co-exist in a real system. Indeed, a recent work refutes the original argumentation and shows that Landau-Zener transitions can cause a 4π periodicity in a trivial material [40]. In their model, the supercurrent can flow across the junction via two effective modes which represent the many modes in a simplified way. One mode has a very low transmission and a negligible probability to undergo a Landau-Zener transition. The other one has a very high transmission and favors Landau-Zener transitions. For a low current bias, i.e. a low average voltage, the current is predominantly carried by the channel with high transmission. Thus, Landau-Zener transitions occur and a 4π periodicity is mimicked. When the bias current is increased, more and more of the current is carried by the channel with a negligible probability of Landau-Zener transitions showing the 2π periodicity. For the appearance of missing Shapiro steps in a trivial material, the results imply that only a few modes with high transmission besides many modes with low transmission are sufficient to observe missing odd steps. As long as the bias, i.e. the frequency, is low enough that most of the current flows via the channel with high transmission, missing odd steps occur. When the current in the channel with low transmission becomes larger, the odd Shapiro steps reappear [40]. Therefore, these considerations show that the observation of a 4π-periodic Josephson current is a necessary but not sufficient proof of topological superconductivity and the presence of a Majorana bound state [159].

In our device, it is quite reasonable that there are a few modes with very high transmission and many modes with poorer transmission resulting in an average transmission as calculated in section 4.2. With this assumption, we can ascribe the 4π-periodic supercurrent at $B = 0$ in our experiment to Landau-Zener transitions between trivial Andreev bound states with a small gap.

6.4 Magnetic field dependence of the 4π-periodic supercurrent

In the following, we show data as a function of magnetic flux where the system is expected to change from trivial to topological.

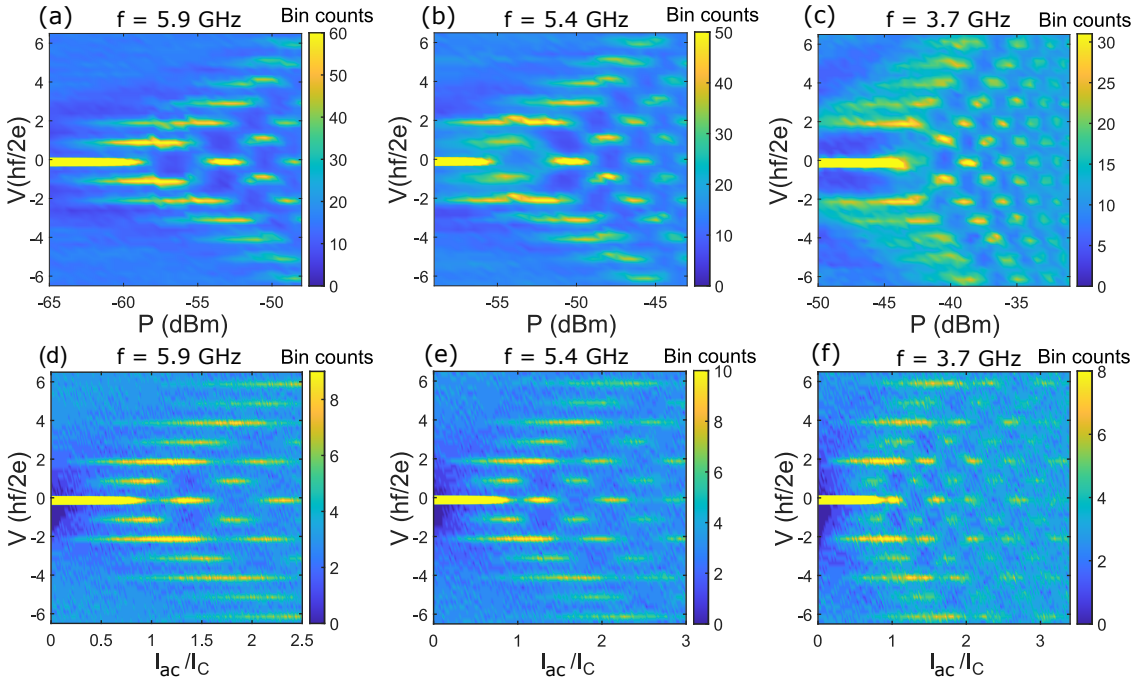

FIG. 6.8: Frequency dependence of Shapiro steps at $B = 30\,\mathrm{mT}$ ($\Phi/\Phi_0 \approx 0.27$) (a-c) Color maps of the bin counts of sample r1 at frequencies $f = 5.9\,\mathrm{GHz}$, $5.4\,\mathrm{GHz}$, and $3.7\,\mathrm{GHz}$. The transition frequency is $f_{4\pi} = 5.6\,\mathrm{GHz}$. With $R_N = 216\,\Omega$, we estimate $I_{4\pi}/I_C \approx 0.21$ using the RSJ model. (d-f) Numerical simulations using the extended RCSJ model. The model almost perfectly fits the experiment by using $I_{4\pi}/I_C \approx 0.15$. The simulations were performed by J. Picò-Cortés.

Figure 6.8(a-c) shows the data of sample r1 measured at $B = 30\,\mathrm{mT}$ where the magnetic field B is aligned along the wire axis as sketched in figure 6.1(a). This value corresponds to a magnetic flux $\Phi = BA \approx 0.27\,\Phi_0$. The first Shapiro steps, fully present at 5.9 GHz, are weakened at 5.4 GHz and are fully absent at 3.7 GHz. Analogous to section 6.3, we extract the transition frequency $f_{4\pi} = 5.6\,\mathrm{GHz}$. Consequently, we obtain $I_{4\pi} = \frac{f_{4\pi}h}{2eR_N} \approx 55\,\mathrm{nA}$ using equation (6.2.4). Thus, the 4π-periodic current is slightly smaller than without a magnetic field. However, as the total critical current I_C decreases strongly with B to $I_C\,(30\,\mathrm{mT}) = 260\,\mathrm{nA}$, a larger fraction of the 4π-periodic current $I_{4\pi}/I_C = 0.21$ is carried by the 4π-periodic contribution. Figures 6.8(d-f) show corresponding simulations within the extended RCSJ model. Here, the experimental data are most accurately reproduced using a fraction of the 4π-periodic

current $I_{4\pi}/I_C = 0.15$. As the simulations also give satisfying results for a certain range around this value, which is $I_{4\pi}/I_C = 0.14 - 0.18$, there is some uncertainty of this value. The determination of the range and the influence of different 4π-periodic contributions on the results is summarized in [155, 156].

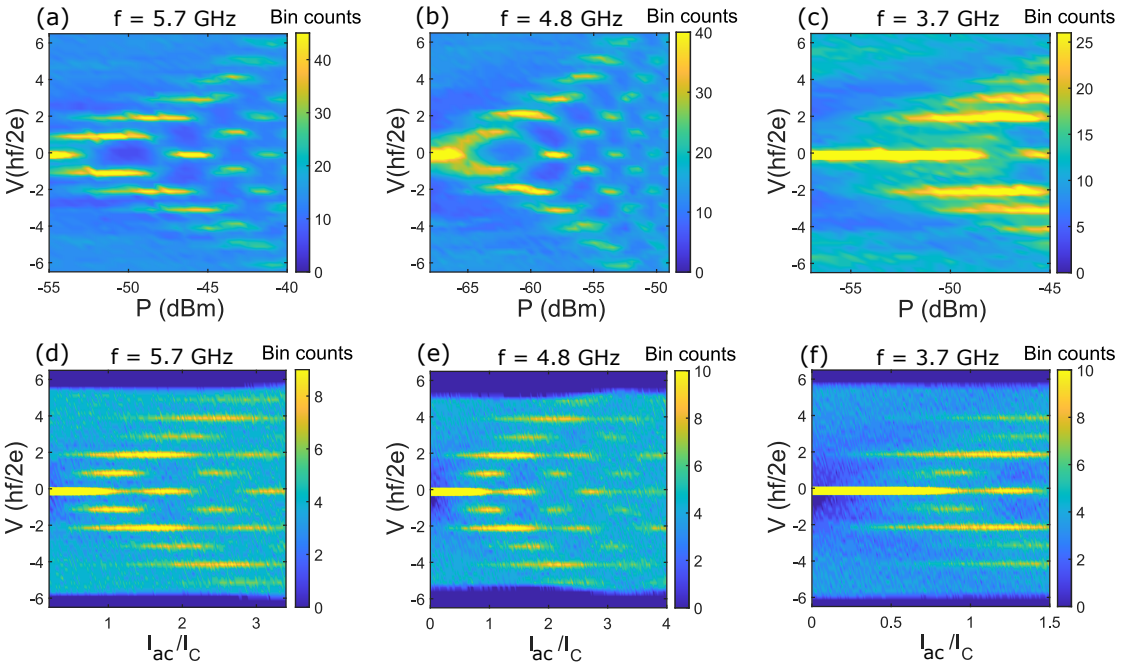

FIG. 6.9: Frequency dependence of Shapiro steps at $B = 40\,\mathrm{mT}$ ($\Phi/\Phi_0 \approx 0.36$) (a-c) Color maps of the bin counts of sample r1 at frequencies $f = 5.7\,\mathrm{GHz}$, $4.8\,\mathrm{GHz}$, and $3.7\,\mathrm{GHz}$. The transition frequency is $f_{4\pi} = 4.9\,\mathrm{GHz}$. With $R_N = 217\,\Omega$, we estimate $I_{4\pi}/I_C \approx 0.31$ using the RSJ model. (d-f) Numerical simulations using the extended RCSJ model. The simulations reproduce the experimental results most accurately for $I_{4\pi}/I_C \approx 0.20$. The simulations were performed by J. Picò-Cortés.

Figure 6.9(a-c) shows the color maps at $B = 40\,\mathrm{mT}$. This value corresponds to a magnetic flux $\Phi = BA \approx 0.36\,\Phi_0$. The first Shapiro steps are fully visible at 5.7 GHz. At $f = 5.4\,\mathrm{GHz}$, they are decreased to approximately half width, while they are almost fully disappeared at 3.7 GHz. Here, the transition frequency is $f_{4\pi} = 4.9\,\mathrm{GHz}$. Thus, we get $I_{4\pi} = \frac{f_{4\pi}h}{2eR_N} \approx 48\,\mathrm{nA}$ using the RSJ model. Since the total critical current is reduced to $I_C\,(40\,\mathrm{mT}) = 155\,\mathrm{nA}$, $I_{4\pi}/I_C = 0.31$. The corresponding simulations using the extended RCSJ model are presented in figure 6.9(d-f). Simulated and experimental data show the best agreement for $I_{4\pi}/I_C = 0.2$. Although the absolute values of $I_{4\pi}/I_C$ depends on the respective model, both models capture an increase of the 4π-periodic current up to $B \approx 40\,\mathrm{mT}$.

At last, we present color maps at $B = 55\,\mathrm{mT}$, which correspond to $\Phi = BA \approx 0.5\,\Phi_0$, in figure 6.10(a-c). By lowering the frequency from $f = 3.7\,\mathrm{GHz}$ across 3.4 GHz to

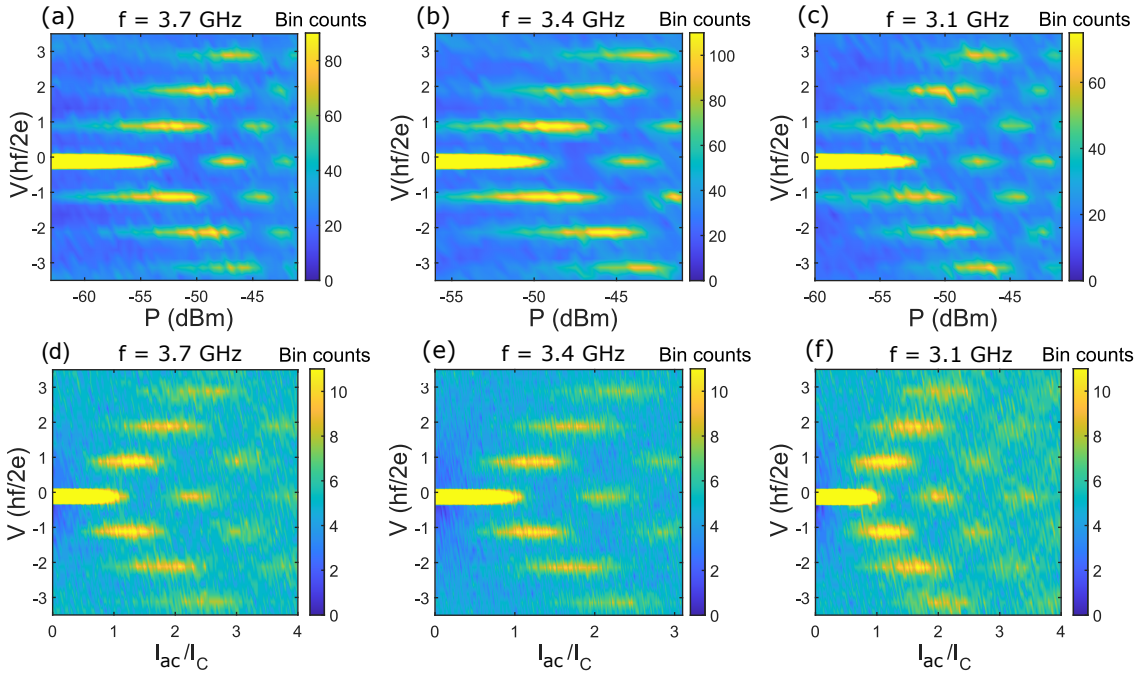

FIG. 6.10: Frequency dependence of Shapiro steps at $B = 55\,\mathrm{mT}$ ($\Phi/\Phi_0 \approx 0.5$). (a-c) Color maps of the bin counts of sample r1 at frequencies $f = 3.7\,\mathrm{GHz}$, $3.4\,\mathrm{GHz}$, and $3.1\,\mathrm{GHz}$. The transition frequency is $f_{4\pi} = 3.2\,\mathrm{GHz}$. With $R_N = 217\,\Omega$, we estimate $I_{4\pi}/I_C \approx 0.43$ using the RSJ model. (d-f) Numerical simulations using the extended RCSJ model. The simulations reproduce the experimental results most accurately for $I_{4\pi}/I_C \approx 0.09$. The simulations were performed by J. Picò-Cortés.

$f = 3.1\,\mathrm{GHz}$, only a tiny reduction in the width of the first step is detectable. Indeed, a detailed analysis of the step widths suggests that the width of the second step is larger than the width of the first one at $f = 3.1\,\mathrm{GHz}$. The evaluation leads to $f_{4\pi} = 3.2\,\mathrm{GHz}$, $I_{4\pi} = \frac{f_{4\pi}h}{2eR_N} \approx 31\,\mathrm{nA}$, and $I_{4\pi}/I_C = 0.43$ using the RSJ model. As the critical current is significantly reduced for such high magnetic fields, the resistive and capacitive contributions gain in importance. The effect of the 4π-periodic supercurrent is harder to observe in this regime. Compared to lower magnetic fields, much lower frequencies are required to observe completely missing Shapiro steps. Hence, a clearer reduction of the first step would probably be observable at lower frequencies. Unfortunately, useful measurements could not be obtained due to limited resolution of the Shapiro steps. For that reason, the estimation of $I_{4\pi}$ is less precise than for lower magnetic fields. Figures 6.10(d-f) illustrate the corresponding simulations within the extended RCSJ model. The experimental data are most accurately reproduced using $I_{4\pi}/I_C = 0.09$. Since there is no experimental data as a template, in which a fully missing first step is present, the determination of $I_{4\pi}/I_C$ is also less accurate, and satisfying results can be obtained for a large range of $I_{4\pi}/I_C = 0 - 0.16$. By comparing the results of the RSJ and the extended

RCSJ model for $B = 55\,\mathrm{mT}$, we notice clear differences: While the RSJ model predicts a higher fraction $I_{4\pi}/I_C$ at $B = 55\,\mathrm{mT}$ than for lower magnetic fields, the results of the extended RCSJ model suggest that $I_{4\pi}/I_C$ is reduced again compared to $B = 40\,\mathrm{mT}$.

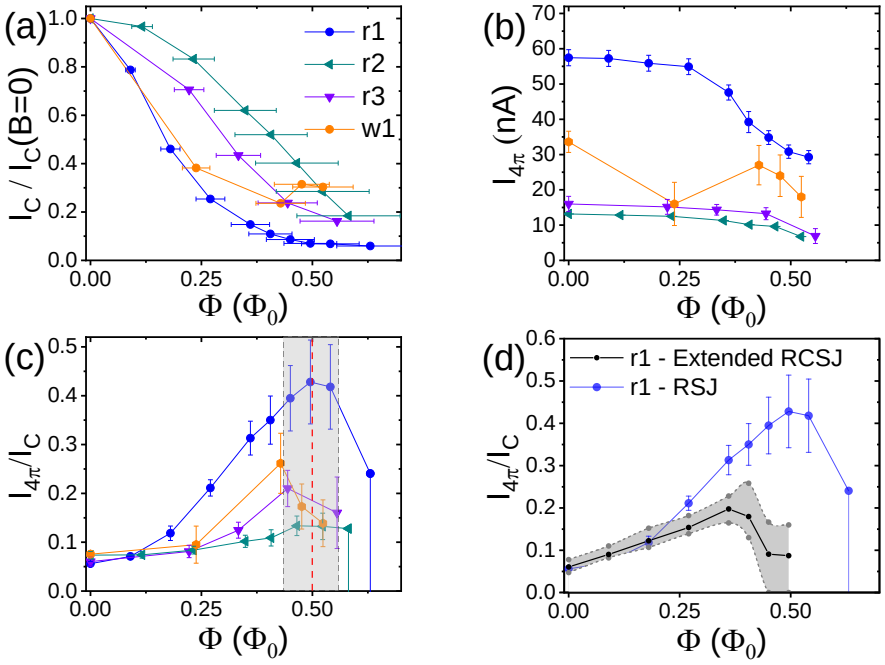

FIG. 6.11: Magnetic field dependence of the critical currents for samples r1, r2, r3, and w1. (a) The total critical current I_C normalized to its value at $B = 0$ for four wires plotted versus the magnetic field applied in parallel to the wire. The amplitude of I_C is strongly reduced by the magnetic field. (b) The 4π-periodic current $I_{4\pi}$, in contrast, decreases weaker as a function of magnetic flux. (c) The ratio $I_{4\pi}/I_C$ obtained using the RSJ model plotted as a function of the magnetic flux Φ. The red line marks $\Phi/\Phi_0 = 0.5$ while the grayish background indicates its uncertainty. All traces display maxima at about $\Phi/\Phi_0 \approx 0.5$. (d) Comparison of $I_{4\pi}/I_C$ of wire r1 extracted using the RSJ model and the extended RCSJ model. The black dots resemble the values for which the simulations fit the experimental data most accurately while ratios in the gray area also lead to satisfying results. The extended RCSJ model gives somewhat smaller values at high magnetic fields than the RSJ model, but also shows a distinct maximum which occurs at a lower field. However, the exact position of the maximum in the blue curve is difficult to determine due to the large error bars around $\Phi/\Phi_0 \approx 0.5$.

A detailed overview of the magnetic field dependence of I_C and $I_{4\pi}$ for sample r1 is displayed in figure 6.11 (blue traces). To be quantitative, we also add the results of three other samples r2, r3, and w1[6] with different geometries. Experimental datasets of samples r2 and r3 can be found in appendix B. Figure 6.11(a) illustrates the

[6]Sample 'w1' was fabricated and measured by W. Himmler.

critical current I_C normalized to its value at $B = 0$ as a function of the magnetic flux Φ. The critical current drops quickly with increasing Φ for all samples. The error bars on the Φ-axis indicate the uncertainty of determining the exact value of the magnetic flux since the width of the wire can only be roughly estimated (see section 4.2). Furthermore, there are also errors on the I_C-axis which are not shown in the figure. They arise since the exact value of I_C cannot be determined due to a finite size of the measurement interval between two points. The 4π-periodic current $I_{4\pi}$ calculated within the RSJ model as a function of the magnetic flux Φ is shown in figure 6.11(b). It decreases much less than I_C. The error bars have their origin in the uncertainty of the transition frequency $\Delta f_{4\pi}$. The magnetic field dependence of the ratio $I_{4\pi}/I_C$ is plotted in figure 6.11(c). For sample r1, $I_{4\pi}/I_C$ increases from about 0.06 at $B = 0$ to 0.43 at $B = 55\,\mathrm{mT}$ ($\Phi/\Phi_0 \approx 0.5$). We also performed measurements at $B = 70\,\mathrm{mT}$ ($\Phi/\Phi_0 \approx 0.63$). Here, we do not observe a missing first Shapiro step down to $f = 1.5\,\mathrm{GHz}$ which is the lowest frequency at which the first Shapiro steps get resolved. Thus, the blue point of wire r1 in figure 6.11(c) at $\Phi/\Phi_0 \approx 0.63$ can be regarded as an upper limit for $I_{4\pi}/I_C$. Assuming the odd Shapiro steps start to disappear just below $f = 1.5\,\mathrm{GHz}$, we use $f_{4\pi} = 1.5\,\mathrm{GHz}$ and get $I_{4\pi}/I_C \approx 0.24$. However, the value might be significantly lower as indicated by the large error bar. All in all, we observe an increase of $I_{4\pi}/I_C$ with Φ with a maximum close to $\Phi \approx 0.5\,\Phi_0$. We ascribe the increase to the additional occurrence of the topological mode around $\Phi \approx 0.5\,\Phi_0$ as predicted by the theory [23]. Upon further increase of B, we expect the perfectly transmitting state to disappear again and $I_{4\pi}/I_C$ to drop.

The wires r2, r3, and w1 show a similar dependence of $I_{4\pi}/I_C$ on the flux Φ although the peak height near $\Phi/\Phi_0 \approx 0.5$ varies strongly. This variation is most likely linked to the magnetic field dependence of the 2π-periodic current $I_{2\pi}$ which dominates the critical current I_C. The fact that $I_{4\pi}/I_C$ has a maximum sometimes slightly below $\Phi = \Phi_0/2$ is not surprising since the exact magnetic field range in which the perfectly transmitting mode occurs depends on many experimental parameters like the exact position of the Fermi level, disorder, or the shape of the nanowire [73]. Additionally, there is also some uncertainty of determining the exact value of the magnetic flux as discussed above. This error is indicated by the grayish background in figure 6.11(c).

In figure 6.11(d), we compare the results of sample r1 obtained from the RSJ and the extended RCSJ model. The blue dots show the results of the RSJ model, while the black dots resemble the values for which the simulations within the extended RCSJ model fit the experimental data most accurately. The ratios in the gray area also lead to satisfying results and can be regarded as error bars. The extended RCSJ model gives somewhat smaller values at high magnetic fields than the RSJ model, but also shows a distinct maximum which occurs at a lower field $B = 40 - 45\,\mathrm{mT}$. Despite this difference, both analysis methods show qualitative agreement, i.e. an increase

of $I_{4\pi}/I_C$ with increasing flux with a maximum near half flux quantum. Possibly, the positions of the maxima obtained from both methods could be closer together than assumed as the exact position of the maximum in the blue trace is hard to determine due to the large vertical error bars around $\Phi/\Phi_0 \approx 0.5$. Additionally, for the estimation of $f_{4\pi}$, the value $f\,(\mathrm{w}_1/\mathrm{w}_2 = 1)$ is used in the RSJ model. Since this definition of $f_{4\pi}$ does not necessarily describe exactly the beginning of the influence of the 4π-periodic component, a slightly different definition might also be conceivable. This would lead to different absolute values of $I_{4\pi}/I_C$.

6.5 Trivial vs. topological 4π-periodic supercurrents

So far, we assume that the 4π-periodic current at $B = 0$ is of trivial origin while at a finite range around $\Phi/\Phi_0 \approx 0.5$ (or a slightly smaller value than $\Phi/\Phi_0 \approx 0.5$) the perfectly transmitting mode appears adding an additional contribution to the 4π-periodic current. By further increasing Φ, the topological mode is expected to disappear again.

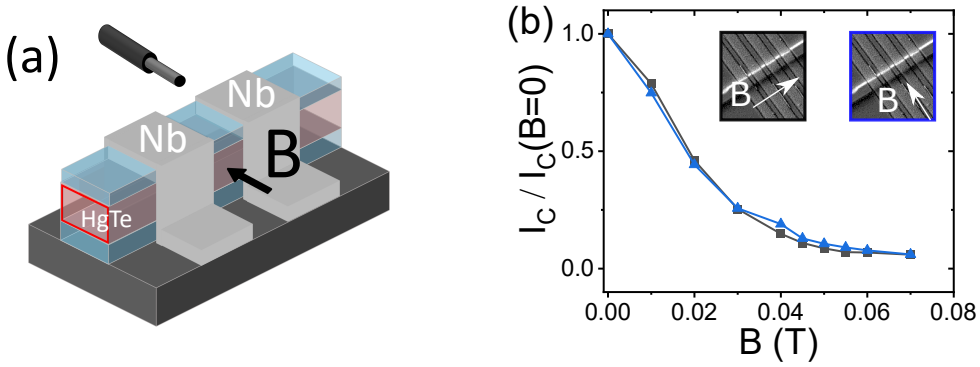

FIG. 6.12: (a) Sketch of the experimental setup. When the magnetic field B is aligned perpendicular to the wire, no transition from a trivial to a topologically nontrivial band structure occurs. (b) The total critical current I_C, normalized to its value at $B = 0$, plotted for the magnetic fields applied parallel to the wire (black) and perpendicular to the wire (blue). The orientation of B is visualized in the insets.

To verify our consideration, we have to disentangle the trivial and the topological 4π-periodic contribution to the supercurrent. This can be accomplished by experiments where the magnetic field is oriented perpendicular to the wire as sketched in figure 6.12(a). For this configuration, no transition from a trivial to a topologically nontrivial band structure is expected. Hence, missing Shapiro steps should exclusively arise due to trivial effects. In figure 6.12(b), the critical current I_C as a function of B aligned perpendicular to the wire (blue trace) is compared to I_C where the magnetic field B is orientated along the wire (black trace, same data as in figure 6.11 (a)). We

plot them as normalized values since the data were taken at different temperature cycles leading to small differences of about 7 % for I_C. For both orientations of the magnetic field, I_C decays quite similar. This allows us to directly compare the Shapiro maps at specific magnetic field values.

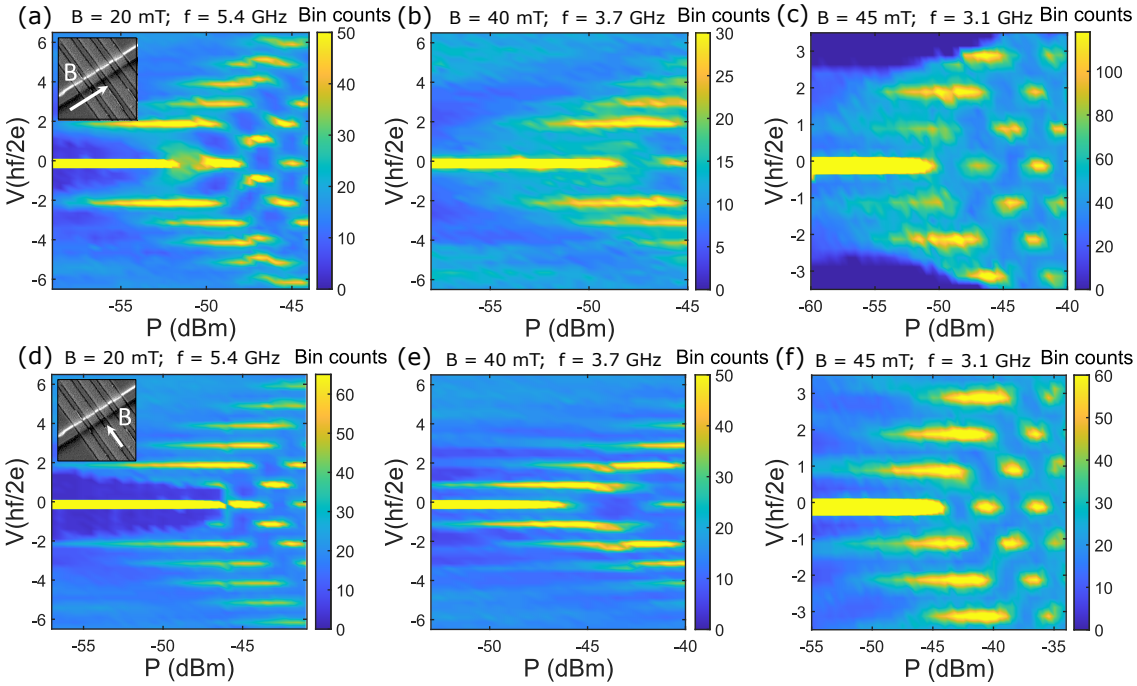

FIG. 6.13: Shapiro maps at magnetic fields parallel and perpendicular to the wire. (a-c) B parallel to the wire as shown in the inset of (a). Color maps of the bin counts at $B = 20\,\mathrm{mT}$ and $f = 5.4\,\mathrm{GHz}$, $B = 40\,\mathrm{mT}$ and $f = 3.7\,\mathrm{GHz}$, $B = 45\,\mathrm{mT}$ and $f = 3.1\,\mathrm{GHz}$. The first steps are strongly quenched or fully absent at these frequencies for the respective magnetic field values. (d-f) B perpendicular to the same wire as shown in the inset of (d). Color map of the bin counts at the same field strengths and frequencies than in the above color map, respectively. While in (d) the first step is quenched similar than in (a), in (e) and (f) all steps are fully visible. The latter is contrary to the observations in (b) and (c). This indicates an additional 4π-periodic component of the supercurrent when B is oriented along the wire.

Corresponding color maps for magnetic fields orientated along as well as perpendicular to the wire are shown in figure 6.13. The upper row (a-c) illustrates data for the field applied along the wire. For $B = 20$, 40 and 45 mT, we show the data of the highest frequency where the first Shapiro step is fully suppressed, respectively. The lower row (d-f) shows the corresponding maps for identical frequencies and magnetic field strengths while the field is orientated perpendicular to the wire. For $B = 20\,\mathrm{mT}$ and $f = 5.4\,\mathrm{GHz}$, the first Shapiro step is suppressed in both configurations. Thus, we expect a similar transition frequency $f_{4\pi}$ and 4π-periodic current $I_{4\pi}$. This suggests that $I_{4\pi}$ is mainly of trivial origin in the low field range. The situation changes

for higher magnetic fields. For $B = 40\,\mathrm{mT}$ at $f = 3.7\,\mathrm{GHz}$ and for $B = 45\,\mathrm{mT}$ at $f = 3.1\,\mathrm{GHz}$, the first Shapiro steps are suppressed when the magnetic field is orientated along the wire. However, the first steps are fully present if the magnetic field is oriented perpendicular to the wire. This indicates that there is an additional 4π-periodic contribution which only arises if the magnetic field is aligned along the wire.

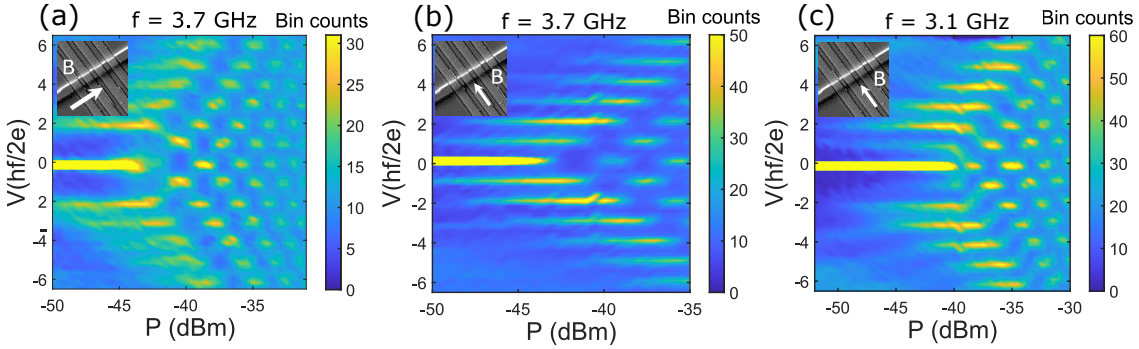

FIG. 6.14: Shapiro maps at $B = 30\,\mathrm{mT}$. The orientation of the magnetic field is shown in the inset, respectively. (a) For B along the wire, the first steps are fully absent at $f = 3.7\,\mathrm{GHz}$. (b) For B perpendicular to the wire, the first steps are slightly quenched at $f = 3.7\,\mathrm{GHz}$, but they are still well visible. (c) The perpendicular magnetic field has to be reduced to $f = 3.1\,\mathrm{GHz}$ to fully suppress the first steps.

For $B = 30\,\mathrm{mT}$ and $f = 3.7\,\mathrm{GHz}$, corresponding bin maps for a magnetic field along the wire (a) and perpendicular the wire (b) are presented in figure 6.14. The first steps are fully suppressed if the magnetic field is aligned along the wire. For the same magnetic field strength, orientated perpendicular to the wire, the first Shapiro steps are still visible. Hence, an additional 4π-periodic contribution is already present at $B = 30\,\mathrm{mT}$ for a magnetic field aligned along the wire. For the perpendicular magnetic field, we have to reduce the frequency to $f = 3.1\,\mathrm{GHz}$ to significantly reduce the first steps. The associated color map is shown in figure 6.14(c). This implies that $f_{4\pi}$ is lower for a perpendicular magnetic field compared to a parallel field of 30 mT, respectively. Thus, we conclude that the perfectly transmitting mode starts to emerge for parallel magnetic field in the range $B = 20 - 30\,\mathrm{mT}$. Due to limited resolution at low frequencies and low I_C, we are not able to perform experiments at lower frequencies for $B = 40\,\mathrm{mT}$ and $B = 45\,\mathrm{mT}$. Hence, we cannot determine the exact transition frequencies $f_{4\pi}$ when the magnetic field is aligned perpendicular to the wire. Therefore, the exact amplitudes of trivial and topological components for $B > 30\,\mathrm{mT}$ are unknown.

In summary, $I_{4\pi}$ is consistently lower for $B \geq 30\,\mathrm{mT}$ in the perpendicular configuration. These observations can be explained by trivial 4π-periodic contributions which get suppressed for both configurations with increasing magnetic fields while the topological perfectly transmitting mode only emerges with an increasing magnetic field

orientated along the wire. This also explains the decrease of $I_{4\pi}/I_C$ for $\Phi/\Phi_0 > 0.4$ in figure 6.11(d) since the topological 4π-periodic contribution is expected to vanish again. Therefore, our experiments are a first indication that one can indeed switch between trivial and topological superconductivity with an axial magnetic flux in topological insulator wires as suggested theoretically [23, 99, 160]. However, it is necessary to understand the exact behavior of Landau-Zener transition for different orientations of the magnetic field to prove the topological nature of the 4π-periodic current $I_{4\pi}$ for $\Phi/\Phi_0 > 0.4$ with certainty.

7 Summary

This thesis describes the studies of Josephson junctions made from topological insulator nanowires. Such nanowires in proximity to conventional superconductors have been proposed as a tunable platform to realize topological superconductivity and Majorana zero modes. The tuning is done using an axial magnetic flux Φ, which allows transforming the system from trivial at $\Phi = 0$ to topologically nontrivial when half a magnetic flux quantum $\Phi = \Phi_0/2 = h/2e$ penetrates the cross-sectional area of the wire.

In this work, we investigate Josephson junctions based on HgTe nanowires under the influence of a magnetic field. Additionally, we probe the expected transition from trivial to topological superconductivity as a function of the axial magnetic flux.

In an out-of-plane magnetic field, some devices studied show a Fraunhofer pattern, i.e. a modulation of the critical current I_C as a function of the magnetic field. The effects of magnetic flux focusing and spin-orbit interaction are taken into account to agree with the theoretically predicted evolution of the pattern. The absence of the pattern in other devices is explained by bad transmissions of the nanowire/superconductor interface or the extreme thinness of some wires.

For an axial magnetic field, we also observe a modulation of I_C for devices with low transmissions. Here, the modulations show periodicites of $\Phi = \Phi_S/2 = h/4e$ or $\Phi = \Phi_S/4 = h/8e$ where Φ is magnetic flux threading the cross-sectional area of the wire. For devices with high transmission, no modulation occurs, and I_C monotonously decays with the magnetic field. We relate these findings both experimentally and theoretically to the coupling of the superconducting contacts to the topological insulator nanowire. For a high transmission, all sides of the nanowire become superconducting due to the proximity effect. In contrast, only the interfaces directly covered by the superconductor, i.e. the top and the sides, are proximitized if the average transmission is rather low. Here, different types of transport paths exist while some of them pick up an additional phase induced by the magnetic flux. This additional phase causes a modification of the current-phase relation and, thus, leads to a modulation of the critical current as a function of the magnetic flux.

In Josephson junctions, an indication of emanating Majorana bound states is a 4π-periodic current-phase relation. A convenient way to probe the periodicity of the current-phase relation is the measurement of Shapiro steps. In the trivial situation,

all Shapiro steps are visible while the odd steps are supposed to disappear if the current-phase relation is 4π-periodic.

Hence, we probe the Shapiro step spectrum for different microwave frequencies and intensities. From the suppression of odd Shapiro steps, we extract the 4π- and 2π-periodic fraction of the critical current $I_{4\pi}/I_C$ and $I_{2\pi}/I_C$ using both a resistively shunted junction (RSJ) and a resistively and capacitively shunted junction (RCSJ) model. The ratio $I_{4\pi}/I_C$ depends strongly on the axial magnetic flux. While the total critical current I_C decreases with an increasing flux, the ratio $I_{4\pi}/I_C$ changes from approximately 6 % at $\Phi = 0$ up to a maximum around $\Phi = \Phi_0/2$. The presence of a finite $I_{4\pi}$ at $\Phi = 0$ and small magnetic fields is ascribed to Landau-Zener transitions between trivial Andreev bound states causing the 4π-periodic current. A method to distinguish between the trivial and the topological origin of the 4π-periodic currents is achieved by comparing the results for in-plane magnetic fields parallel to the wire as well as perpendicular to the wire. A topological 4π-periodic current is only proposed for the first configuration, while a trivial 4π-periodic current appear for both cases. Thus, our data suggest that the 4π-periodic current, which only appears for parallel magnetic fields $\gtrsim \Phi_0/4$, is mainly of topological origin. Therefore, our experiments provide an indication for the switching between trivial and topological superconductivity with an axial magnetic flux in topological insulator nanowires.

In a next step, the implementation of topgates on several junctions could be realized. This allows to reduce the effects of the bulk by tuning the Fermi level to the band gap. Furthermore, the fabrication of narrower wires would lead to a decreased number of trivial subbands. For this purpose, a perfect deposition of the superconducting contacts must be ensured. Additionally, a further improvement of the filtering would result in the suppression of disruptive effects such as quasiparticle poisoning. Furthermore, the behavior of Landau-Zener transitions in a magnetic field needs to be understood in more detail. This can allow to confirm the topological nature of the induced superconductivity in topological insulator nanowires.

The results of this thesis have shown that topological insulator nanowires represent a promising platform for topological superconductivity. In future experiments, the 'braiding' of Majorana zero modes would be a milestone in the realization of topological quantum computing. To verify the elementary braid of Majorana zero modes, a trijunction hosting a single topological qubit is propsed [161]. In addition, more complex networks made from sets of four and six wires with strategies for the optimization of robustness to quantities such as noise and the size can realize first scalable architectures for topological quantum computing [162].

References

1. Feynman, R. P. Simulating physics with computers. *International Journal of Theoretical Physics* **21,** 467–488 (1982).
2. Deutsch, D. Quantum theory, the Church–Turing principle and the universal quantum computer. *Proceedings of the Royal Society of London Series A* **400,** 97–117 (1985).
3. Grover, L. *A fast quantum mechanical algorithm for database search* in *Annual ACM Symposium on the Theory of Computing* (ACM, 1996), 212–219.
4. Shor, P. W. *Algorithms for quantum computation: Discrete logarithms and factoring* in *Proceedings 35th Annual Symposium on Foundations of Computer Science* (IEEE, 1994), 124–134.
5. Arute, F. *et al.* Quantum supremacy using a programmable superconducting processor. *Nature* **574,** 505–510 (2019).
6. Shor, P. W. Scheme for reducing decoherence in quantum computer memory. *Physical Review A* **52,** R2493(R) (1995).
7. Cory, D. G. *et al.* Experimental Quantum Error Correction. *Physical Review Letters* **81,** 2152 (1998).
8. Chiaverini, J. *et al.* Realization of quantum error correction. *Nature* **432,** 602–605 (2004).
9. Kitaev, A. Y. Fault-tolerant quantum computation by anyons. *Annals of Physics* **303,** 2–30 (2003).
10. Nayak, C., Simon, S. H., Stern, A., Freedman, M. & Das Sarma, S. Non-Abelian anyons and topological quantum computation. *Reviews of Modern Physics* **80,** 1083–1159 (2008).
11. Majorana, E. Teoria simmetrica dell'elettrone e del positrone. *Il Nuovo Cimento* **14,** 171–184 (1937).
12. Kitaev, A. Y. Unpaired Majorana fermions in quantum wires. *Physics-Uspekhi* **44,** 131–136 (2001).
13. Mackenzie, A. P., Scaffidi, T., Hicks, C. W. & Maeno, Y. Even odder after twenty-three years: the superconducting order parameter puzzle of Sr2RuO4. *npj Quantum Materials* **2,** 1–9 (2017).
14. Fu, L. & Kane, C. L. Superconducting proximity effect and majorana fermions at the surface of a topological insulator. *Physical Review Letters* **100,** 096407 (2008).
15. Alicea, J. New directions in the pursuit of Majorana fermions in solid state systems. *Reports on Progress in Physics* **75,** 076501 (2012).

16. Mourik, V. *et al.* Signatures of majorana fermions in hybrid superconductor-semiconductor nanowire devices. *Science* **336,** 1003–1007 (2012).

17. Rokhinson, L. P., Liu, X. & Furdyna, J. K. The fractional a.c. Josephson effect in a semiconductor-superconductor nanowire as a signature of Majorana particles. *Nature Physics* **8,** 795–799 (2012).

18. Deng, M. T. *et al.* Majorana bound state in a coupled quantum-dot hybrid-nanowire system. *Science* **354,** 1557–1562 (2016).

19. Albrecht, S. M. *et al.* Exponential protection of zero modes in Majorana islands. *Nature* **531,** 206–209 (2016).

20. Gül, Ö. *et al.* Ballistic Majorana nanowire devices. *Nature Nanotechnology* **13,** 192–197 (2018).

21. Zhang, H. *et al.* Retraction Note: Quantized Majorana conductance. *Nature* **591,** E30 (2021).

22. Das Sarma, S. & Pan, H. Disorder-induced zero-bias peaks in Majorana nanowires. *Physical Review B* **103,** 195158 (2021).

23. Cook, A. & Franz, M. Majorana fermions in a topological-insulator nanowire proximity-coupled to an s-wave superconductor. *Physical Review B* **84,** 201105 (2011).

24. Cook, A. M., Vazifeh, M. M. & Franz, M. Stability of Majorana fermions in proximity-coupled topological insulator nanowires. *Physical Review B* **86,** 155431 (2012).

25. Bardarson, J. H., Brouwer, P. W. & Moore, J. E. Aharonov-Bohm oscillations in disordered topological insulator nanowires. *Physical Review Letters* **105,** 156803 (2010).

26. Bardarson, J. H. & Moore, J. E. Quantum interference and Aharonov-Bohm oscillations in topological insulators. *Reports on Progress in Physics* **76,** 056501 (2013).

27. Kwon, H. J., Sengupta, K. & Yakovenko, V. M. Fractional ac Josephson effect in p- and d-wave superconductors. *The European Physical Journal B - Condensed Matter and Complex Systems* **37,** 349–361 (2004).

28. Kwon, H. J., Sengupta, K. & Yakovenko, V. M. Fractional ac Josephson effect in unconventional superconductors. *Fizika Nizkikh Temperatur (Kharkov)* **30,** 814–822 (2004).

29. Brüne, C. *et al.* Quantum Hall effect from the topological surface states of strained bulk HgTe. *Physical Review Letters* **106,** 126803 (2011).

30. Kozlov, D. A. *et al.* Transport properties of a 3D topological insulator based on a strained high-mobility HgTe film. *Physical Review Letters* **112,** 196801 (2014).

31. Kozlov, D. A. *et al.* Probing Quantum Capacitance in a 3D Topological Insulator. *Physical Review Letters* **116,** 166802 (2016).

32. Ziegler, J. *et al.* Probing spin helical surface states in topological HgTe nanowires. *Physical Review B* **97,** 035157 (2018).

33. Wiedenmann, J. *et al.* 4π-periodic Josephson supercurrent in HgTe-based topological Josephson junctions. *Nature Communications* **7,** 10303 (2016).

34. Bocquillon, E. *et al.* Gapless Andreev bound states in the quantum spin Hall insulator HgTe. *Nature Nanotechnology* **12,** 137–143 (2017).

35. Schüffelgen, P. *et al.* Selective area growth and stencil lithography for in situ fabricated quantum devices. *Nature Nanotechnology* **14,** 825–831 (2019).

36. Laroche, D. *et al.* Observation of the 4π-periodic Josephson effect in indium arsenide nanowires. *Nature Communications* **10,** 1–7 (2019).

37. Li, C. *et al.* 4π-periodic Andreev bound states in a Dirac semimetal. *Nature Materials* **17,** 875–880 (2018).

38. Shapiro, S. Josephson currents in Superconducting tunneling: The effect of microwaves and other observations. *Physical Review Letters* **11,** 80–82 (1963).

39. Domínguez, F., Hassler, F. & Platero, G. Dynamical detection of Majorana fermions in current-biased nanowires. *Physical Review B* **86,** 140503 (2012).

40. Dartiailh, M. C. *et al.* Missing Shapiro steps in topologically trivial Josephson junction on InAs quantum well. *Nature Communications* **12,** 1–9 (2021).

41. Hasan, M. Z. & Kane, C. L. Colloquium: Topological insulators. *Reviews of Modern Physics* **82,** 3045–3067 (2010).

42. Thouless, D. J., Kohmoto, M., Nightingale, M. P. & Den Nijs, M. Quantized hall conductance in a two-Dimensional periodic potential. *Physical Review Letters* **49,** 405–408 (1982).

43. Kohmoto, M. Topological invariant and the quantization of the Hall conductance. *Annals of Physics* **160,** 343–354 (1985).

44. Klitzing, K. V., Dorda, G. & Pepper, M. New method for high-accuracy determination of the fine-structure constant based on quantized hall resistance. *Physical Review Letters* **45,** 494–497 (1980).

45. Kane, C. L. & Mele, E. J. Quantum Spin hall effect in graphene. *Physical Review Letters* **95,** 226801 (2005).

46. Fu, L. & Kane, C. L. Topological insulators with inversion symmetry. *Physical Review B* **76,** 045302 (2007).

47. Fu, L., Kane, C. L. & Mele, E. J. Topological insulators in three dimensions. *Physical Review Letters* **98,** 106803 (2007).

48. Bernevig, B. A., Hughes, T. L. & Zhang, S. C. Quantum spin hall effect and topological phase transition in HgTe quantum wells. *Science* **314,** 1757–1761 (2006).

49. König, M. *et al.* Quantum spin hall insulator state in HgTe quantum wells. *Science* **318,** 766–770 (2007).

50. Ando, Y. Topological insulator materials. *Journal of the Physical Society of Japan* **82,** 102001 (2013).

51. Xiao, D., Chang, M. C. & Niu, Q. Berry phase effects on electronic properties. *Reviews of Modern Physics* **82,** 1959–2007 (2010).

52. Ando, T., Nakanishi, T. & Saito, R. Berry's Phase and Absence of Back Scattering in Carbon Nanotubes. *Journal of the Physical Society of Japan* **67,** 2857–2862 (1998).

53. Berchenko, N. N. & Pashkovskiĭ, M. V. Mercury telluride–a zero-gap semiconductor. *Soviet Physics - Uspekhi* **19,** 462–480 (1976).

54. Brüne, C. *et al.* Dirac-screening stabilized surface-state transport in a topological insulator. *Physical Review X* **4,** 041045 (2014).

55. Wu, S. C., Yan, B. & Felser, C. Ab initio study of topological surface states of strained HgTe. *Europhysics Letters* **107,** 57006 (2014).

56. Kozlovsky, R. *Magnetotransport in 3D Topological Insulator Nanowires.* PhD thesis (University of Regensburg, 2020).

57. Bardarson, J. H. & Ilan, R. in *Topological Matter* (eds Bercioux, D., Cayssol, J., Vergniory, M. G. & Calvo, M. R.) 93–114 (Springer, Cham, 2018).

58. Jauregui, L. A., Pettes, M. T., Rokhinson, L. P., Shi, L. & Chen, Y. P. Magnetic field-induced helical mode and topological transitions in a topological insulator nanoribbon. *Nature Nanotechnology* **11,** 345–351 (2016).

59. Tian, M. *et al.* Dual evidence of surface Dirac states in thin cylindrical topological insulator Bi2Te3 nanowires. *Scientific Reports* **3,** 1212 (2013).

60. Dufouleur, J. *et al.* Quasiballistic Transport of Dirac Fermions in a Bi2Se3 Nanowire. *Physical Review Letters* **110,** 186806 (2013).

61. Safdar, M. *et al.* Topological surface transport properties of single-crystalline SnTe nanowire. *Nano Letters* **13,** 5344–5349 (2013).

62. Hong, S. S., Zhang, Y., Cha, J. J., Qi, X. L. & Cui, Y. One-dimensional helical transport in topological insulator nanowire interferometers. *Nano Letters* **14,** 2815–2821 (2014).

63. Cho, S. *et al.* Aharonov-Bohm oscillations in a quasi-ballistic three-dimensional topological insulator nanowire. *Nature Communications* **6,** 1–5 (2015).

64. Bardeen, J., Cooper, L. N. & Schrieffer, J. R. Theory of superconductivity. *Physical Review* **108,** 1175–1204 (1957).

65. Schäpers, T. *Superconductor/semiconductor junctions* (Springer, Berlin, 2001).

66. Tinkham, M. *Introduction to superconductivity* (McGraw-Hill Inc., New York, 1996).

67. Schmidt, V. V. *The Physics of Superconductors - Introduction to Fundamentals and Applications* (Springer, Berlin, 1997).

68. Valatin, J. G. Comments on the theory of superconductivity. *Il Nuovo Cimento* **7,** 843–857 (1958).

69. Bogoljubov, N. N. On a new method in the theory of superconductivity. *Il Nuovo Cimento* **7,** 794–805 (1958).

70. Fernandes, R. M. *Lecture Notes: BCS theory of superconductivity* (2015).

71. De Gennes, P.-G. *Superconductivity of metals and alloys* (Westview Press, 1999).

72. Sigrist, M. in *Topology, Entanglement, and Strong Correlations Modeling and Simulations* (eds Pavarini, E. & Koch, E.) (Forschungszentrum Jülich GmbH, 2020).

73. De Juan, F., Bardarson, J. H. & Ilan, R. Conditions for fully gapped topological superconductivity in topological insulator nanowires. *SciPost Physics* **6,** 060 (2019).

74. Andreev, A. F. Thermal conductivity of the intermediate state of superconductors. II. *J. Exptl. Theoret. Phys. (U.S.S.R.)* **47,** 2222–2228 (1964).

75. Blonder, G. E., Tinkham, M. & Klapwijk, T. M. Transition from metallic to tunneling regimes in superconducting microconstrictions: Excess current, charge imbalance, and supercurrent conversion. *Physical Review B* **25,** 4515–4532 (1982).

76. Josephson, B. D. Possible new effects in superconductive tunnelling. *Physics Letters* **1,** 251–253 (1962).

77. McMillan, W. L. Tunneling Model of the Superconducting Proximity Effect. *Physical Review* **175,** 537 (1968).

78. Thouless, D. J. Maximum Metallic Resistance in Thin Wires. *Physical Review Letters* **39,** 1167 (1977).

79. Gross, R. & Marx, A. *Applied Superconductivity: Josephson Effect and Superconducting Electronics* (Walther-Meißner Institut, München, 2005).

80. Stewart, W. C. Current-voltage characteristics of Josephson junctions. *Applied Physics Letters* **12,** 277–280 (1968).

81. McCumber, D. E. Effect of ac impedance on dc voltage-current characteristics of superconductor weak-link junctions. *Journal of Applied Physics* **39,** 3113–3118 (1968).

82. Ambegaokar, V. & Halperin, B. I. Voltage due to thermal noise in the dc Josephson effect. *Physical Review Letters* **22,** 1364–1366 (1969).

83. Russer, P. Influence of microwave radiation on current-voltage characteristic of superconducting weak links. *Journal of Applied Physics* **43,** 2008–2010 (1972).

84. Rohlfing, F. *Induzierte Supraleitung in Nb/InAs-Hybridstrukturen in parallelen und senkrechten Magnetfeldern.* PhD Thesis (University of Regensburg, 2007).

85. Yip, S. K. Magnetic-field effect on the supercurrent of an SNS junction. *Physical Review B* **62,** R6127(R) (2000).

86. Heikkilä, T. T., Wilhelm, F. K. & Schön, G. Non-equilibrium supercurrent through mesoscopic ferromagnetic weak links. *Europhysics Letters* **51,** 434–440 (2000).

87. Crosser, M. S. *et al.* Nonequilibrium transport in mesoscopic multi-terminal SNS Josephson junctions. *Physical Review B* **77,** 014528 (2008).

88. Maier, L. *Induced Superconductivity in the Topological Insulator Mercury Telluride.* Phd Thesis (University of Würzburg, 2015).

89. London, F. & London, H. The electromagnetic equations of the supraconductor. *Proceedings of the Royal Society of London Series A* **149,** 71–88 (1935).

90. Sigrist, M. *Introduction to unconventional superconductivity* in *AIP Conference Proceedings* **789** (AIP, 2005), 165–243.

91. Dirac, P. A theory of electrons and protons. *Proceedings of the Royal Society of London Series A* **126,** 360–365 (1930).

92. Beenakker, C. W. Search for majorana fermions in superconductors. *Annual Review of Condensed Matter Physics* **4,** 113–136 (2013).

93. Wilczek, F. Majorana returns. *Nature Physics* **5,** 614–618 (2009).

94. Leijnse, M. & Flensberg, K. Introduction to topological superconductivity and Majorana fermions. *Semiconductor Science and Technology* **27,** 124003 (2012).

95. Von Oppen, F., Peng, Y. & Pientka, F. in *Topological Aspects of Condensed Matter Physics: Lecture Notes of the Les Houches Summer School* (eds Cugliandolo; L. F., Moessner; R., Goerbig; M. O. & Chamon, C.) 387–450 (Oxford University Press, Oxford, 2017).

96. Read, N. & Green, D. Paired states of fermions in two dimensions with breaking of parity and time-reversal symmetries and the fractional quantum Hall effect. *Physical Review B* **61,** 10267 (2000).

97. Hughes, T. L. in *Topological Insulators and topological superconducors* (ed Bernevig, B. A.) 193–213 (Princeton University Press, Princeton and Oxford, 2013).

98. Jackiw, R. & Rebbi, C. Solitons with fermion number ½. *Physical Review D* **13,** 3398 (1976).

99. De Juan, F., Ilan, R. & Bardarson, J. H. Robust transport signatures of topological superconductivity in topological insulator nanowires. *Physical Review Letters* **113,** 107003 (2014).

100. Legg, H. F., Loss, D. & Klinovaja, J. Majorana bound states in topological insulators without a vortex. *Physical Review B* **104,** 165405 (2021).

101. Ziegler, J. *Quantum transport in HgTe topological insulator nanostructures.* PhD thesis (University of Regensburg, 2019).

102. Pleyer, M. *Untersuchung des nasschemischen Ätzprozesses von Nanostrukturen in HgTe.* Bachelor's thesis (University of Regensburg, 2015).

103. Maier, J. *Optimierung der Herstellung von supraleitenden Kontakten auf HgTe-basierten topologischen Isolatoren.* Bachelor's thesis (University of Regensburg, 2018).

104. Enss, C. & Hunklinger, S. *Tieftemperaturphysik* (Springer, Berlin Heidelberg, 2000).

105. Johnson, J. B. Thermal Agitation of Electricity in Conductors. *Physical Review* **32,** 97 (1928).

106. Nyquist, H. Thermal agitation of electric charge in conductors. *Physical Review* **32,** 110–113 (1928).

107. Wittl, W. *Herstellung eines Tieftemperaturfilters zur Messung von Supraleiter / Topologische Isolator Strukturen.* Bachelor's thesis (University of Regensburg, 2018).

108. Scheller, C. P. *et al.* Silver-epoxy microwave filters and thermalizers for millikelvin experiments. *Applied Physics Letters* **104,** 211106 (2014).

109. Laird. *Eccosorb CRS - Two-Part Castable Silicone Load Absorber.* Data Sheet (2016).

110. Jackson, J. D. *Classical Electrodynamics.* (Wiley, 1998).

111. Reinhardt, S. *et al.* Lab::Measurement-A portable and extensible framework for controlling lab equipment and conducting measurements. *Computer Physics Communications* **234,** 216–222 (2019).

112. Kvon, Z. D. *et al.* Two-dimensional electron-hole system in HgTe-based quantum wells with surface orientation (112). *Physical Review B* **83,** 193304 (2011).

113. Weishäupl, S. *Quanteninterferenzeffekte in topologischen Isolatoren und magnetischen Halbleitern.* Phd Thesis (University of Regensburg, 2014).

114. Matthias, B. T., Geballe, T. H. & Compton, V. B. Superconductivity. *Reviews of Modern Physics* **35,** 1 (1963).

115. Dantscher, K. M. *et al.* Cyclotron-resonance-assisted photocurrents in surface states of a three-dimensional topological insulator based on a strained high-mobility HgTe film. *Physical Review B* **92,** 165314 (2015).

116. Fulton, T. A. & Dunkleberger, L. N. Origin of hysteresis in the I-V curves of point-contact junctions. *Journal of Applied Physics* **45,** 2283 (2003).

117. Courtois, H., Meschke, M., Peltonen, J. T. & Pekola, J. P. Origin of hysteresis in a proximity josephson junction. *Physical Review Letters* **101,** 067002 (2008).

118. Octavio, M., Tinkham, M., Blonder, G. E. & Klapwijk, T. M. Subharmonic energy-gap structure in superconducting constrictions. *Physical Review B* **27,** 6739–6746 (1983).

119. Flensberg, K., Hansen, J. B. & Octavio, M. Subharmonic energy-gap structure in superconducting weak links. *Physical Review B* **38,** 8707–8711 (1988).

120. Niebler, G., Cuniberti, G. & Novotný, T. Analytical calculation of the excess current in the Octavio–Tinkham–Blonder–Klapwijk theory. *Superconductor Science and Technology* **22,** 085016 (2009).

121. Cuevas, J. C. *Electronic Transport in Normal and Superconducting Nanocontacts.* PhD Thesis (Universidad Autonoma de Madrid, 1999).

122. Averin, D. & Bardas, A. ac Josephson Effect in a Single Quantum Channel. *Physical Review Letters* **75,** 1831–1834 (1995).

123. Cuevas, J., Martín-Rodero, A. & Yeyati, A. L. Hamiltonian approach to the transport properties of superconducting quantum point contacts. *Physical Review B* **54,** 7366 (1996).

124. Maxfield, B. W. & McLean, W. L. Superconducting Penetration Depth of Niobium. *Physical Review* **139,** A1515 (1965).

125. Paajaste, J. *et al.* Pb/InAs nanowire josephson junction with high critical current and magnetic flux focusing. *Nano Letters* **15,** 1803–1808 (2015).

126. Angers, L. *et al.* Proximity dc squids in the long-junction limit. *Physical Review B* **77,** 165408 (2008).

127. Frielinghaus, R. *et al.* Josephson supercurrent in Nb/InN-nanowire/Nb junctions. *Applied Physics Letters* **96,** 132504 (2010).

128. Cuevas, J. C. & Bergeret, F. S. Magnetic interference patterns and vortices in diffusive SNS junctions. *Physical Review Letters* **99,** 217002 (2007).

129. Stampfer, L. *et al.* Andreev Interference in the Surface Accumulation Layer of Half-Shell InAsSb/Al Hybrid Nanowires. *Advanced Materials* **34,** 2108878 (2022).

130. Gharavi, K., Holloway, G. W., LaPierre, R. R. & Baugh, J. Nb/InAs nanowire proximity junctions from Josephson to quantum dot regimes. *Nanotechnology* **28,** 085202 (2017).

131. Zuo, K. *et al.* Supercurrent Interference in Few-Mode Nanowire Josephson Junctions. *Physical Review Letters* **119,** 187704 (2017).

132. Fuchs, J. *Transport and subgap states in superconducting heterostructures with effective Dirac systems.* PhD Thesis (University of Regensburg, 2022).

133. Himmler, W. *et al.* Supercurrent interference in HgTe Josephson junctions. *arXiv,* 2211.06702 (2022).

134. Barth, M. *ongoing PhD thesis* 2022.

135. Groth, C. W., Wimmer, M., Akhmerov, A. R. & Waintal, X. Kwant: a software package for quantum transport. *New Journal of Physics* **16,** 063065 (2014).

136. Sriram, P., Kalantre, S. S., Gharavi, K., Baugh, J. & Muralidharan, B. Supercurrent interference in semiconductor nanowire Josephson junctions. *Physical Review B* **100,** 155431 (2019).

137. Little, W. A. & Parks, R. D. Observation of Quantum Periodicity in the Transition Temperature of a Superconducting Cylinder. *Physical Review Letters* **9,** 9 (1962).

138. Deaver, B. S. & Fairbank, W. M. Experimental Evidence for Quantized Flux in Superconducting Cylinders. *Physical Review Letters* **7,** 43 (1961).

139. Doll, R. & Näbauer, M. Experimental Proof of Magnetic Flux Quantization in a Superconducting Ring. *Physical Review Letters* **7,** 51 (1961).

140. Zadorozhny, Y. & Liu, Y. Fractional-flux little-parks resistance oscillations in disordered superconducting Au0.7In0.3 cylinders. *Europhysics Letters* **55,** 712–718 (2001).

141. Li, Y., Xu, X., Lee, S.-P. & Chien, C. L. Fractional Little-Parks effect observed in a topological superconductor. *arXiv,* 2003.00603 (2020).

142. Li, Y., Xu, X., Lee, M. H., Chu, M. W. & Chien, C. L. Observation of half-quantum flux in the unconventional superconductor β-Bi2Pd. *Science* **366,** 238–241 (2019).

143. Domínguez, F. *et al.* Josephson junction dynamics in the presence of 2π - and 4π -periodic supercurrents. *Physical Review B* **95,** 195430 (2017).

144. Picó-Cortés, J., Domínguez, F. & Platero, G. Signatures of a 4π-periodic supercurrent in the voltage response of capacitively shunted topological Josephson junctions. *Physical Review B* **96,** 125438 (2017).

145. Wiedenmann, J. *Induced topological superconductivity in HgTe based nanostructures.* PhD Thesis (University of Würzburg, 2017).

146. Le Calvez, K. *et al.* Joule overheating poisons the fractional ac Josephson effect in topological Josephson junctions. *Communications Physics* **2,** 1–9 (2019).

147. Baars, P., Richter, A. & Merkt, U. Temperature and power dependence of Shapiro and Fiske step widths in Nb/InAs/Nb Josephson junctions. *Physical Review B* **67,** 224501 (2003).

148. Larkin, A. I. & Ovchinnikov, Y. N. Decay of the supercurrent in tunnel junctions. *Physical Review B* **28,** 6281 (1983).

149. Antonenko, D. S. & Skvortsov, M. A. Quantum decay of the supercurrent and intrinsic capacitance of Josephson junctions beyond the tunnel limit. *Physical Review B* **92,** 214513 (2015).

150. Wellstood, F. C., Urbina, C. & Clarke, J. Hot-electron effects in metals. *Physical Review B* **49,** 5942 (1994).

151. Le Calvez, K. *Signatures of a 4pi periodic Andreev bound state in topological Josephson junctions.* PhD Thesis (Universite Grenoble Alpes, 2017).

152. Roukes, M. L., Freeman, M. R., Germain, R. S., Richardson, R. C. & Ketchen, M. B. Hot electrons and energy transport in metals at millikelvin temperatures. *Physical Review Letters* **55,** 422 (1985).

153. Echternach, P. M., Thoman, M. R., Gould, C. M. & Bozler, H. M. Electron-phonon scattering rates in disordered metallic films below 1 K. *Physical Review B* **46,** 10339 (1992).

154. Reizer, M. Y. Electron-phonon relaxation in pure metals and superconductors at very low temperatures. *Physical Review B* **40,** 5411 (1989).

155. Fischer, R. *et al.* 4π-periodic supercurrent tuned by an axial magnetic flux in topological insulator nanowires. *Physical Review Research* **4,** 013087 (2022).

156. Picó Cortés, J. *AC dynamics of quantum dots and Josephson junctions for quantum technologies.* PhD Thesis (Universidad Autónoma de Madrid, 2021).

157. Golubov, A. A., Kupriyanov, M. Y. & Il'ichev, E. The current-phase relation in Josephson junctions. *Reviews of Modern Physics* **76,** 411 (2004).

158. Kautz, R. L. & Martinis, J. M. Noise-affected I-V curves in small hysteretic Josephson junctions. *Physical Review B* **42,** 9903 (1990).

159. Chiu, C. K. & Das Sarma, S. Fractional Josephson effect with and without Majorana zero modes. *Physical Review B* **99,** 035312 (2019).

160. Sitthison, P. & Stanescu, T. D. Robustness of topological superconductivity in proximity-coupled topological insulator nanoribbons. *Physical Review B* **90,** 035313 (2014).

161. Aasen, D. *et al.* Milestones toward Majorana-based quantum computing. *Physical Review X* **6,** 031016 (2016).

162. Karzig, T. *et al.* Scalable designs for quasiparticle-poisoning-protected topological quantum computation with Majorana zero modes. *Physical Review B* **95,** 235305 (2017).

A Process documentation

This section contains a detailed description of the fabrication process. Here, we show the final version of the documentation since the different fabrication steps have been optimized continuously.

Wafer splitting

- Clean wafer (30 s acetone → 30 s isopropyl alcohol)
- Spin coat protective resist *Shipley 1813* (1500 rpm for 30 s), bake (5 min at 80 °C)
- Scribe wafer with *ATV Diamond Scriber RV-129* to 3.2 cm × 3.7 cm big sample pieces, scribe force 5-7 cm, repeat 3-4×
- Split wafer over glass edge with clean tape

Nanowire structuring

- Clean sample (30 s acetone in ultrasonic bath → 30 s acetone → 30 s isopropyl alcohol)
- Spin coat with *CSAR* 9 % (800 rpm for 3 s → 5000 rpm for 40 s), bake (20 min at 80 °C)
- Expose 'nanowire structures' in the electron microscope (*Zeiss Auriga*) at 3 kV by two steps:
  - Detailed structure in proximity to the nanowire: 30 µm aperture, dose: 50 µC/cm^2
  - Remaining area on the sample: 120 µm aperture, dose: 50 µC/cm^2
- Develop with *AR-600-546* for 30 s, stop process in isopropyl alcohol (30 s)
- Wet chemical etching with solution of Br_2:$C_2H_6O_2$:H_2O=0.1 : 100 : 25 ml at 0 °C (magnetic stirring rod at 300 rpm), typical etching times are between 4:00-4:30 min depending on the thickness of the HgTe and cap layer, jiggle sample holder shortly every 30 s, stop process in pure water (2 × 5 s)

- Remove remaining resist with *AR-600-71* for 30 s, clean sample in isopropyl alcohol (30 s)

Removal of the cap layer: Test stripes to determine the etching rate

- Spin coat with *CSAR* 9 % (800 rpm for 3 s → 5000 rpm for 40 s), bake (20 min at 80 °C)
- Expose 'teststripes' in the electron microscope (*Zeiss Auriga*) at 3 kV: 30 µm aperture, dose: 150 µC/cm^2
- Develop with *AR-600-546* for 30 s, stop process in isopropyl alcohol (30 s)
- Wet chemical etching with solution of Br_2:$C_2H_6O_2$:H_2O=∼0.015 : 100 : 25 ml at 0 °C (magnetic stirring rod at 300 rpm), typical etching times are between 20-30 s for a 60 nm thick cap layer, stop process in pure water (2 × 5 s)
- Remove remaining resist with *AR-600-71* for 30 s, clean sample in isopropyl alcohol (30 s)
- Determine etching depth using atomic force microscopy, calculate exact etching time to remove 60 nm. It is important to ensure an almost identical etching process (e.g. usage of the same pipette) in the next step.

Removal of the cap layer at position of the superconducting contatcs

- Spin coat with *CSAR* 9 % (800 rpm for 3 s → 5000 rpm for 40 s), bake (20 min at 80 °C)
- Expose 'superconducting contacts' in the electron microscope (*Zeiss Auriga*) at 3 kV: 30 µm aperture, dose: 150 µC/cm^2
- Develop with *AR-600-546* for 30 s, stop process in isopropyl alcohol (30 s)
- Wet chemical etching with solution of Br_2:$C_2H_6O_2$:H_2O=∼0.015 : 100 : 25 ml at 0 °C (magnetic stirring rod at 300 rpm) for the previously determined time, stop process in pure water (2 × 5 s)

Superconducting contatcs

- Mounting the sample in the pre-chamber of the *UHV Orion Sputtering System*, pump down to ∼ 10^{-6} mbar
  - Ar^+-milling using a Kaufman ion source for 10-15 s (I_{cat} ∼ 5.9 A, I_{dis} = 0.1 V, V_{dis} = 40 V, V_{beam} = 150 V, V_{acc} = 90 V, flow: 4 %, pressure: ∼1.5 × 10^{-3} mbar)
  - Transfer sample to the main chamber via the load lock and place the sample at the lowest position

- Deposit 3 nm Ti by thermal evaporation (rate: 0.4 Å/s)
- Deposit 60 nm Nb by dc sputtering ($P = 250$ W, flow: 40 %, pressure: $\sim 5 \times 10^{-3}$ mbar) at an angle $\alpha \approx 45\,^{\circ}$ (corresponds to position 0 mm on milimeter screw)
- Deposit 2 nm Pt by thermal evaporation (rate: 0.2 Å/s)

- Lift-off in *AR-600-71* (15 min at 60 °C → 30 s in ultrasonic bath → remove excess materials with syringe), clean sample in isopropyl alcohol (30 s)

Metallic contacts

- Spin coat with *CSAR* 9 % (800 rpm for 3 s → 5000 rpm for 40 s), bake (20 min at 80 °C)
- Expose 'metallic contacts' in the electron microscope (*Zeiss Auriga*) at 3 kV by two steps:
  - Detailed structure in proximity to the superconducting contacts: 30 µm aperture, dose: 50 µC/cm^2
  - Large contacts pads on the outer part of the sample: 120 µm aperture, dose: 50 µC/cm^2
- Develop with *AR-600-546* for 30 s, stop process in isopropyl alcohol (30 s)
- Mount the sample in *Leybold Univex 450*, pump down to $\sim 10^{-6}$ mbar
  - Ar^+-milling for 60 s ($V = 3$ kV, $I = 35$ mA, pressure: $\sim 1 \times 10^{-3}$ mbar)
  - Deposit 10 nm Ti by thermal evaporation (rate :1 Å/s)
  - Deposit 100 nm Au by thermal evaporation (rate :1.9 Å/s)
- Lift-off in *AR-600-71* (15 min at 60 °C → remove excess materials with syringe), clean sample in isopropyl alcohol (30 s)
- Develop with *AR-600-546* for 30 s, stop process in isopropyl alcohol (30 s)

Only sample r*I*: Fabrication of a topgate

- Spin coat with *CSAR* 9 % (800 rpm for 3 s → 5000 rpm for 40 s), bake (20 min at 80 °C)
- Expose 'insulator' in the electron microscope (*Zeiss Auriga*) at 3 kV: 120 µm aperture, dose: 50 µC/cm^2
- Develop with *AR-600-546* for 30 s, stop process in isopropyl alcohol (30 s)
- deposit 30 nm SiO_2 by PECVD (*Oxford Plasmalab 80Plus*), 3×15 s, gas flow: SiH_4 710 sccm; N_2O 170 sccm, 80 °C, 150 W

- deposit 100 nm Al_2O_3 in ALD (*Cambridge NanoTech Savannah 100*) at 80 °C, 66 s purge time, 1100 cycles
- Lift-off in *AR-600-71* (15 min at 60 °C → remove excess materials with syringe), clean sample in isopropyl alcohol (30 s)
- Spin coat with *CSAR* 9 % (800 rpm for 3 s → 5000 rpm for 40 s), bake (20 min at 80 °C)
- Expose 'topgate' in the electron microscope (*Zeiss Auriga*) at 3 kV: 30 µm aperture, dose: 60 µC/cm^2
- Develop with *AR-600-546* for 30 s, stop process in isopropyl alcohol (30 s)
- Mount the sample in *Leybold Univex 450*, pump down to $\sim 10^{-6}$ mbar
  - Ar^+-milling for 30 s ($V = 2$ kV, $I = 25$ mA, pressure: $\sim 4 \times 10^{-3}$ mbar)
  - Deposit 10 nm Ti by thermal evaporation (rate: 1 Å/s)
  - Deposit 100 nm Au by thermal evaporation (rate: 1.9 Å/s)
- Lift-off in *AR-600-71* (15 min at 60 °C → remove excess materials with syringe), clean sample in isopropyl alcohol (30 s)

Contacting to chip carrier

- glue sample into chip carrier with PMMA resist, cure resist 20 min at 80 °C
- bond contact pads to chip carrier with 25 μm Au wire on the *MEI gold bonder*, Settings: Power 1: 6, Time 1: 6; Power 2: 4, Time 2: 6

B Supplementary data

This section contains additional data of sample r2 and r3.

Sample r2

In this section, we show additional data of sample r2 at $\Phi = 0$, at $\Phi = 0.35\,\Phi_0$, and at $\Phi = 0.52\,\Phi_0$.

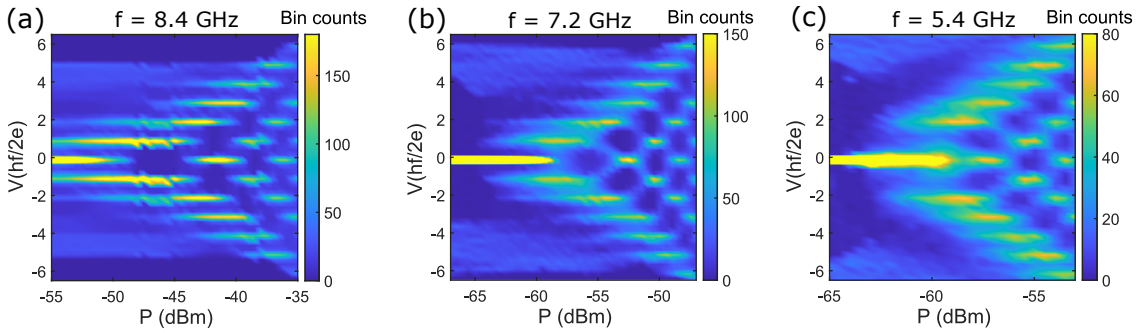

FIG. B.1: Frequency dependence of Shapiro steps at $B = 0\,\mathrm{mT}$ (a-c) Color maps of the bin counts of sample r2 at frequencies $f = 8.4\,\mathrm{GHz}$, $7.2\,\mathrm{GHz}$, and $5.4\,\mathrm{GHz}$. The transition frequency is $f_{4\pi} = 7.8\,\mathrm{GHz}$. We estimate $I_{4\pi}/I_C \approx 0.07$ using the RSJ model.

Figure B.1(a-c) illustrates the color maps of the bin counts as a function of the power P and the normalized voltage V for different frequencies f at $\Phi = 0$. All Shapiro steps are visible for $f = 8.4\,\mathrm{GHz}$. At $f = 7.2\,\mathrm{GHz}$, the first steps $n = \pm 1$ are reduced while they are fully absent at $f = 5.4\,\mathrm{GHz}$. The transition frequency is $f_{4\pi} \approx 7.8\,\mathrm{GHz}$. With equation (6.2.4), we calculate the amplitude of the 4π-periodic supercurrent $I_{4\pi} \approx 13\,\mathrm{nA}$. With $I_C\,(0\,\mathrm{mT}) = 180\,\mathrm{nA}$, $I_{4\pi}/I_C \approx 7\,\%$.

Figure B.2(a-c) shows the data of sample r2 measured at $B = 150\,\mathrm{mT}$ where the magnetic field B is aligned along the wire. This value corresponds to a magnetic flux $\Phi = BA \approx 0.35\,\Phi_0$. The first Shapiro steps are fully present at $f = 7.2\,\mathrm{GHz}$. At $f = 6.2\,\mathrm{GHz}$, the first steps are reduced, and they are fully suppressed at $f = 5.1\,\mathrm{GHz}$. We obtain the transition frequency $f_{4\pi} = 6.7\,\mathrm{GHz}$ and calculate $I_{4\pi} \approx 11\,\mathrm{nA}$ using

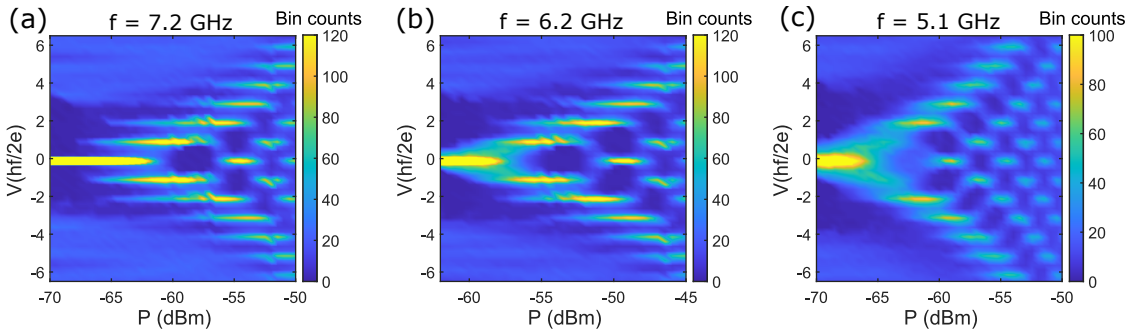

FIG. B.2: Frequency dependence of Shapiro steps at $B = 150\,\mathrm{mT}$ ($\Phi = 0.35\,\Phi_0$) (a-c) Color maps of the bin counts of sample r2 at frequencies $f = 7.2\,\mathrm{GHz}$, $6.2\,\mathrm{GHz}$, and $5.1\,\mathrm{GHz}$. The transition frequency is $f_{4\pi} = 6.7\,\mathrm{GHz}$. We estimate $I_{4\pi}/I_C \approx 0.10$ using the RSJ model.

equation (6.2.4). The total critical current I_C decreases with B to $I_C\,(150\,\mathrm{mT}) = 111\,\mathrm{nA}$. Thus, the fraction of the 4π-periodic current is $I_{4\pi}/I_C \approx 0.10$.

Figure B.3(a-c) shows the data of sample r2 measured at $B = 225\,\mathrm{mT}$. This value corresponds to a magnetic flux $\Phi = BA \approx 0.52\,\Phi_0$. All Shapiro steps are visible at $f = 6.2\,\mathrm{GHz}$ and $f = 4.5\,\mathrm{GHz}$. At $f = 3.4\,\mathrm{GHz}$, the first steps are reduced and the second steps dominate. The transition frequency is $f_{4\pi} = 4.0\,\mathrm{GHz}$. Thus, we obtain $I_{4\pi} \approx 7\,\mathrm{nA}$ using equation (6.2.4). With $I_C\,(225\,\mathrm{mT}) = 51\,\mathrm{nA}$, the fraction of the 4π-periodic current is $I_{4\pi}/I_C \approx 0.13$.

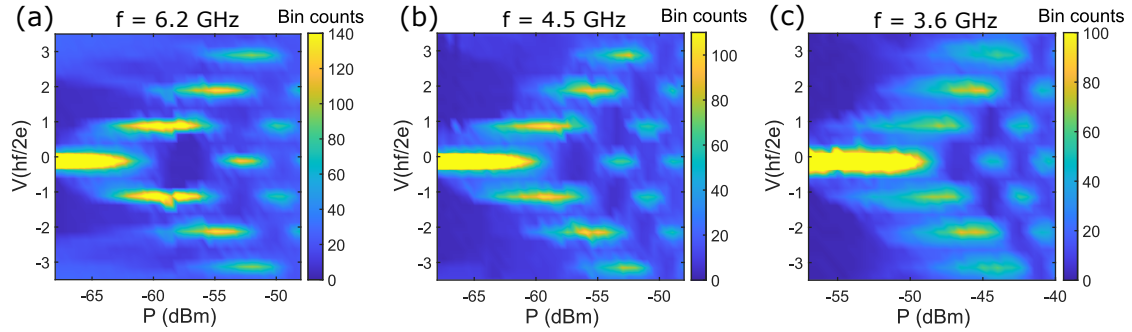

FIG. B.3: Frequency dependence of Shapiro steps at $B = 225\,\mathrm{mT}$ ($\Phi = 0.52\,\Phi_0$) (a-c) Color maps of the bin counts of sample r2 at frequencies $f = 6.2\,\mathrm{GHz}$, $4.5\,\mathrm{GHz}$, and $3.6\,\mathrm{GHz}$. The transition frequency is $f_{4\pi} = 4.0\,\mathrm{GHz}$. We estimate $I_{4\pi}/I_C \approx 0.13$ using the RSJ model.

Sample r3

In this section, we show additional data of sample r3 at $\Phi = 0$ and at $\Phi = 0.44\,\Phi_0$, where the fraction $I_{4\pi}/I_C$ has a maximum.

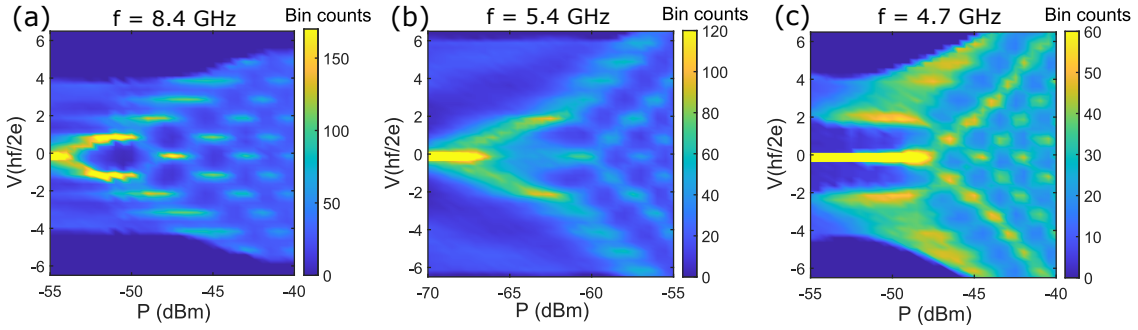

FIG. B.4: Frequency dependence of Shapiro steps at $B = 0\,\mathrm{mT}$ (a-c) Color maps of the bin counts of sample r3 at frequencies $f = 8.4\,\mathrm{GHz}$, $5.4\,\mathrm{GHz}$, and $4.7\,\mathrm{GHz}$. The transition frequency is $f_{4\pi} = 5.8\,\mathrm{GHz}$. We estimate $I_{4\pi}/I_C \approx 0.06$ using the RSJ model.

Figure B.4(a-c) illustrates the color maps of the bin counts as a function of the power P and the normalized voltage V for different frequencies f at $\Phi = 0$. All Shapiro steps are visible for $f = 8.4\,\mathrm{GHz}$. By reducing the frequency to $f = 5.4\,\mathrm{GHz}$, the first steps $n = \pm 1$ become completely suppressed. At $f = 4.7\,\mathrm{GHz}$, the third steps are also fully quenched. The transition frequency is $f_{4\pi} \approx 5.8\,\mathrm{GHz}$. With equation (6.2.4), we calculate the amplitude of the 4π-periodic supercurrent $I_{4\pi} \approx 16\,\mathrm{nA}$. With $I_C\,(0\,\mathrm{mT}) = 265\,\mathrm{nA}$, this corresponds to $I_{4\pi}/I_C \approx 6\,\%$.

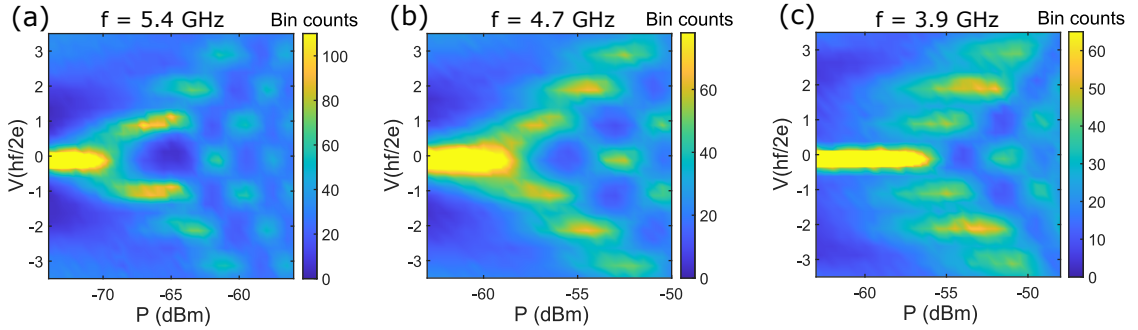

FIG. B.5: Frequency dependence of Shapiro steps at $B = 100\,\mathrm{mT}$ ($\Phi = 0.44\,\Phi_0$) (a-c) Color maps of the bin counts of sample r3 at frequencies $f = 5.4\,\mathrm{GHz}$, $4.7\,\mathrm{GHz}$, and $3.9\,\mathrm{GHz}$. The transition frequency is $f_{4\pi} = 4.8\,\mathrm{GHz}$. We estimate $I_{4\pi}/I_C \approx 0.21$ using the RSJ model.

Figure B.5(a-c) shows the data of sample r3 measured at $B = 100\,\mathrm{mT}$ where the magnetic field B is aligned along the wire. This value corresponds to a magnetic

flux $\Phi = BA \approx 0.44\,\Phi_0$. The first Shapiro steps, fully present at $f = 5.4\,\mathrm{GHz}$, are weakened at $f = 4.7\,\mathrm{GHz}$. At $f = 3.9\,\mathrm{GHz}$, the second steps clearly dominate. We extract the transition frequency $f_{4\pi} = 4.8\,\mathrm{GHz}$. Thus, we obtain $I_{4\pi} \approx 13\,\mathrm{nA}$ using equation (6.2.4). Since the total critical current I_C decreases strongly with B to $I_C\,(100\,\mathrm{mT}) = 63\,\mathrm{nA}$, the fraction of the 4π-periodic current is $I_{4\pi}/I_C \approx 0.21$.

Danksagung

An dieser Stelle möchte ich mich herzlichst bei einigen Personen bedanken, die die Durchführung dieser Arbeit ermöglicht und mich dabei unterstützt haben:

- Besonders möchte ich mich bei Prof. Dieter Weiss bedanken, der mir die Durchführung dieses spannenden und viel versprechenden Themas ermöglicht hat. Vielen Dank für das stetige Interesse am Fortschreiten der Arbeit und die zahlreichen Diskussionen.
- Dr. Dmitry Kozlov für die Ratschläge zu den Messungen und zum Materialsystem. Zusätzlich möchte ich Nikolai Mikhailov und Sergey Dvoretsky für die Versorgung mit HgTe Wafern danken.
- Jordi Picó-Cortès, Prof. Gloria Platero und Prof. Milena Grifoni für die hervorragende Kollaboration und die unzähligen Simulationen zu meinen Messsungen.
- Michael Barth, Jacob Fuchs und Prof. Klaus Richter für das Entwickeln der Theorie zu meinen Messergebnissen und die zahlreichen Diskussionen darüber.
- Prof. Christoph Strunk für die fachlichen Diskussionen und Ratschläge rund um die Supraleitung.
- Prof. Milena Grifoni für die Übernahme des Zweitgutachtens.
- Dr. Johannes Ziegler, Dr. Alexei Iankilevitch, Wolfgang Himmler, Elisabeth Richter und Michael Weigl für die reibungslose Zusammenarbeit bei der Betreuung unseres Mischers.
- Wilhelm Wittl, Thomas Huber und Michael Weigl für die Unterstützung beim Bau der Ag-epoxy Filter. Zudem möchte ich Dieter Riedl für die Hilfe beim Bau der RC Filter und Alexander Meier für die Anfertigung der Semi-Rigid Kabeln danken.
- den Technikern des Lehrstuhls Uli Gürster, Daniel Pahl, Thomas Haller, Cornelia Linz und Michael Weigl für die Instandhaltung und Hilfestellungen an den Anlagen.
- Elke Haushalter und Claudia Moser für ihre Unterstützung bei allen organisatorischen Problemen.

- der ganzen Topo-Gruppe, allen voran Dr. Johannes Ziegler, Wolfgang Himmler, Stefan Hartl und Niklas Hüttner, die auch das Interesse für topologische Supraleitung stets geteilt haben.
- Pauline Drexler, Elisabeth Richter, Stefan Hartl, Wolfgang Himmler, Niklas Hüttner und Jacob Fuchs für das Korrekturlesen meiner Arbeit.
- meinen Eltern und meiner Familie, die mir das alles ermöglicht und mich stets unterstützt haben.
- meiner Frau Kristin für ihre Unterstützung und Geduld, wenn ich mal wieder etwas länger arbeiten musste, sowie meinem Sohn Bastian, der im letzten Jahr so viel Freude in mein Leben gebracht hat.